Article

SOURCE DATA | TRANSPARENT PROCESS | OPEN ACCESS

EMBO reports

Monomeric agonist peptide/MHCII complexes activate T-cells in an autonomous fashion

René Platzer[1], Joschka Hellmeier[2,†], Janett Göhring[1], Iago Doel Perez[1,‡], Philipp Schatzlmaier[1], Clara Bodner[2], Margarete Focke-Tejkl[3], Gerhard J Schütz[2], Eva Sevcsik[2], Hannes Stockinger[1], Mario Brameshuber[2,*] & Johannes B Huppa[1,**]

Abstract

Molecular crowding of agonist peptide/MHC class II complexes (pMHCIIs) with structurally similar, yet *per se* non-stimulatory endogenous pMHCIIs is postulated to sensitize T-cells for the recognition of single antigens on the surface of dendritic cells and B-cells. When testing this premise with the use of advanced live cell microscopy, we observe pMHCIIs as monomeric, randomly distributed entities diffusing rapidly after entering the APC surface. Synaptic TCR engagement of highly abundant endogenous pMHCIIs is low or non-existent and affects neither TCR engagement of rare agonist pMHCII in early and advanced synapses nor agonist-induced TCR-proximal signaling. Our findings highlight the capacity of single freely diffusing agonist pMHCIIs to elicit the full T-cell response in an autonomous and peptide-specific fashion with consequences for adaptive immunity and immunotherapeutic approaches.

Keywords MHC class II; molecular imaging; T-cell antigen recognition
Subject Categories Immunology; Signal Transduction
DOI 10.15252/embr.202357842 | Received 19 July 2023 | Revised 4 September 2023 | Accepted 14 September 2023 | Published online 28 September 2023
EMBO Reports (2023) 24: e57842

Introduction

The recognition of antigenic peptides by T-cells relies on transient interactions with antigen-presenting cells or target cells (APC). The formation of this specialized cell contact—termed the immunological synapse—is driven by specific T-cell antigen receptors (TCRs) on the T-cell side engaging peptide-loaded MHC complex molecules (pMHCs; Bromley *et al*, 2001; Huppa & Davis, 2003). In this setting, T-cells can detect the presence of even a single stimulatory pMHC molecule among thousands of structurally similar yet non-stimulatory or endogenous pMHCs on a densely packed APC surface (Irvine *et al*, 2002; Li *et al*, 2004; Purbhoo *et al*, 2004; Huang *et al*, 2013). The molecular, biophysical, and cellular mechanisms underlying this phenomenon are still unclear, in particular when considering that most T-cell antigen receptors (TCR) engage their nominal ligands with a low-to-moderate affinity (1–100 μM), at least when measured *in vitro* (Matsui *et al*, 1991; Corr *et al*, 1994; Davis *et al*, 1998). Previous studies have suggested that ligand recognition may not only depend on the intrinsic binding properties of TCRs and pMHCs but also the quality and quantity of accessory interactions (i.e., CD28/B7-1, CD2/CD48, LFA-1/ICAM-1, and CD4 and CD8 co-receptors), as well as cell biological parameters such as TCR subunit or pMHC stoichiometry, local molecular crowding, and cytoskeletal forces (reviewed in Platzer & Huppa, 2020; Gohring *et al*, 2022).

Key to understanding the molecular foundation of T-cell antigen recognition is to examine TCR-pMHC engagement *in situ*, as conditions for binding within the synapse differ in many regards from those found in solution (Huang *et al*, 2010; Huppa *et al*, 2010). If positioned in sufficient proximity, TCRs and pMHCs engage each other on opposed plasma membranes in a pre-oriented fashion which appears to accelerate the binding on-rate (Huppa *et al*, 2010; Huang *et al*, 2013; Weikl *et al*, 2016). Synaptic TCR-pMHC lifetimes are furthermore affected by simultaneous engagement of co-receptors with the same pMHC (Huppa *et al*, 2010; Jiang *et al*, 2011) as well as cellular forces imposed on the binding partners (Liu *et al*, 2014; Feng *et al*, 2017; Sibener *et al*, 2018; Gohring *et al*, 2021; Pettmann *et al*, 2023). Furthermore, both pMHCI and pMHCII have been suggested to be organized in clusters (Lu *et al*, 2012) where they may undergo lateral interactions, which could alter binding and signaling dynamics. In fact, nanoscale MHCII clustering through interaction with tetraspanins or partitioning into glycosphingolipid rafts has been considered critical for accelerated T-cell scanning and sensitized antigen recognition (Anderson *et al*, 2000; Bosch *et al*, 2013; Zuidscherwoude *et al*, 2015). pMHCII enrichment has furthermore been suggested to drive the formation of pMHCII higher order structures, in particular in view of the tendency of some

1 Center for Pathophysiology, Infectiology, Immunology, Institute for Hygiene and Applied Immunology, Medical University of Vienna, Vienna, Austria
2 TU Wien, Institute of Applied Physics, Vienna, Austria
3 Center for Pathophysiology, Infectiology, Immunology, Institute for Pathophysiology and Allergy Research, Medical University of Vienna, Vienna, Austria
*Corresponding author. Tel: +43 1 58801 134896; E-mail: brameshuber@iap.tuwien.ac.at
**Corresponding author. Tel: +43 1 40160 33004; E-mail: johannes.huppa@meduniwien.ac.at
†Present address: Max Planck Institute of Biochemistry, Molecular Imaging and Bionanotechnology, Martinsried, Germany
‡Present address: Takeda Manufacturing Austria AG, Vienna, Austria

pMHCIIs to crystallize as dimers (Brown *et al*, 1993; Fremont *et al*, 2002). Consistent with this, soluble agonist pMHCIIs activate antigen-experienced T-cells only when tethered to a second agonist pMHCII or an endogenous pMHCII capable of TCR binding (Cochran *et al*, 2000; Krogsgaard *et al*, 2005). Rather than confounding the process of antigen recognition, highly abundant endogenous pMHCs have hence been proposed to facilitate the detection of rare agonist pMHCs in a so-termed "pseudodimer" arrangement (Wulfing *et al*, 2002; Krogsgaard *et al*, 2005; Anikeeva *et al*, 2012) whereby such pMHCs may act—without being able to stimulate T-cells on their own—as so-termed "co-agonists."

We have recently shown via molecular live cell imaging that TCRs are randomly distributed prior to pMHCII engagement (Rossboth *et al*, 2018; Platzer *et al*, 2020) and function as monomeric antigen-binding and -signaling entities (Brameshuber *et al*, 2018). Therefore, any co-agonistic effect mediated by a pseudodimer arrangement would have to result from agonist pMHCIIs being either displayed as part of the same higher order MHCII structure or densely packed in membrane nanodomains. However, to this date, neither the presence of MHCII-enriched membrane domains nor the existence of pMHCII dimers or higher order structures has been demonstrated on the surface of living APCs, and hence the relevance of pMHCII clustering for T-cell sensitization remains to be determined (Nagy *et al*, 2001; Gascoigne, 2008; Ma *et al*, 2008; Anikeeva *et al*, 2012; Hoerter *et al*, 2013).

To do so we have conducted minimally invasive single-molecule imaging on living professional APCs with sub-diffraction resolution. We failed to obtain any evidence for the existence or formation of higher order pMHCII structures prior to or in the course of antigen recognition and ruled out any relevance of such entities for antigen recognition if generated experimentally. Instead, we observed pMHCIIs as monomeric entities uniformly distributed at high densities across the plasma membrane and diffusing rapidly immediately after entering the surface of bone marrow-derived dendritic cells and B-cells. When measuring synaptic TCR-pMHCII interactions with the use of a Förster resonance energy transfer (FRET)-based assay, we did not find the presence of highly abundant endogenous bystander pMHCIIs to be relevant for (i) the TCR engagement of rare agonist pMHCII at early and later stages of synapse formation and (ii) ensuing TCR-proximal signaling. Instead, we witnessed low-level calcium signaling in T-cells facing "co-agonistic" altered peptide ligands (APLs) at supraphysiological densities (above 1,000 molecules μm^{-2}), yet without contributing to T-cell sensitization toward rare antigenic pMHCIIs. In summary, our findings challenge the concept of pMHCII co-agonism and underscore the stimulatory potency of single, freely diffusing agonist pMHCIIs, which activate cognate T-cells in a peptide-specific manner without any significant contribution from endogenous bystander pMHCIIs.

Results

Dendritic cells and B-cells express pMHCIIs at high numbers and densities

We first determined the number of pMHCIIs that T-cells can in principle encounter while scanning the surface of professional APCs. For precise quantitation, we employed a monovalent site-specifically labeled and in selected cases also biotinylated recombinant single-chain antibody fragment (scF_V) derived from the I-E^k-reactive 14.4.4S mAb (Appendix Fig S1A–E, for details, see Materials and Methods section). As verified by flow cytometry, 14.4.4 scF_V binding to I-E^k expressed on CH27 B-cells was specific, efficient, and stable: when employed at a concentration of 5 $\mu g\ ml^{-1}$ 14.4.4 scF_V conjugated to Alexa Fluor 647 or Alexa Fluor 488 (14.4.4 scF_V-AF647 or -AF488) decorated more than 95% of surface-expressed I-E^k with half-lives of staining amounting to 41 min at 37°C, 80 min at 25°C, and 16 h on ice (Appendix Fig S1C–E). To further confirm target specificity of the 14.4.4 scF_V, we co-cultured 5c.c7 TCR transgenic T-cells with moth cytochrome c (MCC 88–103) peptide-pulsed BMDCs at 37°C in the presence of 20 $\mu g\ ml^{-1}$ 14.4.4 scF_V. T-cells no longer secreted interferon-γ (IFN-γ) and tumor necrosis factor (TNF-α). EC50 values derived from a peptide titration series in the presence or absence of the 14.4.4 scF_V indicated an epitope coverage of 98.7% over a period of 4 h (Fig 1A and Appendix Fig S2A).

Total I-E^k surface expression was quantitated based on flow cytometric median fluorescence intensities (MFIs) of 14.4.4 scF_V-AF647-stained BMDCs and B-cells, which we then normalized to measured fluorescence intensities of AF647 quantification beads serving as reference (Appendix Fig S2B). As shown in Fig 1B, non-activated days 6 to 7 $CD11c^+$ I-E^{k+} BMDCs expressed an average of 0.5 million copies of I-E^k at the surface per cell, which increased to 4–5 million copies per BMDC upon activation with lipopolysaccharide (LPS). Indicative of partial BMDC maturation prior to LPS exposure, I-E^k expression levels of non-activated BMDCs (7 days after bone marrow isolation) were highly heterogeneous (Appendix Fig S3A), with $CD11c^+$ $CD11b^+$ I-$E^{k\ hi}$ BMDCs representing mainly mature DCs (Helft *et al*, 2015). At least in part owing to their significantly smaller size, $CD19^+$ B-cells displayed about 10- to 50-fold fewer copies of I-E^k, that is, on average $\sim 1 \times 10^5$ molecules per non-activated and $\sim 5 \times 10^5$ molecules per B-cell stimulated with LPS for 48 h (Fig 1C, and Appendix Fig S3B and C).

To account for all surface-resident pMHCIIs that are in principle available for T-cell scanning, we also determined the total number of displayed I-A^k copies indirectly through comparison of MFIs obtained from APCs stained with saturating quantities of the 14.4.4 mAb and the I-A^k-reactive 11-5.2 mAb (Fig 1D). After normalizing MFIs for degrees of antibody labeling (DOL; 14.4.4 mAb = 2.1; 11-5.2 mAb = 2.4), we arrived at similar numbers of I-A^k and I-E^k that were accessible to antibody staining on the surface of BMDCs and B-cells.

To assess whether endogenous pMHCIIs exerted any influence on the detection of rare agonist ligands, we sought to determine the number of bystander pMHCII in close vicinity to any scanning or ligated TCR. Of note, both BMDCs and B-cells gain considerably in surface area upon activation, while B-cells increase in overall size (blast formation), the surface of BMDCs changes from microvilli to veils (Verdijk *et al*, 2004). As a result, total cellular expression levels cannot easily be converted into molecular densities due to varying cell size and plasma membrane convolutions. We hence stained BMDCs and B-cells with saturating amounts of 14.4.4 scF_V site-specifically conjugated with Alexa Fluor 647 or Alexa Fluor 568, and then allowed the cells to spread on intercellular adhesion molecule 1 (ICAM-1)-coated glass slides as a means to directly measure surface I-E^k densities using total internal reflection fluorescence (TIRF) microscopy (Fig 1E). Image acquisition was conducted at room

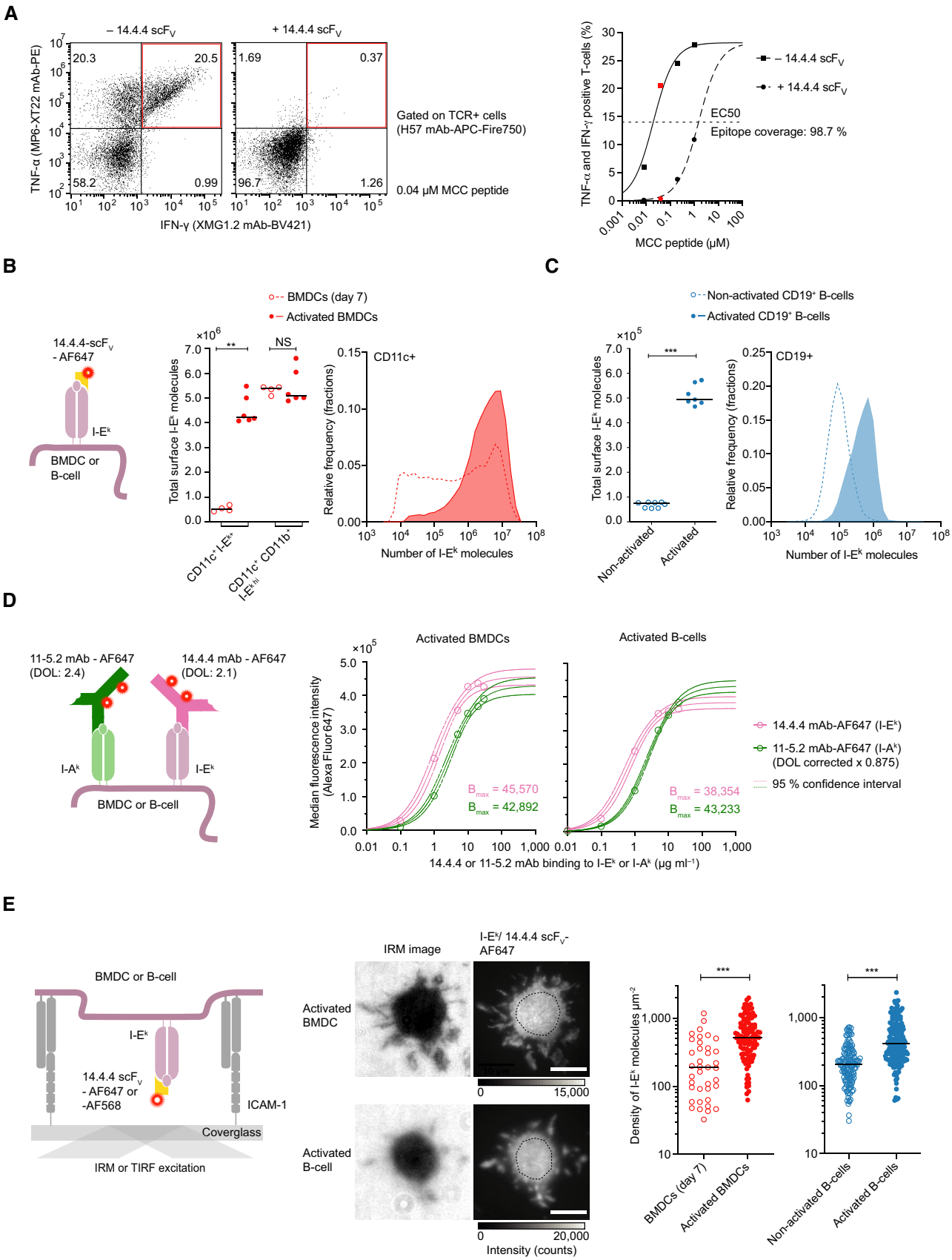
A
– 14.4.4 scFV
+ 14.4.4 scFV
TNF-α (MP6-XT22 mAb-PE)
IFN-γ (XMG1.2 mAb-BV421)
20.3
20.5
58.2
0.99
1.69
0.37
96.7
1.26
Gated on TCR+ cells
(H57 mAb-APC-Fire750)
0.04 μM MCC peptide
TNF-α and IFN-γ positive T-cells (%)
EC50
Epitope coverage: 98.7 %
MCC peptide (μM)
B
BMDCs (day 7)
Activated BMDCs
14.4.4-scFV
- AF647
I-Ek
BMDC or
B-cell
Total surface I-Ek molecules
CD11c+ I-Ek+
CD11c+ CD11b+
I-Ekhi
CD11c+
Relative frequency (fractions)
Number of I-Ek molecules
C
Non-activated CD19+ B-cells
Activated CD19+ B-cells
Non-activated
Activated
CD19+
D
11-5.2 mAb - AF647
(DOL: 2.4)
14.4.4 mAb - AF647
(DOL: 2.1)
I-Ak
I-Ek
BMDC or B-cell
Activated BMDCs
Activated B-cells
Median fluorescence intensity
(Alexa Fluor 647)
Bmax = 45,570
Bmax = 42,892
Bmax = 38,354
Bmax = 43,233
14.4.4 or 11-5.2 mAb binding to I-Ek or I-Ak (μg ml−1)
14.4.4 mAb-AF647 (I-Ek)
11-5.2 mAb-AF647 (I-Ak)
(DOL corrected x 0.875)
95 % confidence interval
E
BMDC or B-cell
I-Ek
14.4.4 scFV
- AF647 or
-AF568
ICAM-1
Coverglass
IRM or TIRF excitation
IRM image
I-Ek/ 14.4.4 scFV-
AF647
Activated
BMDC
Activated
B-cell
Intensity (counts)
Density of I-Ek molecules μm-2
BMDCs (day 7)
Activated BMDCs
Non-activated B-cells
Activated B-cells

Figure 1.

Figure 1. Dendritic cells and B-cells express pMHCIIs at high numbers and densities.

A Efficient blockade of T-cell antigen recognition by the 14.4.4 scF_V. Shown is the flow cytometric analysis (refer to Appendix Fig S2A) of antigen-induced TNF-α and IFN-γ expression in 5c.c7 TCR-transgenic T-cells co-cultured with BMDCs which had been prepulsed with MCC peptide antigen (from 0 to 1 μM) in the absence or presence of the 14.4.4 scF_V with a representative dot plot (0.05 μM MCC peptide) depicted on the left. Flow cytometry analysis was conducted with $n > 11{,}000$ cells per condition.

B I-E^k is expressed at high numbers on activated $CD11c^+$ $CD11b^+$ BMDCs. Left panel: staining procedure employed for quantitation. Middle panel: the median number of I-E^k molecules displayed on the surface of non-activated and activated BMDCs ($n > 10{,}000$ cells per analysis), gated as $CD11c^+$ I-E^{k+} or $CD11c^+$ $CD11b^+$ I-$E^{k\ hi}$, as analyzed through quantitative flow cytometry. Statistics: median and Mann–Whitney *U*-test. Data were pooled from two biological replicates each containing $n = 2$ (BMDCs day 7) and $n = 2$–4 (activated BMDCs) technical replicates. Right panel: histogram depicting the distribution of surface-expressed I-E^k molecules on non-activated (dashed) and activated (solid) $CD11c^+$ BMDCs (binning = 0.15 (log scale), $n = 14{,}585$ non-activated BMDCs, $n = 24{,}214$ activated BMDCs). Data are representative of two biological replicates. *P*-value format: $P > 0.05$ (NS), $P \leq 0.01$ (**).

C I-E^k is expressed at high numbers on non-activated and activated $CD19^+$ B-cells. Left panel: the median number of I-E^k molecules displayed on the surface of non-activated and activated $CD19^+$ B-cells ($n > 10{,}000$ cells per analysis) as analyzed through quantitative flow cytometry. Statistics: median and Mann–Whitney *U*-test. Data were pooled from three biological replicates each containing $n = 2$–3 technical replicates. Right panel: histogram depicting the distribution of I-E^k molecules expressed on non-activated and activated $CD19^+$ B-cells (binning = 0.15 (log scale), $n = 14{,}032$ non-activated $CD19^+$ B-cells, $n = 10{,}010$ activated $CD19^+$ B-cells). Data are representative of three biological replicates. *P*-value format: $P \leq 0.001$ (***).

D I-A^k and I-E^k molecules are expressed on the surface of activated $CD11c^+$ BMDCs and activated $CD19^+$ B-cells at similar levels. Left panel: staining procedure employed for quantitation. Right panel: I-A^k and I-E^k expression levels as determined on the basis of I-E^k surface expression after correcting for the degree of fluorophore conjugation of the antibodies employed. The mAb titration curves were fitted to a one-site-specific binding model to estimate B_{max} and the 95% confidence interval. Goodness of fit $R^2 > 0.99$. Median fluorescence intensity of $n > 10{,}000$ cells shown. These data are representative of one experiment.

E High I-E^k densities as measured via TIRF microscopy on the surface of activated BMDCs and B-cells. Left panel: Scheme illustrating 14.4.4 scF_V-AF647-based staining as well as interference reflection microscopy (IRM)- and total internal reflection fluorescence (TIRF)-based microscopy readout to confirm attachment and spreading of cells on the ICAM-1-coated glass surface and density quantitation, respectively. Middle panel: Example of IRM and TIRF images of indicated cells on ICAM-1-functionalized glass slides. Upper scale bar, 10 μm. Lower scale bar, 5 μm. Right panel: Dot plot of I-E^k surface densities on non-activated BMDCs (median, $n = 38$ cells), activated BMDCs (median, $n = 113$ cells), non-activated B-cells (median, $n = 141$ cells), and activated B-cells (median, $n = 188$ cells). Data were pooled from two (BMDCs day 7), three (activated BMDCs), and five (non-activated or activated B-cells) biological replicates. Statistics: median, unpaired two-tailed Student's *t*-test. *P*-value format: $P \leq 0.001$ (***).

Source data are available online for this figure.

temperature (22.5°C) to minimize probe dissociation (Appendix Fig S1D). Tight alignment of the APC plasma membrane with the glass slide was verified by interference reflection microscopy (IRM). We then determined average I-E^k densities within a central region of interest (ROI) randomly picked from the cell–glass contact region. For this, we divided the integrated background-subtracted fluorescence intensity by the mean intensity of a single-molecule fluorescent signal and the area of the ROI (Fig 1E, for more details, refer to Materials and Methods). We arrived at a median I-E^k surface density of 188 molecules μm^{-2} (minimum: 33 μm^{-2}, maximum: 1,179 μm^{-2}) on non-activated BMDCs and 206 molecules μm^{-2} (minimum: 30 μm^{-2}, maximum: 723 μm^{-2}) on non-activated B-cells (Fig 1E). After LPS treatment, we noticed an approximately twofold increase in I-E^k surface densities on BMDCs (median: 514 μm^{-2}, minimum: 63 μm^{-2}, maximum: 1,991 μm^{-2}) and B-cells (median: 413 μm^{-2}, minimum: 61 μm^{-2}, maximum: 2,346 μm^{-2}).

I-E^k molecules fail to associate with detergent-resistant membranes and are randomly distributed on the surface of activated BMDCs and B-cells

pMHCII have previously been described to be sequestered to so-termed lipid rafts, a class of small and highly dynamic membrane domains consisting of cholesterol, sphingolipids, saturated fatty acids, and glycosylphosphatidylinositol (GPI)-anchored and cysteine-palmitoylated proteins (Anderson *et al*, 2000; Kusumi *et al*, 2012; Sevcsik *et al*, 2015), the existence of which is, however, controversially debated. To assess possible mechanisms underlying lipid raft-dependent T-cell sensitization as proposed by others (Anderson *et al*, 2000; Bosch *et al*, 2013), we quantitated the extent to which pMHCIIs on the surface of BMDCs and B-cells are found in so-termed detergent-resistant membranes (DRMs). Protein presence in DRMs has previously been regarded as the biochemical equivalent of lipid raft residence. To this end, we conducted lysis gradient centrifugation (LGC) affording comprehensive results with a sample size of fewer than 10,000 cells when combined with a flow cytometric readout (Schatzlmaier *et al*, 2015). The LGC methodology rests on quantitative co-isolation of DRMs and their associated proteins with the detergent-resistant nuclei of their parental detergent-treated cells (Appendix Fig S4A). As shown in Appendix Fig S4B and C, we analyzed surface-resident I-E^k or I-A^k molecules on non-activated and activated BMDCs and B-cells as well as the GPI-anchored DRM markers CD44 and CD55 as positive control, and the non-DRM resident CD71 as negative control. As expected, CD44 and CD55 decorated with fluorescently labeled mAbs were predominantly present within the DRM fraction while CD71 was absent, testifying to the technical integrity of the experiment. Strikingly, I-E^k labeled with either the 14.4.4-scF_V-AF647 or 14.4.4 mAb-AF647 was hardly detectable in DRMs (< 1%, see Appendix Fig S4C), a behavior we could also associate with I-A^k decorated with the 11-5.2 mAb-AF647 on the surface of both BMDCs and B-cells. Contrasting previous reports, these results indicate that MHCIIs, at least when present on the surface of primary B-cells and BMDCs, are predominantly absent from or only very weakly associated with DRMs (< 1%).

To examine whether pMHCIIs are enriched in micro- or nanoclusters other than lipid rafts, we stained living activated BMDCs and B-cells with randomly AF647-conjugated I-E^k and I-A^k-reactive mAbs or site-specifically AF647-conjugated 14.4.4 scF_Vs and analyzed cellular mid-sections via fluorescence microscopy.

We continued our study by focusing primarily on activated BMDCs given the pivotal role in T-cell priming. For comparative analysis, we also included activated B-cells in our study. Using the 14.4.4 scF_V or 14.4.4 mAb (or 11-5.2 mAb) as probe, deconvolved images revealed uniform staining of I-E^k or I-A^k. As is consistent

with a previous study (Bosch *et al*, 2013), we observed a punctate staining pattern on BMDCs after exposing surface-resident mAb-engaged I-E^k molecules with secondary AF647-conjugated IgG mAbs. Taken together, we concluded that pMHCIIs are not organized in plasma membrane microdomains that are large enough to be resolvable with diffraction-limited microscopy (Appendix Fig S5A and B).

To determine whether pMHCIIs are enriched in plasma membrane nanodomains, which can no longer be identified by conventional fluorescence microscopy, we analyzed the surface distribution of I-E^k on living and paraformaldehyde (PFA)-fixed BMDCs and B-cells with sub-diffraction resolution applying high-speed photoactivation localization microscopy (hsPALM). We included cell fixation in half of our analyses since the high lateral diffusion of pMHCII may compromise cluster detection via hsPALM. Of note, PALM relies on the stochastic photo-switching of suitable fluorophores between a blue-shifted fluorescent or dark state and a red-shifted or bright fluorescent state and the subsequent reconstruction of diffraction-limited but well-separated single-molecule events into a localization map (Betzig *et al*, 2006; Hess *et al*, 2006). For visualization of I-E^k, we site-specifically conjugated the 14.4.4 scF$_V$ with AF647 and biotin (14.4.4 scF$_V$-AF647-biotin, Fig 2A and Appendix Fig S1B). Cell surface-resident 14.4.4 scF$_V$-AF647-biotin was then detected in hsPALM with the use of monovalent streptavidin (mSav) site-specifically conjugated with recombinant PS-CFP2 (mSav-cc-PS-CFP2, Fig 2A and Appendix Fig S6A–E), a photo-switchable fluorophore with a moderate repetitive blinking behavior (Platzer *et al*, 2020).

To allow for noise-reduced imaging in TIRF mode, we seeded living BMDCs and B-cells labeled with 14.4.4 scF$_V$-AF647-biotin and mSav-cc-PS-CFP2 on ICAM-1-coated glass slides. Prior to conducting hsPALM, attachment of each cell was verified through acquisition of a single AF647 ensemble fluorescence image, which also served to assess surface I-E^k distribution at a diffraction-limited level (Fig 2B). For hsPALM, we recorded 3,050 image frames that displayed single-diffraction-limited PS-CFP2 fluorescence events within a timeframe of 7 s. Diffraction-limited single-molecule signals were then fitted with a Gaussian intensity profile accounting for the point spread function, spatially positioned with an accuracy of 15 to 108 (mean value 51 ± 12) nm (Appendix Fig S6F) and then superimposed to give rise to a composite localization map.

Of note, the interpretation of single-molecule localization microscopy (SMLM) data is typically complicated by overcounting and undercounting artifacts, which result from insufficient photobleaching (on–off blinking) and variability in psCFP maturation. Fluorophore blinking can give rise to false-positive nanocluster detections in the reconstructed localization map (Annibale *et al*, 2011; Baumgart *et al*, 2016). To distinguish true protein nanoclusters from overcounting artifacts, we first employed an imaging platform to quantitatively determine the blinking signature of PS-CFP2 (Appendix Fig S7A) prior to PALM measurements on cells (Platzer *et al*, 2020). To promote the appearance of PS-CFP2 in a single imaging frame only, we employed a 488 nm laser power density of 3.5 kW cm^{-2} and recorded the images in stream mode (488 nm laser is continuously illuminating) with an illumination time of 2 ms. Applying a Monte-Carlo simulation-based approach, we quantitatively related cell-derived PALM images to localization maps, which had been computed from simulated random distributions featuring cell-derived molecular densities, the diffusion parameters of I-E^k at 25°C (Appendix Fig S7B), and the respective blinking signature of PS-CFP2 (Appendix Fig S8A and B, for more details, see Materials and Methods). As shown in Fig 2B and summarized in Appendix Fig S8C, comparing respective Ripley's K functions of recorded I-E^k localization maps with those derived from simulated random localization maps did not reveal Ripley's K maxima above the simulation (mean ± standard deviation) for most of the investigated cell regions, which let us conclude that pMHCIIs are uniformly distributed on the surface of activated BMDCs and B-cells, at least when judged within the cluster detection sensitivity of our approach (Appendix Fig S7A). Importantly and in contrast, we could detect local surface enrichments for the internalization receptor CD205 and for the integrin beta-chain CD18 (Fig 2C and D, and Appendix Fig S7C and D) on all investigated cell regions (Appendix Fig S8C). Confirming the sensitivity and robustness of our imaging and analysis methodologies, background localizations registered only in negligible numbers in the absence of PS-CFP2 (Appendix Fig S7E). To circumvent potential complications arising from molecular diffusion and cellular motility, we performed analogous imaging and analysis procedures on PFA-fixed activated BMDCs and B-cells. As shown in Appendix Fig S9A and B and summarized in Appendix Fig S8C, we frequently identified inhomogeneities and thus small deviations from a normal random distribution of I-E^k on PFA-fixed cell regions, which could have also arisen from the fixation procedure itself.

We hence carried out artifact-free label density variation SMLM (Baumgart *et al*, 2016) to quantitate the extent to which I-E^k is organized in nanoscale entities within I-E^k localization maps derived from PFA-fixed activated BMDCs and B-cells. To this end and based on image analysis, we assigned a spatial uncertainty (σ) of 35 nm to each PS-CFP2 localization and merged overlapping Gaussian profiles to three-dimensional cluster maps (X, Y position, intensity, Fig 2E). We calculated localization densities within an assigned clustered area (ρ) and the relative clustered area to the total area (η) for a given threshold (1.0) and plotted the density of localizations in the clustered area μm^{-2} (ρ) against η (clustered area divided by total area). In case of a uniform fluorophore distribution, the relative area covered by artificial clusters resulting from fluorophore blinking will increase steadily with an increasing degree of labeling, while the density of localizations per cluster is expected to remain constant. Conversely, if molecules are in fact clustered, the relative area will saturate, and the density of localizations per cluster will increase with the degree of labeling. Results correlated best with a random distribution of I-E^k on activated PFA-fixed BMDCs and B-cells, in particular, because the localization density within the clustered area did not deviate with higher staining degree from a simulated random distribution (solid line), unlike what would be expected from a clustered distribution (Fig 2F). In contrast and consistent with previous studies, label density variation SMLM revealed clustering of CD205 on BMDCs, with an increase in the localization density within clusters at higher expression or staining levels (Fig 2F).

We further refined and advanced our analysis by applying a model-based correction (MBC) workflow on localization maps derived from living and PFA-fixed cell regions. MBC is based on the calibration-free estimation of PS-CFP2 blinking dynamics followed by a hierarchical clustering step to give rise to a corrected set of localization coordinates without fluorescence blinking (Bohrer *et al*, 2021;

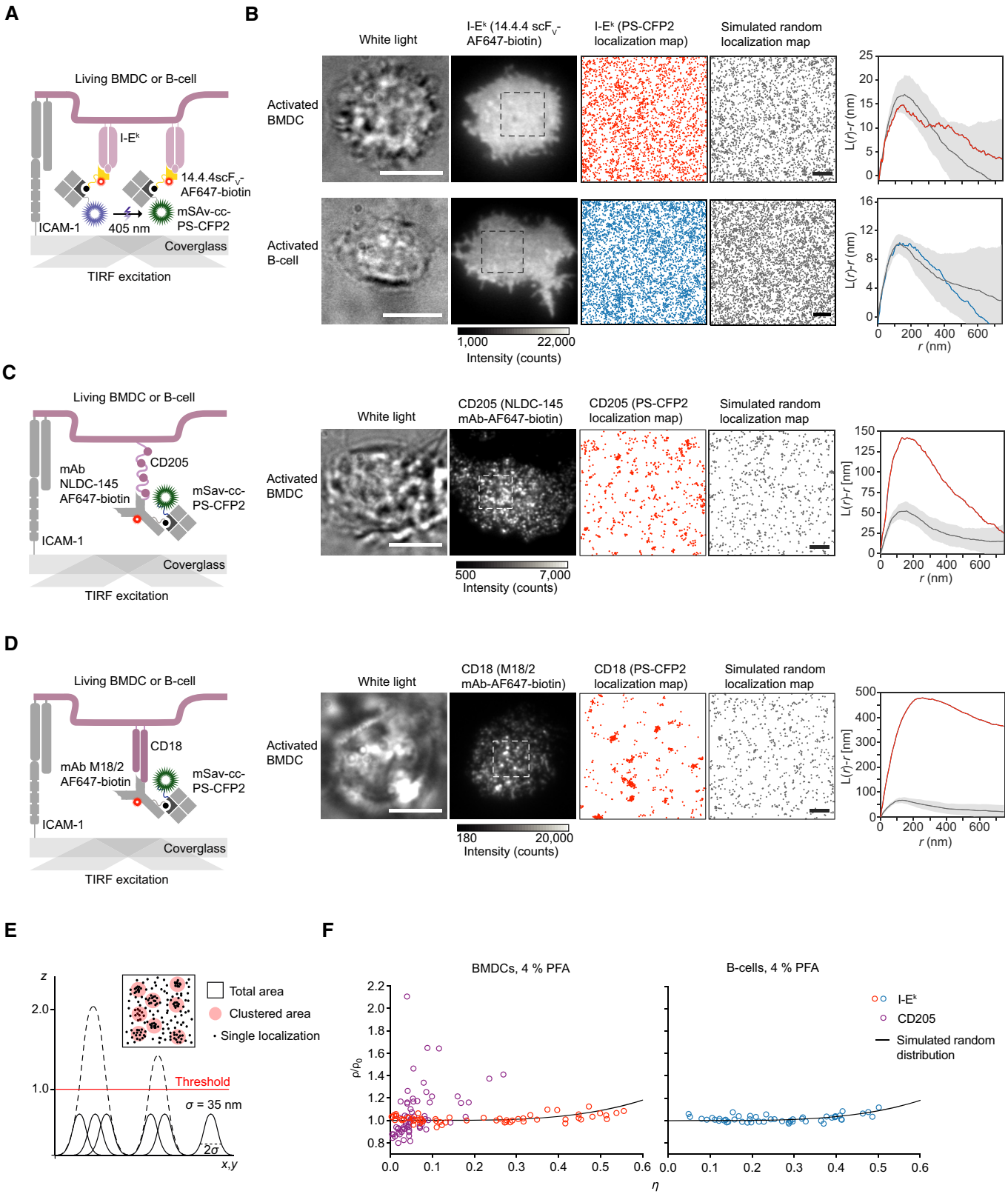

Figure 2.

Figure 2. I-E^k molecules are randomly distributed on the surface of activated BMDCs and B-cells.

A Staining procedure to image the surface distribution of I-E^k on living professional APCs below the diffraction limit of visible light using hsPALM.

B BMDCs and B-cells were stained with 14.4.4 scF$_V$-AF647-biotin and mSav-cc-PS-CFP2 and seeded onto ICAM-1-coated glass slides for imaging in TIRF mode. The presence of each cell was verified through acquisition of a white light image (first image, scale bar 10 μm), a single AF647 ensemble fluorescence image (second image), followed by 3,050 image frames displaying single PS-CFP2 fluorescence events acquired within 7 s to be assembled as a localization map (third image), which was compared to a simulated random I-E^k localization map (fourth image, scale bar 1 μm). Ripley's K analysis was used to compare BMDC-derived I-E^k distributions (red) or B-cell-derived I-E^k distributions (blue) to 10 simulations of randomized distributions with corresponding molecular densities, diffusion parameters, and blinking statistics (gray). Statistics: mean ± standard deviation.

C, D Quantification of the surface distribution of (C) CD205 and (D) CD18 on activated BMDCs. Left panels: Staining and imaging procedure. Right panels: BMDCs were stained with the indicated mAbs (NLDC-145 mAb-AF647-biotin or M18/2 mAb-AF647-biotin) and mSav-cc-PS-CFP2 for hsPALM imaging. Large scale bars, 10 μm. Small scale bars, 1 μm. Ripley's K analysis was used to compare cell-derived CD205 distributions (red) to 10 simulations of randomized distributions with corresponding molecular densities, diffusion parameters, and blinking statistics (gray). Statistics: mean ± standard deviation.

E Principle of label density variation analysis. A theoretical spatial uncertainty (σ) of 35 nm was assigned to each PS-CFP2 localization and overlapping Gaussian profiles were merged (and intensities were added up) to arrive at three-dimensional cluster maps (X, Y position, intensity). Different thresholds were assigned to probe-derived cluster maps and calculate ρ (the density of localizations in the clustered area μm^{-2}) and η (clustered area divided by total area).

F Label density variation analysis is consistent with a random surface distribution of I-E^k on activated BMDCs and B-cells and a clustered surface distribution of CD205 on activated BMDCs which served as a positive control. Quantification of the relative clustered area (η) and the density of localizations per clustered area (ρ) for indicated molecular species at a threshold of 1.0. The black line indicates the reference curve for a random distribution. This data set was derived from two biological replicates with a total of $n = 59$ activated BMDCs (I-E^k), $n = 53$ activated B-cells (I-E^k), and $n = 64$ activated BMDCs (CD205).

Source data are available online for this figure.

Jensen *et al*, 2022). After MBC of the recorded localization maps, we were able to perform a detailed characterization of the ground truth protein distribution using Ripley's K (Appendix Fig S8A and B) and density-based spatial clustering of applications with noise (DBSCAN) analysis (Ester *et al*, 1996). As shown in Appendix Fig S8D (for living cells) and Appendix Fig S8F (for PFA-fixed cells), summarized Ripley's K functions (mean ± standard deviation) of I-E^k localization maps did not diverge considerably from the baseline around zero, which exemplifies spatial randomness. Likewise, DBSCAN analysis, referenced to the simulated random distribution (for details, see Materials and Methods section), categorized most of the detected I-E^k localizations on living and PFA-fixed cell regions as uniformly distributed noise points (Appendix Fig S8E and G). Consequently, only 0 to 6 % of I-E^k molecules (average ~1%) appeared in zero to two clusters per region with a maximum of zero to seven molecules per cluster on (living and PFA-fixed) activated BMDCs and B-cells (Appendix Fig S8E and G). This was in stark contrast to CD205, with ~39% of CD205 molecules (26–58%) present in clusters of up to 16 molecules per cluster (average ~9) and 2 to 16 clusters per region (average ~8), which was further confirmed by means of the summarized Ripley's K function as being clearly above the simulated random distribution (Appendix Fig S8B, D and F).

Lastly, to avoid any issues potentially arising from SMLM and data interpretation, we employed stimulated emission depletion (STED) microscopy. STED is not susceptible to artifacts resulting from overcounting, as it resolves structures below the diffraction limit of visible light by reducing the width of the point spread function to several tens of nanometers through high-powered stimulated emission depletion (Sahl *et al*, 2017). For this purpose, we stained activated BMDCs and B-cells with a 14.4.4-scF$_V$ which had been site-specifically conjugated with abSTAR635P (14.4.4-scF$_V$-abSTAR635P), a STED-compatible fluorophore, and allowed the cells to spread on ICAM-1-coated glass slides prior to PFA-mediated fixation (Appendix Figs S10A and B, and S11). To assess the degree of pMHCII clustering in STED microscopy images, we compared the STED recordings with simulated images of randomly distributed molecules obtained with the fitted parameters of single fluorescence emitters derived from activated BMDCs and B-cells labeled with single 14.4.4 scF$_V$-abSTAR635P molecules (Appendix Fig S10A). To this end, we employed image autocorrelation function (ACF) analysis, which calculates the probability that two pixels separated by a distance r feature similar brightness, and thus enables quantification of the spatial distribution of fluorophores in the recorded STED images (Robertson & George, 2012). The ACF amplitude scales with the inverse of the number of molecules per pixel, thus, small surface densities as well as clustering of molecules yielded a pronounced increase in the ACF amplitude (Sengupta *et al*, 2011; Rossboth *et al*, 2018). ACF analysis of the recorded STED images of fixed activated BMDCs (Appendix Fig S10B) and B-cells (Appendix Fig S11) decorated with 14.4.4 scF$_V$-abSTAR635P did not reveal any difference in the ACF curves when compared to analyses of simulated random pMHCII distributions.

In summary, the use of two independent super-resolution methodologies and three autonomous cluster analysis tools leaves no conclusion other than that the majority of surface I-E^k molecules (> 90%) are not organized in nanoclusters but instead uniformly distributed on the surface of living as well as PFA-fixed activated BMDCs and B-cells.

Surface-resident I-E^k molecules pMHCIIs are to 99% mobile with 60–70% displaying fast diffusion immediately after entering the cell surface

The lateral mobility of pMHCII may influence T-cell antigen detection as it affects (i) the speed with which antigens become distributed on the APC surface, (ii) the frequency of serial TCR engagement, (iii) the dynamics of lateral pMHCII interactions, and also (iv) the mechanical forces exerted on pMHCII-engaged TCRs (Gohring *et al*, 2021) with possible consequences for the ensuing TCR-proximal signaling response (Hsu *et al*, 2012). To measure the lateral mobility of I-E^k by single-molecule tracking (Vrljic *et al*, 2002; Umemura *et al*, 2008), we decorated I-E^k molecules in low abundance on non-activated as well as activated BMDCs and B-cells with Alexa Fluor 555-conjugated 14.4.4 scF$_V$ (14.4.4 scF$_V$-AF555) prior to allowing the cells to spread on ICAM-1-coated glass slides for TIRF imaging at 37°C (Fig 3A). We recorded traces of single I-E^k molecules over several hundred

milliseconds with a delay time of about 10 ms. Trajectories containing 2 to 50 steps were used to calculate the mean square displacement and diffusion constants for I-E^k (Fig 3B and C). Overall, I-E^k diffusion was significantly faster on activated BMDCs than on activated B-cells with average diffusion constants of $D = 0.300\ \mu m^2\ s^{-1}$ and $D = 0.209\ \mu m^2\ s^{-1}$, respectively (Fig 3D). Since we witnessed a broad distribution of diffusion constants for individual I-E^k traces, we fitted all recorded trajectories to a binary diffusion model (see Materials and Methods) and identified a fast (73.1% on activated BMDC and 62.6% on activated B-cells) and a more slowly diffusing fraction as well as a small fraction of immobile I-E^k (< 1%). Based on mean square displacement analysis, the rapidly diffusing I-E^k molecules appeared to follow free Brownian motion on activated BMDCs ($D = 0.364\ \mu m^2\ s^{-1}$) and activated B-cells ($D = 0.263\ \mu m^2\ s^{-1}$) while the slowly moving I-E^k fraction ($D = 0.026\ \mu m^2\ s^{-1}$, activated BMDCs; $D = 0.017\ \mu m^2\ s^{-1}$, activated B-cells, Fig 3E) showed signs of confinement with a radius smaller than 75 nm (Wieser & Schutz, 2008). We arrived at similar I-E^k diffusion parameters when comparing the binary data fit performed on individual cells (Fig 3F). Following 24 to 48 h of LPS treatment, the fraction of rapidly diffusing I-E^k entities increased marginally in B-cells, but not in BMDCs, and the mobility of rapidly moving I-E^k molecules increased slightly on both activated BMDCs and B-cells (Appendix Fig S12A–F). Furthermore, the average diffusion constant of the slowly moving fraction did not change after LPS treatment and was similar for BMDC- and B-cell-resident I-E^k molecules (Appendix Fig S12B and D).

We next visualized the dynamics with which I-E^k molecules dispersed at any given time on the APC surface. For this, we decorated activated BMDCs with a site-specifically biotinylated 14.4.4 scF$_V$ (14.4.4 scF$_V$-biotin) for the detection with mSav. The latter had been site-specifically conjugated with abCAGE635, a photo-switchable and photo-stable bright fluorophore (Fig 3G and Appendix Fig S6C). Stained BMDCs and B-cells were seeded on ICAM-1-coated glass slides for imaging at 37°C in TIRF mode. As shown in Fig 3H and I and consistent with high lateral mobility, we witnessed a rapid dispersion of I-E^k-associated photo-uncaged fluorescence over the entire surface of BMDCs and B-cells within 150 s after applying a single UV pulse to photo-converge a small, selected area.

Extracellular antigens are present at high concentrations in the MIIC or endosomal peptide-loading compartments (Pierre *et al*, 1997; Turley *et al*, 2000). Antigen proximity could in principle be spatially and temporally conserved on the cell surface after exosome fusion with the plasma membrane. If true, this may in turn enhance T-cell antigen detection. To test whether pMHCIIs are locally enriched within the first minutes after entering the cell surface, we loaded I-E^k with a traceable peptide. To this end, we exposed non-activated BMDCs (day 6) and activated B-cells (day 2) for 0 to 36 h to a C-terminally biotinylated MCC peptide 88–103 derivative (MCC-PEG$_2$-biotin) in the presence of LPS. We first determined the proportion of surface-resident MCC-PEG$_2$-biotin-loaded I-E^k molecules by flow cytometry of activated BMDCs (up to 17%) and B-cells (up to 25%) with the use of site-specifically AF647-conjugated monovalent streptavidin (Fig 4A and B, and Appendix Fig S13A). We next tracked surface I-E^k/MCC-PEG$_2$-biotin complexes 6–12 h after addition of the peptide to the APC culture, that is, 0–12 h prior to maximal I-E^k/MCC-PEG$_2$-biotin surface expression (Fig 4A). To discriminate newly arriving I-E^k/MCC-PEG$_2$-biotin complexes from all other previously arrived I-E^k/MCC-PEG$_2$-biotin complexes, we first blocked surface-exposed biotin residues quantitatively using an excess of unlabeled monovalent mSav (500 $\mu g\ ml^{-1}$; for more details, refer to Materials and Methods section). After removing unbound mSav species as part of a rapid washing step conducted at 4°C to avoid fusion of MHCII-loaded anterograde transport vesicles with the plasma membrane, we allowed newly assembled I-E^k/MCC-PEG$_2$-biotin complexes to arrive at the cell surface for 10 min at 37°C, where they were directly conjugated to site-specifically abCAGE635-labeled mSav (or AF555-labeled mSav) and subsequently tracked as single molecules after photo-uncaging by TIRF microscopy at 37°C (Fig 4C). After preblocking and staining at 4°C, only a small number of I-E^k/MCC-PEG$_2$-biotin complexes were still accessible for staining with abCAGE635-labeled mSav (with an average of 70 trajectories per BMDC and 15 trajectories per B-cell). This number increased around 10-fold after incubating the cells at 37°C, indicating that more than 90% of the observable I-E^k/MCC-PEG$_2$-biotin complexes had arrived at the cell surface within the recovery time of 10 min (Appendix Fig S13B and C).

As shown in Fig 4C, newly arriving I-E^k molecules exhibited a similar, if not even slightly elevated lateral mobility when compared to all other I-E^k molecules on mature BMDCs ($D_{new} = 0.534 \pm 0.008\ \mu m^2\ s^{-1}$; $D_{pool} = 0.448 \pm 0.005\ \mu m^2\ s^{-1}$) and activated B-cells ($D_{new} = 0.251 \pm 0.005\ \mu m^2\ s^{-1}$; $D_{pool} = 0.237 \pm 0.003\ \mu m^2\ s^{-1}$). The proportion of newly arrived rapidly moving I-E^k molecules remained unchanged on activated BMDCs (Fig 4D and Appendix Fig S13D) and was marginally decreased on activated B-cells (Fig 4E and Appendix Fig S13E).

Taken together, our single-molecule tracking analysis rendered a scenario, in which newly arriving antigen-loaded MHCIIs conserve their spatial proximity observed in MIIC compartments and anterograde transport vesicles, rather unlikely, at least within a physiologically meaningful timeframe. Still to be considered is, however, the possibility that such molecules undergo confined diffusion over a prolonged period of time together with other colocalizing antigen-loaded MHCIIs derived from the same vesicle. Yet inconsistent with this notion is the observation that the labeling procedure employed gave exclusively rise to diffraction-limited fluorescence events which featured brightness values matching those of single fluorophores.

Surface-resident I-Ek molecules are monomeric

In large part motivated by our above findings, we next sought to assess in a definitive manner the possibility that pMHCII forms higher order structures on the surface of living APCs. In fact, the observation that some pMHCII variants crystalize as dimeric entities (Brown *et al*, 1993) could in principle result from an inherent propensity of pMHCII to assemble into complexes of larger size. If true, such behavior may sensitize T-cell antigen detection, as had been previously proposed by the "TCR-pseudodimer" model, which postulates simultaneous binding of two adjacent TCRs to a pMHCII agonist and a physically linked pMHCII co-agonist (Krogsgaard *et al*, 2005).

I-E^k surface densities on living activated BMDCs (i.e., median 514 molecules μm^{-2}) and activated B-cells (median 413 molecules μm^{-2}) are too high to allow for nanoscopic assessment of individual I-E^k mono- or multimers via diffraction-limited microscopy. To score for the presence of I-E^k oligomers on living APCs, we hence resorted to the "Thinning Out Clusters While Conserving the Stoichiometry

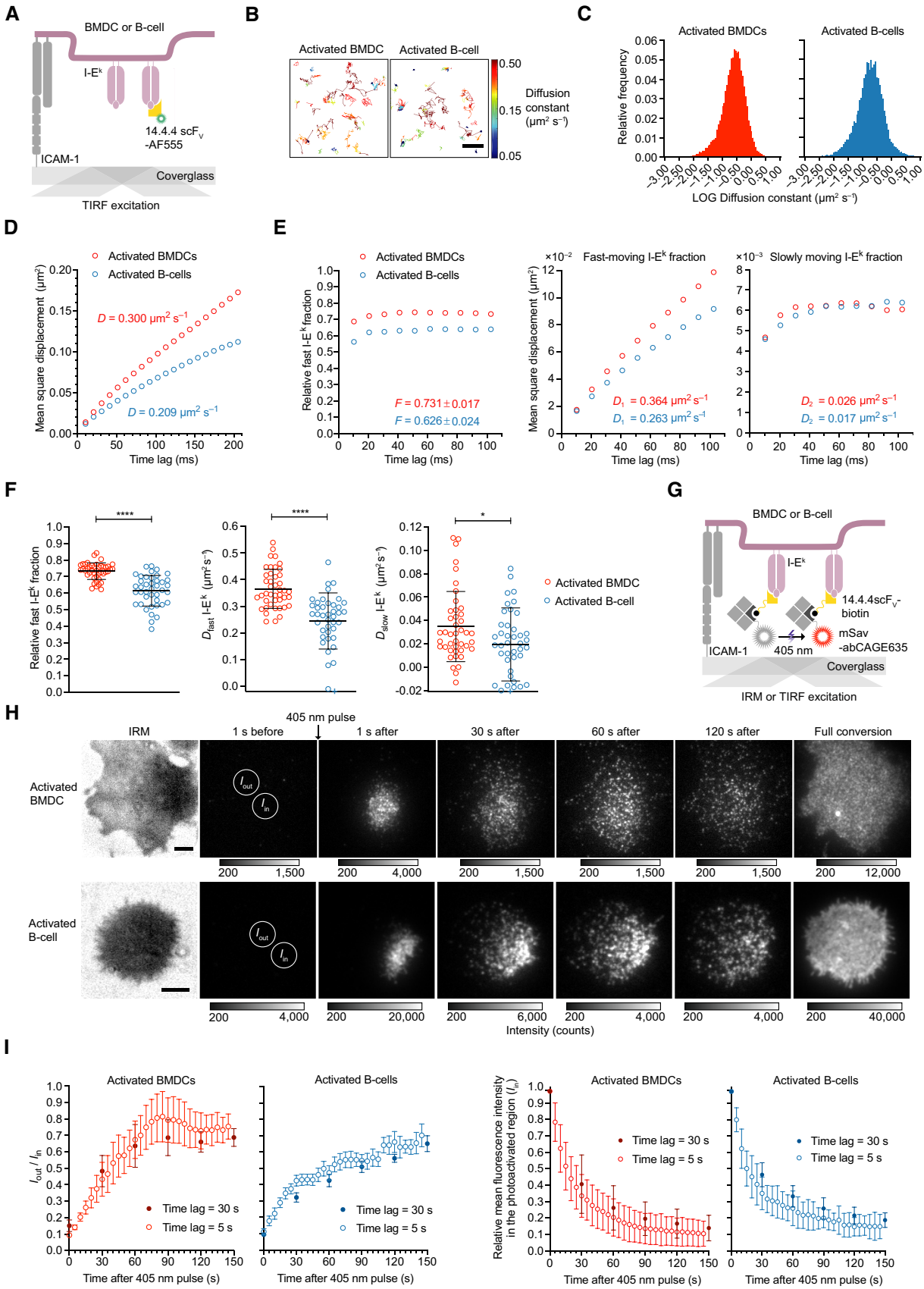
A
BMDC or B-cell
I-E^k
14.4.4 scF_V -AF555
ICAM-1
Coverglass
TIRF excitation
B
Activated BMDC
Activated B-cell
0.50
0.15
0.05
Diffusion constant (μm² s⁻¹)
C
Activated BMDCs
Activated B-cells
Relative frequency
LOG Diffusion constant (μm² s⁻¹)
D
Activated BMDCs
Activated B-cells
D = 0.300 μm² s⁻¹
D = 0.209 μm² s⁻¹
Mean square displacement (μm²)
Time lag (ms)
E
Activated BMDCs
Activated B-cells
Relative fast I-E^k fraction
F = 0.731 ± 0.017
F = 0.626 ± 0.024
Time lag (ms)
×10⁻² Fast-moving I-E^k fraction
D₁ = 0.364 μm² s⁻¹
D₁ = 0.263 μm² s⁻¹
×10⁻³ Slowly moving I-E^k fraction
D₂ = 0.026 μm² s⁻¹
D₂ = 0.017 μm² s⁻¹
F
****
****
*
Relative fast I-E^k fraction
D_fast I-E^k (μm² s⁻¹)
D_slow I-E^k (μm² s⁻¹)
Activated BMDC
Activated B-cell
G
BMDC or B-cell
I-E^k
14.4.4scF_V-biotin
mSav -abCAGE635
ICAM-1
405 nm
Coverglass
IRM or TIRF excitation
H
405 nm pulse
IRM
1 s before
1 s after
30 s after
60 s after
120 s after
Full conversion
Activated BMDC
Activated B-cell
I_out
I_in
200 1,500
200 4,000
200 1,500
200 1,500
200 1,500
200 12,000
200 4,000
200 20,000
200 6,000
200 4,000
200 4,000
200 40,000
Intensity (counts)
I
Activated BMDCs
Activated B-cells
I_out / I_in
Time lag = 30 s
Time lag = 5 s
Time after 405 nm pulse (s)
Relative mean fluorescence intensity in the photoactivated region (I_in)

Figure 3.

Figure 3. Surface-resident I-E^k molecules are to 99% mobile with 60–75% displaying fast diffusion immediately after entering the cell surface.

A Schematic illustration of a single-molecule tracking experiment to monitor the diffusion of single I-E^k molecules within the plasma membrane of activated BMDCs and B-cells at 37°C. Cells were stained with an I-E^k-specific AF555-conjugated 14.4.4 scF$_V$ and seeded on ICAM-1-coated glass slides. Single I-E^k molecules were tracked over time with a time lag of 10.2 or 10.5 ms to study the mobility of I-E^k.

B Visualization of single I-E^k trajectories on the surface of representative BMDCs and B-cells. Trajectories were color-coded according to their lateral velocity. Scale bar, 1 μm.

C Histogram of diffusion constants derived from individual I-E^k trajectories on BMDCs and B-cells. Number of trajectories (length 2–50 steps): n = 36,023 (BMDCs); n = 14,607 (activated B-cells), and binning = 0.05. These data were pooled from two biological replicates with a total of n = 43 BMDCs and n = 41 B-cells.

D Mean square displacement plot of recorded I-E^k trajectories shown in (C). D = diffusion constant (fitted through the first two data points). Statistics: mean and standard deviation.

E Binary diffusion model to describe heterogenous I-E^k diffusion of trajectories shown in (C). Left panel: Relative fraction of fast- and slowly moving I-E^k molecules on activated BMDCs and B-cells were calculated by fitting the recorded I-E^k trajectories to a binary diffusion model. Middle and right panel: Mean square displacement plot of fast-moving I-E^k molecules (middle panel) and slowly moving I-E^k molecules (right panel). F = fraction of fast-moving molecules. D_1 = diffusion constant of fast-moving molecules. D_2 = diffusion constant of slowly moving molecules. Diffusion constants were extracted by fitting the first two data points. Fractions were calculated by fitting the first 10 data points. Statistics: mean and standard deviation.

F Quantification of the binary diffusion data (E) on individual activated BMDCs and B-cells. Each circle represents the mean of all recorded I-E^k trajectories of a single cell (n = 43 BMDCs and n = 41 B-cells pooled from two biological replicates), after being categorized by the binary fit. Data points outside the axis limits are marked with a plus (+). Statistics: mean and standard deviation; unpaired two-tailed Student's t-test. P-value format: $P \leq 0.05$ (*), $P \leq 0.0001$ (****).

G Scheme illustrating the use of inverse fluorescence recovery after photobleaching (iFRAP) to assess cell surface spreading of I-E^k. Activated BMDCs were stained with site-specifically biotinylated 14.4.4 scF$_V$ (14.4.4 scF$_V$-biotin) for detection with site-specifically conjugated mSav-abCAGE635, a photo-switchable and photo-stable bright fluorophore that allowed for tracking of individual molecules from a particular region of interest after photo-switching with a short 405 nm laser pulse. Stained BMDCs were seeded onto ICAM-1-coated glass slides for recordings in TIRF mode at 37°C.

H Shown are representative time-lapse montages of I-E^k-conjugated mSav-abCAGE635 photo-converted within the indicated circular ROI (I_{in}) on the surface of an activated BMDC and B-cell. Scale bars, 5 μm.

I Over 70–90% of I-E^k-bound mSav-CAGE635 dispersed over the entire APC surface within 150 s after photo-conversion of a small region of interest. Left panel: Shown is the ratio between the background-subtracted mean intensity of a dark cell region (I_{out}) and the photo-converted region (I_{in}) recorded either with a long (30 s) or a short (5 s) time delay. Statistics: mean and standard error of the mean of 10 to 14 cells (for each delay) from one experiment. Right panel: Decline in the fluorescence intensity within the photoactivated region (I_{in}). Shown is mean fluorescence intensity which had been background-subtracted and corrected for photobleaching (3% per image). Statistics: mean and standard deviation of n = 10 to 14 cells (for each delay) from one experiment.

Source data are available online for this figure.

of Labeling" (TOCCSL) methodology, a live cell-compatible single-molecule fluorescence recovery after photobleaching (FRAP) approach, which affords identification and quantification of laterally mobile higher order entities at high surface densities (Moertelmaier *et al*, 2005; Brameshuber *et al*, 2010, 2018). For TOCCSL measurements, we stained activated BMDCs and B-cells with saturating quantities of the 14.4.4 scF$_V$-AF647 and then allowed the cells to spread on ICAM-1-coated glass slides for imaging in TIRF mode. To ensure quantitative decoration of cell surface-resident I-E^k with the 14.4.4-scF$_V$, we conducted TOCCSL experiments at 25°C (a temperature at which 14.4.4-scF$_V$ exhibited a half-life of binding of ~80 min) and only between 2 and 20 min after the cells had landed on the glass slide. As is illustrated in Fig 5A, we subjected cells to a laser-based TOCCSL illumination sequence, which included a high-powered laser pulse (750–1,000 ms) to quantitatively ablate the AF647 fluorescence of a spatially defined area, to be succeeded by the acquisition of a control image 100–750 ms after bleaching for verification of complete AF647 photobleaching (Fig 5A, center panel). Following a recovery phase of 2–20 s, we recorded a so-termed TOCCSL image representing isolated diffraction-limited spots. These originated from the masked area of the cell surface as laterally mobile I-E^k entities and had therefore not undergone bleaching (Fig 5A, right panel). To enumerate the number of 14.4.4-scF$_V$-AF647-decorated I-E^k molecules per diffraction-limited signal, we compared the obtained distribution of AF647 fluorescence brightness values $\rho(B)$ with the brightness values obtained from recorded cells decorated with AF647-conjugated and unconjugated 14.4.4-scF$_V$ premixed at a ratio of 15:1 as monomer control ($\rho 1$). A linear combination of multimeric n-mer contributions, ρn, derived from $\rho 1$ and applied to fit the distribution $\rho(B)$ yielded exclusively I-E^k monomers (Fig 5B). To determine the overall capacity of the TOCCSL procedure to reveal the existence of diffraction-limited entities exhibiting more than one fluorophore, we imaged cells that we had decorated with 14.4.4-scF$_V$-AF647-biotin preconjugated with mSav-AF647. This regimen gave invariably rise to events associated with two AF647 dyes, and as shown in Fig 5B, 19 and 30% of the events recorded in this fashion on activated BMDCs and activated B-cells, respectively, reflected dimers. The moderate detection efficiency, especially in the case of activated BMDCs, resulted in all likelihood from fast lateral I-E^k diffusion during the application of the TOCCSL bleach pulse, which appeared to have led to a relatively high number of partially ablated dimeric events at the interface of the bleached and the masked area, and which we confirmed in Monte-Carlo–based TOCCSL simulations (Appendix Fig S14A). Similarly, crosslinking of I-E^k-associated biotinylated 14.4.4 scF$_V$-AF647 with 125 nM divalent streptavidin revealed a dimer fraction of 20% on activated BMDCs (Fig 5C).

To also account for the less abundant yet more slowly diffusing pMHCIIs, which might have escaped detection by the TOCCSL method, we employed FRET as a readout for spatial proximity between surface-resident pMHCII. To this end, we quantitatively decorated I-E^k molecules on BMDCs, B-cells, and functionalized planar glass-supported lipid bilayers (PLBs) with 14.4.4 scF$_V$s, which had been site-specifically conjugated with either AF555 or AF647 serving as FRET donor and acceptor, respectively. For most direct FRET yield quantitation, we recorded FRET donor recovery after FRET acceptor photobleaching (FRET DRAAP). We anticipated FRET yields to augment with increasing FRET acceptor abundance, yet we also had to factor in decreasing signal-to-noise ratios with decreasing FRET donor surface densities. We therefore applied

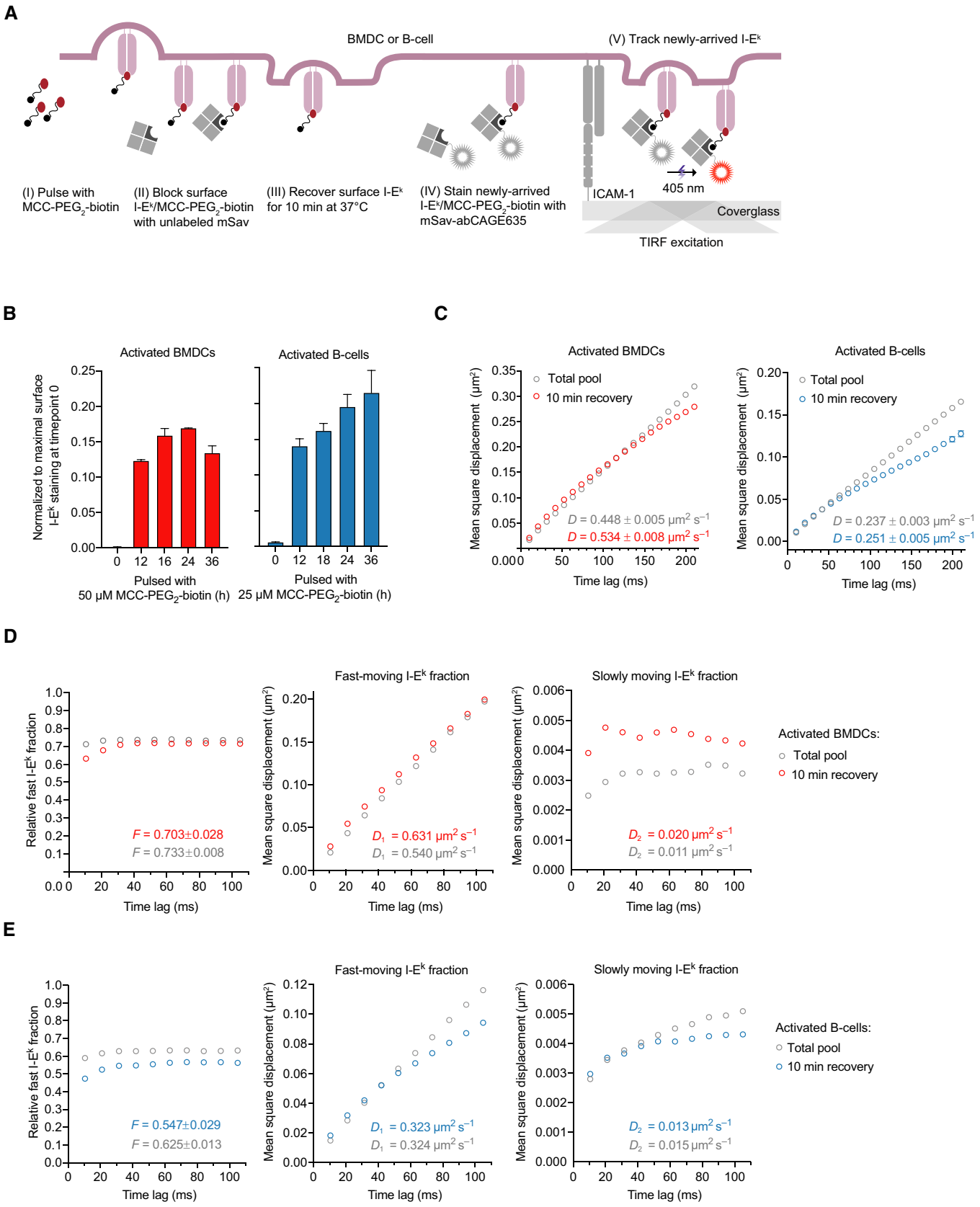
A
BMDC or B-cell
(V) Track newly-arrived I-Eᵏ
(I) Pulse with MCC-PEG2-biotin
(II) Block surface I-Eᵏ/MCC-PEG2-biotin with unlabeled mSav
(III) Recover surface I-Eᵏ for 10 min at 37°C
(IV) Stain newly-arrived I-Eᵏ/MCC-PEG2-biotin with mSav-abCAGE635
ICAM-1
405 nm
Coverglass
TIRF excitation
B
Activated BMDCs
Activated B-cells
Normalized to maximal surface I-Eᵏ staining at timepoint 0
Pulsed with 50 µM MCC-PEG2-biotin (h)
Pulsed with 25 µM MCC-PEG2-biotin (h)
C
Activated BMDCs
Activated B-cells
Total pool
10 min recovery
Mean square displacement (µm²)
Time lag (ms)
D = 0.448 ± 0.005 µm² s⁻¹
D = 0.534 ± 0.008 µm² s⁻¹
D = 0.237 ± 0.003 µm² s⁻¹
D = 0.251 ± 0.005 µm² s⁻¹
D
Relative fast I-Eᵏ fraction
Fast-moving I-Eᵏ fraction
Slowly moving I-Eᵏ fraction
F = 0.703±0.028
F = 0.733±0.008
D1 = 0.631 µm² s⁻¹
D1 = 0.540 µm² s⁻¹
D2 = 0.020 µm² s⁻¹
D2 = 0.011 µm² s⁻¹
Activated BMDCs:
Total pool
10 min recovery
E
F = 0.547±0.029
F = 0.625±0.013
D1 = 0.323 µm² s⁻¹
D1 = 0.324 µm² s⁻¹
D2 = 0.013 µm² s⁻¹
D2 = 0.015 µm² s⁻¹
Activated B-cells:
Total pool
10 min recovery

Figure 4.

Figure 4. Newly arriving I-E^k molecules are not confined and feature a similar diffusion behavior as the total pool of I-E^k molecules.

A Scheme illustrating the experimental procedure applied. (i) Activated BMDCs and B-cells were pulsed with MCC-PEG$_2$-biotin. (ii) Resulting I-E^k/MCC-PEG$_2$-biotin molecules on the cell surface were blocked with unlabeled mSav after the initial peptide pulse (6–12 h). (iii) Following a recovery lasting 10 min at 37°C, newly arrived and surface-exposed I-E^k/MCC-PEG$_2$-biotin molecules were stained with mSav-abCAGE635 at room temperature, washed, and (iv) directly subjected to single-molecule tracking analysis.

B To determine the duration of peptide-loading most adequately for tracking experiments (analysis in C–E), we quantitated the degree of I-E^k-peptide loading on activated BMDCs and B-cells by flow cytometric analysis. Cells were pulsed with MCC-PEG$_2$-biotin for up to 36 h and then stained with either 14.4.4 scF$_V$-AF647 (reflecting all surface-resident I-E^k molecules) or mSav-AF647 (marking I-E^k loaded with MCC-PEG$_2$-biotin). Ratios were built from MFIs measured for either scF$_V$-AF647- or mSav-AF647-decorated cells to determine the proportion of surface-accessible I-E^k molecules loaded with MCC-PEG$_2$-biotin. Statistics: mean and standard deviation of two technical replicates.

C Activated BMDCs and B-cells pulsed with MCC-PEG$_2$-biotin for 12 and 6 h, respectively, were stained with mSav-abCAGE635 and seeded on ICAM-1-coated glass slides for imaging in TIRF mode at 37°C. Single I-E^k/MCC-PEG$_2$-biotin molecules were tracked over time with a time lag of 10.5 ms. The graphs demonstrate the mean square displacement of the total pool and newly arrived I-E^k molecules on activated BMDCs (10,051 trajectories on 14 cells, total pool; 8,607 trajectories on 13 cells, 10 min recovery) and activated B-cells (11,312 trajectories on 16 cells, total pool; 8,974 trajectories on 15 cells, 10 min recovery). Data are representative of one (BMDCs) and two (B-cells) biological replicates. Diffusion constants D were calculated based on the first two data points. Fractions were calculated by fitting the first 10 data points. Statistics: mean and standard deviation.

D, E Fast-moving fraction of newly arriving and the total pool of I-E^k molecules on activated BMDCs (D) and activated B-cells (E) were calculated by fitting the recorded I-E^k trajectories to a binary diffusion model (left panel). Mean square displacement plot of fast-moving I-E^k molecules (middle panel) and slowly moving I-E^k molecules (right panel) are plotted for the indicated time lags employed in the tracking experiments. Statistics: mean and standard deviation. F = fraction of fast-moving molecules. D_1 = diffusion constant of fast-moving fraction. D_2 = diffusion constant of slowly moving fraction. Diffusion constants were calculated by fitting the first two data points. Fractions were calculated by fitting the first 10 data points.

Source data are available online for this figure.

AF555- and AF647-conjugated 14.4.4 scF$_V$s in our staining procedures at molar ratios of 1:1, 1:2, 1:3, and 1:4 with expected FRET detection efficiencies of 66.7, 80, 85.7, and 88.9% and signal recovery of 50, 44.4, 37.5, and 32%, respectively (Fig 5D–G and Appendix Fig S14B–D). To quantitate the I-E^k density on BMDCs and B-cells with and without the use of FRET acceptor probe (14.4.4 scF$_V$-AF647), we measured the density of I-E^k bound to the FRET donor probe (14.4.4 scF$_V$-AF555) for every scenario and related loss of the FRET donor intensity with the gain in FRET acceptor intensity. As shown in Appendix Fig S14B, the use of FRET donor and FRET acceptor probes premixed at a ratio of 1:1 led to a twofold reduction in FRET donor intensity (as determined after FRET acceptor ablation), confirming that the density of all I-E^k was twofold higher than the density measured for FRET donor probe-associated I-E^k.

We next compared FRET efficiencies measured on cells and PLBs via FRET donor recovery after acceptor photobleaching with simulated FRET efficiencies we had calculated from monomeric and randomly distributed molecules present at comparable densities. As shown in Fig 5D and E, and Appendix Fig S14C and D, we failed to observe in our cell-based measurements significant deviations from FRET efficiencies as expected from random molecular collisions. Yet, validating the use of our FRET-based approach to score for higher order I-E^k entities, we witnessed a considerable increase in FRET efficiency after crosslinking I-E^k-bound biotinylated 14.4.4 scF$_V$ (14.4.4 scF$_V$-AF555-biotin and 14.4.4 scF$_V$-AF647-biotin premixed in a 1:1 ratio) on activated BMDCs via divalent streptavidin (Fig 5F and G).

In summary, both TOCCSL- and FRET-based analyses rendered the existence of mobile and immobile I-E^k higher order structures, at least at frequencies that would be relevant for T-cell detection, highly unlikely.

TCR interactions by endogenous bystander pMHCIIs are indistinguishable from random molecular collisions

We conjectured that, if they exist, co-agonist pMHCIIs engage TCRs within the immunological synapse as a means to sensitize T-cells for rare antigens. To test this, we quantitated synaptic TCR engagement of previously reported co-agonist pMHCIIs with the use of a FRET-based imaging approach previously employed to deduce the molecular dynamics of TCR-pMHCII engagement *in situ* at the ensemble and single molecule level (Huppa *et al*, 2010). For this, we confronted primary TCR-transgenic T-cells with protein-functionalized PLBs, which served as surrogate APCs and recapitulated scenarios of free diffusion and random distribution of pMHCIs, in line with our observations concerning living APCs described above. Of note, the use of PLBs did not only provide full control over the identity and quantity of synaptic T-cell-binding partners but was also compatible with the use of TIRF microscopy, which afforded considerably improved signal-to-noise ratios when recording individual synaptic TCR-pMHCII interactions via single-molecule FRET (Huppa *et al*, 2010).

For FRET measurements, we first decorated 5c.c7 TCR-transgenic T-cells with a site-specifically AF555-conjugated TCRβ-reactive H57-scF$_V$ serving as FRET donor and confronted them with PLBs functionalized with the costimulatory molecule B7-1, the adhesion molecule ICAM-1 and I-E^k complexed with either the agonist moth cytochrome C peptide 88–103 (MCC), MCC derivatives, or endogenous peptides for T-cell recognition (Fig 6A, first panel). Prior to MHC loading, presented peptides have been C-terminally conjugated with AF647 to act as FRET acceptors (for details, see Materials and Methods). With an AF555/AF647-Förster radius of ~5.1 nm, the inter-dye distance giving rise to half-maximal energy transfer, we reasoned that our labeling procedure resulted in measurable FRET only when TCR and pMHCII were engaged with one another (Fig 6A, second panel). Given the calculated inter-dye distance of approximately 4.1 nm within the 5c.c7 TCR-I-E^k/peptide complex (Fig 6A), we expected TCR-pMHCII engagement to result in a FRET yield of about 78% (Fig 6B and Appendix Fig S15A), which would be sufficiently high to visualize synaptic TCR-pMHCII interactions and quantitate their lifetime at the single molecule level (Appendix Fig S15B). In fact, ablation of AF647 gave indeed rise to an increase in AF555 FRET donor fluorescence as a direct measure for the FRET yield (Fig 6B and equations 7–10—see Materials and Methods part). The latter is proportional to the TCR occupancy, the proportion of

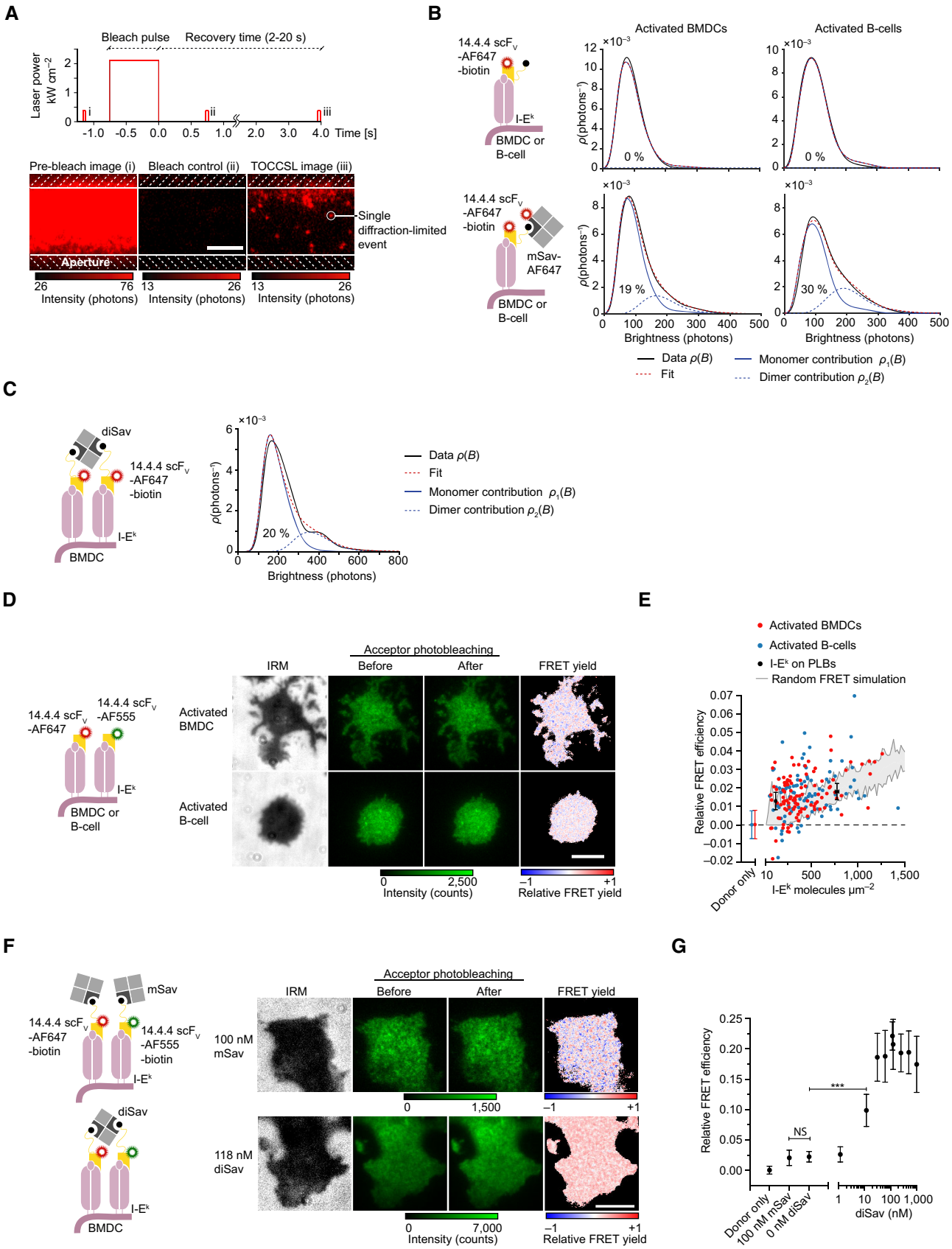
A
Bleach pulse
Recovery time (2-20 s)
Laser power kW cm−2
Time [s]
Pre-bleach image (i)
Bleach control (ii)
TOCCSL image (iii)
Aperture
Single diffraction-limited event
Intensity (photons)
B
14.4.4 scFV -AF647 -biotin
I-Ek
BMDC or B-cell
mSav-AF647
Activated BMDCs
Activated B-cells
ρ(photons−1)
0 %
19 %
30 %
Brightness (photons)
Data ρ(B)
Fit
Monomer contribution ρ1(B)
Dimer contribution ρ2(B)
C
diSav
14.4.4 scFV -AF647 -biotin
I-Ek
BMDC
20 %
Brightness (photons)
Data ρ(B)
Fit
Monomer contribution ρ1(B)
Dimer contribution ρ2(B)
D
14.4.4 scFV -AF647
14.4.4 scFV -AF555
I-Ek
BMDC or B-cell
Activated BMDC
Activated B-cell
Acceptor photobleaching
IRM
Before
After
FRET yield
Intensity (counts)
Relative FRET yield
E
Activated BMDCs
Activated B-cells
I-Ek on PLBs
Random FRET simulation
Relative FRET efficiency
Donor only
I-Ek molecules μm−2
F
mSav
14.4.4 scFV -AF647 -biotin
14.4.4 scFV -AF555 -biotin
I-Ek
diSav
BMDC
100 nM mSav
118 nM diSav
Acceptor photobleaching
IRM
Before
After
FRET yield
Intensity (counts)
Relative FRET yield
G
Relative FRET efficiency
Donor only
100 nM mSav
0 nM diSav
NS
***
diSav (nM)

Figure 5.

Figure 5. Surface-resident I-E^k molecules are monomeric.

A Principle of TOCCSL to study the stoichiometry of I-E^k on living BMDCs and B-cells. Cells were quantitatively labeled with the 14.4.4 scF$_V$-AF647, placed on an ICAM-1-coated glass slide for imaging, and subjected to an illumination sequence of (i) a prebleach image followed by a high-powered laser pulse to quantitatively ablate the AF647 fluorescence of a particular cell area (as defined by the slit aperture). (ii) Complete photobleaching of AF647 was verified by a control image 100–750 ms after the bleach pulse. (iii) Following a recovery phase of 2–20 s, we next recorded TOCCSL images to detect single diffraction-limited events resulting from laterally mobile I-E^k molecules, which had moved from the masked into the unmasked area. Finally, the brightness of individual fluorescence events was determined to assess I-E^k-complex stoichiometry (shown in B, C). Scale bar, 5 μm.

B Quantitative brightness analysis revealed a monomeric contribution of recovered I-E^k molecules on BMDCs (n = 471 molecules on 59 cells) and B-cells (n = 187 molecules on 52 cells). As monomer control, we stained the cells with a cocktail of 14.4.4 scF$_V$-AF647-biotin and 14.4.4 scF$_V$-biotin (mixed 1:15) and recorded n = 441 molecules on 50 BMDCs and n = 263 molecules on 57 B-cells. As dimer control, we stained BMDCs and B-cells with 14.4.4 scF$_V$-AF647-biotin and mSav-AF647 which increased the dimeric contribution of recorded fluorescent events to 19% on activated BMDCs (n = 541 molecules on 64 cells) and 30% on activated B-cells (n = 334 molecules on 61 cells). Data are representative of one (B-cells) and two independent experiments (BMDCs).

C TOCCSL measurement of I-E^k-bound 14.4.4 scF$_V$-AF647-biotin crosslinked with 125 nM divalent streptavidin on activated BMDCs. n = 301 molecules (monomer control) and n = 294 molecules (dimer control) derived from over 50 cells in one experiment.

D Activated B-cells and BMDCs were stained with a 1:1 premix of the 14.4.4 scF$_V$-AF555 and 14.4.4 scF$_V$-AF647 and seeded onto ICAM-1-coated glass slides for imaging in TIRF mode to probe molecular proximities of APC surface expressed pMHCIIs via FRET imaging. FRET donor intensity (green, background subtracted) was monitored before and after FRET DRAAP. FRET efficiencies were calculated on a pixel-by-pixel basis for attached membrane regions (see IRM image). Scale bar, 10 μm.

E FRET measurements of I-E^k on activated BMDCs, B-cells, and PLBs. Activated B-cells and BMDCs were stained with a 1:1 premix of the 14.4.4 scF$_V$-AF555 and 14.4.4 scF$_V$-AF647. PLBs featuring I-E^k at indicated densities were decorated with I-E^k/MCC-AF555 and I-E^k/MCC-AF647 premixed 1:1. Density-dependent FRET efficiencies estimated from randomized molecular pMHCII encounters through Monte-Carlo simulations are shown in gray for FRET donor and acceptors present at a 1:1 ratio. Each dot represents the mean FRET value determined for an individual cell. Error bars represent mean and standard deviation of n = 71 BMDCs, n = 131 B-cells (donor only), and n = 30–34 PLB positions. Upper and lower boundaries of the gray area represent range for n = 20 simulations per data point. Data were pooled from three (BMDCs) and two (B-cells) biological replicates.

F, G Activated BMDCs were stained with 14.4.4 scF$_V$-AF555-biotin and 14.4.4 scF$_V$-AF647-biotin premixed at a 1:1 ratio. Dimerization of biotinylated scF$_V$s was induced with divalent streptavidin at increasing concentrations and quantified via FRET DRAAP. The addition of monovalent streptavidin (mSav) did not crosslink the 14.4.4-scF$_V$-biotin molecules. Data were pooled from two biological replicates. Statistics: mean and standard deviation and unpaired two-tailed Student's t-test. P-value format: $P > 0.05$ (NS), $P \leq 0.001$ (***). Scale bar, 10 μm.

Source data are available online for this figure.

pMHCII within the synapse that is bound to TCRs (Appendix Fig S15C–G and Axmann *et al*, 2015).

Figure 6C displays TCR occupancies as they had been measured for 5c.c7 TCR transgenic T-cells recognizing I-E^k loaded with the agonist MCC peptide, the weak agonistic T102S, the antagonistic K99R, or the reported co-agonist K99A MCC peptide variant (Matsui *et al*, 1994; Wulfing *et al*, 1997, 2002). We also included measurements involving the recognition of I-E^k complexed with the endogenous peptides ER60 and β2m (Ebert *et al*, 2009). I-E^k displaying the triple-null MCC mutant, which no longer binds the 5c.c7 TCR (ANERAELIAYLTQAAK, null peptide), was employed as a negative control to determine FRET yields resulting solely from molecular crowding.

Consistent with their stimulatory potency and the TCR occupancies measured, the agonist I-E^k/MCC and weak agonist I-E^k/T102S rapidly accumulated underneath T-cells, which was followed by their recruitment to the central supramolecular activation cluster. In contrast, the antagonist I-E^k/K99R became only slightly enriched, while non-stimulatory I-E^k/K99A, I-E^k/ER60, I-E^k/β2m, and I-E^k/null failed altogether to accumulate in the synapse and to induce the formation of a mature immune synapse (Appendix Fig S16A and B).

As shown in Fig 6C, synaptic TCRs became ligand engaged already at low densities of I-E^k/MCC and, to a lesser extent, I-E^k/T102S. Expectedly, we observed much reduced synaptic binding of I-E^k/K99R and especially of I-E^k/K99A, with median TCR occupancies of ∼5% at high densities (i.e., 1,390 I-E^k/K99A μm^{-2}or 1,611 I-E^k/K99R μm^{-2}). Of note, we failed to detect any synaptic binding of the endogenous ligands I-E^k/ER60 and I-E^k/β2m even when these had been present in numbers comparable to pMHCII expression levels on activated BMDCs and B-cells (median 400–500 I-E^k μm^{-2}, see Fig 1E). Challenging the notion of any co-agonistic potency associated with I-E^k/ER60 and I-E^k/β2m, measured FRET levels could merely be attributed to molecular crowding rather than TCR-binding, as they were indistinguishable from those determined for I-E^k/null.

Competition rather than cooperativity among agonist, "co-agonist", and weak agonist ligands defines synaptic pMHCII-TCR binding

To further test the conceptual validity of co-agonism, we assessed whether co-presentation of more weakly binding TCR ligands promotes or rather suppresses TCR binding of low-abundant agonist ligands.

Among all investigated co-agonist candidates, only I-E^k/K99A engaged a measurable fraction of synaptic TCRs, at least when present at ∼1,400 molecules μm^{-2} or higher. To evaluate whether I-E^k/K99A affected initial TCR binding to the lowly abundant agonist I-E^k/MCC, we loaded I-E^k with an AF647-conjugated derivative of the MCC peptide, which had been modified at the central lysine residue to contain a (4,5-dimethoxy-2-nitrophenyl)methyl carbonochloridate (NVOC) moiety (DeMond *et al*, 2006; Huse *et al*, 2007). As schematically illustrated in Fig 6D, NVOC sterically hinders I-E^k binding to the 5c.c7 TCR, unless it becomes ablated on demand through a brief violet (λ = 405 nm) laser pulse to release I-E^k/MCC for TCR engagement (DeMond *et al*, 2006). As is demonstrated in Fig 6D–F, T-cells did not engage the provided I-E^k/MCC[NVOC] until photo-uncaging had occurred.

To assess any influence of co-agonists on the TCR engagement by agonist ligands, we titrated I-E^k/K99A-AF488 in high abundance (417 ± 11 molecules μm^{-2}) to I-E^k/MCC[NVOC]-AF647 (92 ± 4 molecules μm^{-2}) and quantified I-E^k/MCC-TCR engagement by

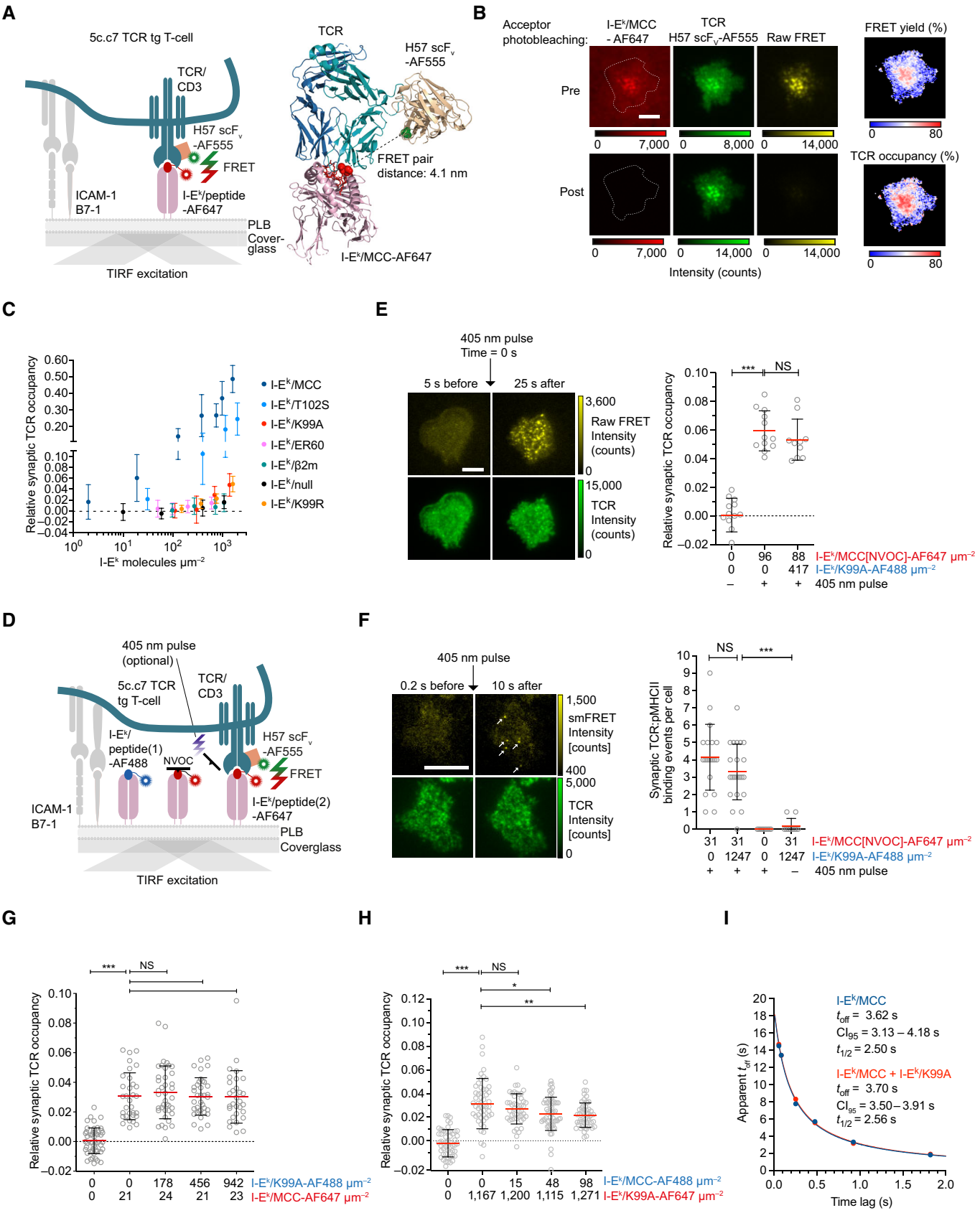
A
5c.c7 TCR tg T-cell
TCR/
CD3
H57 scFv
-AF555
FRET
ICAM-1
B7-1
I-Ek/peptide
-AF647
PLB
Cover-
glass
TIRF excitation
TCR
H57 scFv
-AF555
FRET pair
distance: 4.1 nm
I-Ek/MCC-AF647
B
Acceptor
photobleaching:
I-Ek/MCC
- AF647
TCR
H57 scFv-AF555
Raw FRET
FRET yield (%)
Pre
Post
0 7,000
0 8,000
0 14,000
0 80
TCR occupancy (%)
Intensity (counts)
C
Relative synaptic TCR occupancy
I-Ek molecules µm−2
I-Ek/MCC
I-Ek/T102S
I-Ek/K99A
I-Ek/ER60
I-Ek/β2m
I-Ek/null
I-Ek/K99R
D
405 nm pulse
(optional)
5c.c7 TCR
tg T-cell
TCR/
CD3
I-Ek/
peptide(1)
-AF488
NVOC
H57 scFv
-AF555
FRET
I-Ek/peptide(2)
-AF647
ICAM-1
B7-1
PLB
Coverglass
TIRF excitation
E
405 nm pulse
Time = 0 s
5 s before
25 s after
3,600
Raw FRET
Intensity
(counts)
0
15,000
TCR
Intensity
(counts)
0
Relative synaptic TCR occupancy
***
NS
0 96 88 I-Ek/MCC[NVOC]-AF647 µm−2
0 0 417 I-Ek/K99A-AF488 µm−2
– + + 405 nm pulse
F
405 nm pulse
0.2 s before
10 s after
1,500
smFRET
Intensity
[counts]
400
5,000
TCR
Intensity
[counts]
0
Synaptic TCR:pMHCII
binding events per cell
NS
***
31 31 0 31 I-Ek/MCC[NVOC]-AF647 µm−2
0 1247 0 1247 I-Ek/K99A-AF488 µm−2
+ + + – 405 nm pulse
G
Relative synaptic TCR occupancy
***
NS
0 0 178 456 942 I-Ek/K99A-AF488 µm−2
0 21 24 21 23 I-Ek/MCC-AF647 µm−2
H
Relative synaptic TCR occupancy
***
NS
*
**
0 0 15 48 98 I-Ek/MCC-AF488 µm−2
0 1,167 1,200 1,115 1,271 I-Ek/K99A-AF647 µm−2
I
Apparent toff (s)
Time lag (s)
I-Ek/MCC
toff = 3.62 s
CI95 = 3.13 – 4.18 s
t1/2 = 2.50 s
I-Ek/MCC + I-Ek/K99A
toff = 3.70 s
CI95 = 3.50 – 3.91 s
t1/2 = 2.56 s

Figure 6.

Figure 6. TCR-agonist binding is not affected by the presence of the reported co-agonist I-E^k/K99A.

A Scheme of a FRET-based assay to visualize TCR-pMHCII interactions *in situ*.

B FRET yields resulting from 5c.c7 TCR-transgenic T-cells stained with H57 scF$_V$-AF555 and interacting with PLBs featuring I-E^k/MCC-AF647 as determined via FRET DRAAP and FRET-sensitized emission. The FRET yield is directly proportional to the TCR occupancy, the ratio of bound TCRs to total TCRs. Scale bar, 5 μm.

C Synaptic TCR-ligand engagement was quantified at 25°C via FRET observed for H57 scF$_V$-AF555-decorated 5c.c7 TCR-transgenic T-cells engaging PLBs featuring agonist (MCC), weak agonist (T102S), antagonist (K99R), potential co-agonist (K99A, β2m, ER60), and non-binding (null) I-E^k molecules displayed at increasing densities. ICAM-1 and B7-1 were present at densities of ~100 molecules μm^{-2}. The TCR occupancy of the entire synapse was calculated according to TCR occupancy = $E_{FRET} \times 1.21$. Statistics: mean and standard deviation of $n = 13$–81 T-cell synapses recorded between 2 and 12 min after establishing PLB contact. Data were pooled from 1–2 biological replicates.

D Scheme of a FRET-based assay to analyze I-E^k/MCC-TCR-binding events in the presence or absence of bystander pMHCIIs with and without the use of a caged peptide (MCC[NVOC]).

E Relative synaptic TCR occupancy of T-cells approaching functionalized PLBs displaying the agonist I-E^k/MCC[NVOC]-AF647 together with I-E^k/K99A-AF488 as well as ICAM-1 and B7-1 (both 100 molecules μm^{-2}). Binding of the TCR to I-E^k/MCC-AF647 was quantitated 25 s after photo-uncaging via FRET DRAAP. Scale bar, 5 μm. Statistics: mean and standard deviation and unpaired two-tailed Student's *t*-test. Each gray circle represents a T-cell synapse ($n = 10$–13 cells) of one experiment. *P*-value format: $P > 0.05$ (NS), $P \leq 0.001$ (***).

F Single-molecule FRET analysis of T-cells approaching PLBs functionalized with the photoactivatable agonist I-E^k/MCC[NVOC]-AF647 in low abundance and I-E^k/K99A-AF488 in high abundance together with ICAM-1 and B7-1 (100 μm^{-1}). Ten seconds after the uncaging pulse, single-molecule FRET events were recorded and counted as individual TCR-I-E^k/MCC-binding events (white arrow) if they had disappeared within one frame during recording. Scale bar, 10 μm. Statistics: mean, standard deviation, and unpaired two-tailed Student's *t*-test. Each gray circle represents a T-cell synapse ($n = 10$–23 cells) of one experiment. *P*-value format: $P > 0.05$ (NS), $P \leq 0.001$ (***).

G Synaptic TCR occupancy of T-cells engaging I-E^k/MCC-AF647 in the presence of increasing densities of I-E^k/K99A-AF488. Statistics: mean, standard deviation, and unpaired two-tailed Student's *t*-test. Each gray circle represents a T-cell synapse ($n = 30$–52 cells) of one experiment. *P*-value format: $P > 0.05$ (NS), $P \leq 0.001$ (***).

H Synaptic TCR occupancy of T-cells engaging I-E^k/K99A-AF647 in the presence of increasing I-E^k/MCC-AF488 densities. Statistics: mean, standard deviation, and unpaired two-tailed Student's *t*-test. These data are representative of two experiments. Each gray circle represents a T-cell synapse ($n = 46$–61 cells) of one experiment. *P*-value format: $P > 0.05$ (NS), $P \leq 0.05$ (*), $P \leq 0.01$ (**), $P \leq 0.001$ (***).

I Synaptic lifetime of I-E^k/MCC-TCR interactions in the presence or absence of 1,060 I-E^k/K99A-AF488 μm^{-2} as measured via single-molecule FRET imaging at 26°C. Number of smFRET traces ($n = 135$–227) to calculate the apparent lifetime (app t_{off}) for each time lag (56, 84, 252, 476, 924, and 1,820 ms) are summarized in Appendix Fig S17E.

Source data are available online for this figure.

means of FRET DRAAP 25 s after application of the uncaging 405 nm pulse. As can be appreciated from Fig 6E, the presence of I-E^k/K99A-AF488 did not increase TCR-agonist interactions during synapse formation. To assay earliest TCR-pMHCII-binding events, we titrated I-E^k/K99A-AF488 in high abundance (1,247 ± 12 molecules μm^{-2}) to I-E^k/MCC[NVOC]-AF647 (31 ± 0 molecules μm^{-2}) and recorded the appearance of single-molecule FRET events after photo-uncaging. As shown in Fig 6F, the presence of I-E^k/K99A-AF488 did also not significantly affect the frequency of initial TCR-agonist binding (i.e., detected single TCR-pMHCII-binding events via single-molecule FRET imaging), rendering scenarios in which bystander pMHCIIs boost the detection of rare agonist ligands in early synapses highly unlikely.

To assess whether bystander pMHCIIs influenced synaptic TCR binding of rare agonist pMHCIIs at later stages of synapse formation (i.e., between 2 and 12 min), we measured via FRET TCR-agonist binding on PLBs featuring no or increasing levels of I-E^k/K99A. As is shown in Fig 6G, synaptic 5c.c7 TCR-I-E^k/MCC binding was not affected by the presence of up to 942 I-E^k/K99A μm^{-2}, even when agonist ligands were outnumbered by the co-agonist candidates up to 40-fold. Vice versa, 5c.c7 TCR binding to I-E^k/K99A-AF647 present in high numbers (1,188 ± 65 molecules μm^{-2}) dropped appreciably with increasing numbers of co-presented agonist I-E^k/MCC-AF488 (Fig 6H). This proved also true for synaptic engagement of the weak agonist I-E^k/T102S-AF647 (present at a density of 1,053 ± 55 I-E^k/T102S), which diminished with increasing densities of co-presented agonist I-E^k/MCC (ranging from 0 to 202 I-E^k/MCC μm^{-2}, Appendix Fig S17A). In a similar fashion, 5c.c7 TCR binding to I-E^k/MCC-AF647 (presented at 36 ± 1 I-E^k/MCC) dropped substantially with increasing densities of I-E^k/T102S-AF488 (up to 1,235 I-E^k/T102S μm^{-2}, Appendix Fig S17B). We observed a similar trend for the antagonist I-E^k/K99R, which predictably competed more strongly with agonist binding than I-E^k/K99A yet to a lesser extent than I-E^k/T102S (Appendix Fig S17C and D). Of note, high densities of I-E^k/K99A (1,060 I-E^k/K99A-AF488 μm^{-2}) did not affect the synaptic lifetime of agonistic TCR:I-E^k/MCC interactions as measured via smFRET imaging (Fig 6I and Appendix Fig S17E).

Taken together, our FRET-based synaptic binding studies render the notion that TCR-engagement of low-affinity pMHCII ligands promotes the binding of rare agonist ligands highly improbable. Instead, and as would be expected from applying the law of mass action, high-affinity ligands outcompeted low-affinity ligands for TCR binding, especially under conditions where pMHCIIs outnumbered TCRs. Our findings are best explained with a scenario in which pMHCIIs engage TCRs in an autonomous fashion.

Highly abundant bystander pMHCIIs do not sensitize T-cells for low levels of agonist pMHCIIs

As shown above, we have detected higher order I-E^k structures on the surface of activated BMDCs and B-cells only after their specific and experimentally defined crosslinking. In addition, we did not detect any influence of bystander pMHCIIs on the kinetics of synaptic TCR engagement of rare agonist pMHCIIs. To be able to arrive at a definitive evaluation of endogenous or (low-affinity) bystander pMHCIIs with regard to their role in sensitized agonist detection, we stimulated T-cells with a defined APC mimetic biointerface (Fig 7A). The latter involved PLB-embedded and laterally mobile yet structurally rigid DNA origami platforms, which we had engineered to control for pMHCII identities and inter-pMHCII distances at the nanoscale level and which allowed for the spatially defined display of I-E^k molecules loaded with agonist (MCC) and co-agonist (K99A)

peptides (Hellmeier *et al*, 2021a, 2021b). More specifically and as shown in Fig 7A, we built rectangular DNA origami tiles of 100 × 70 nm in size, with either a single or two functionalization sites at 10 and 20 nm distance on the top side and attachment sites for cholesterol–DNA at the bottom side for PLB anchorage (for details, please see Materials and Methods section). To create defined pMHCII homodimers, DNA origami structures were functionalized with biotinylated oligonucleotides, divalent streptavidin, and biotinylated pMHCII; for heterodimers, we preassembled DNA-conjugated monovalent streptavidin and biotinylated pMHCIIs prior to DNA origami decoration.

As shown in Fig 7A, both strategies allowed for site-specific DNA origami attachment of I-E^k/MCC-AF555 or I-E^k/K99A-AF647. Biotinylated I-E^k/MCC-AF555, which had been attached to poly-histidine-tagged monovalent streptavidin, served as control for monomeric pMHCII. Engineered ligand occupancies of DNA origami-based platforms were verified by comparing the brightness of single DNA origami platforms to single fluorescence emitters recorded via TIRF-based microscopy. As shown in Appendix Table S1A, we arrived at a functionalization efficiency of ∼60% for a single modification site; for two modification sites, we detected a mixed population of DNA origami structures featuring one (∼20%), two (∼50%), and zero ligands (∼10%).

To gauge the impact of homo- or heterodimerization of pMHCIIs on T-cell activation, we loaded 5c.c7 TCR transgenic T-cells with the ratiometric calcium-sensitive dye Fura-2-acetoxymethyl (AM) ester (Fura-2) and allowed the cells to engage PLBs displaying functionalized DNA origami platforms at increasing densities and ICAM-1 and B7-1 at densities of ∼100 molecules μm^{-2} (Fig 7B). Ligand densities on PLBs were quantitated by dividing the average fluorescence brightness per area by the average brightness of single fluorophores. TCR-agonist pMHCII binding resulted in TCR-proximal signaling as witnessed by increasing levels of intracellular calcium acting as second messenger to promote T-cell activation.

For quantitative analysis, we calculated Fura-2 intensity ratios for each T-cell trace and classified the T-cells as activated or non-activated based on a receiver operating curve between a positive control (i.e., > 10 I-E^k/MCC μm^{-2}, ICAM-1 and B7-1 at 100 μm^{-2}) and a negative control (ICAM-1 and B7-1 at 100 μm^{-2}). For better display of low-level calcium signaling in individual T-cells, we identified the maximum Fura-2 ratio in each cell trace and plotted the median value of the peak Fura-2 ratio (i.e., median of the peak Fura-2 ratio plus 10 imaging frames) in a probability density plot (see Materials and Methods and Appendix Fig S18A). Non-activated T-cells featured median Fura-2 intensity ratios of 1.0 (after normalization to the median value representing the negative control), whereas oscillatory or activated T-cells exhibited median Fura-2 ratios ranging from 1.3 to 4.0 (Appendix Fig S18A). In Fig 7B and C, we plotted the fraction of activated T-cells as dose–response curves as a means to determine activation thresholds, that is, ligand densities that had given rise to half-maximum responses. To this end, we fitted the data with a four-parameter dose–response curve (for more information, see Materials and Methods, equation (12); all fit parameters are listed in Appendix Table S1B).

When confronted with I-E^k/MCC-AF555 tethered to monovalent streptavidin, T-cells responded at density of 0.33 molecules μm^{-2} (Fig 7C). Attachment of either a single or two I-E^k/MCC-AF555 molecules to a DNA origami platform did not lower but rather slightly increased the activation threshold to 0.4 and 0.48 molecules μm^{-2}, respectively. Likewise, confronting T-cells with DNA origami platforms that featured a single I-E^k/MCC-AF555 as well as a single I-E^k/K99A-AF647 molecule spatially separated by either 10 or 20 nm did not significantly affect activation threshold with values amounting to 0.34 and 0.46 molecules μm^{-2}, respectively. Of note, T-cells failed to respond to I-E^k/K99A when displayed in the absence of the agonist ligand I-E^k/MCC at ∼100 molecules μm^{-2} (Fig 7B).

Taken together, pre-organization of two agonist pMHCIIs or one agonist pMHCII and one co-agonist pMHCII did not measurably alter the activation threshold of agonist pMHCIIs in 5c.c7 TCR transgenic T-cells (see Appendix Table S1C for significance table). We hence conclude that T-cell activation was independent of ligand spacing.

We next assessed whether bystander pMHCIIs in high abundance can trigger low-level calcium signaling in T-cells, which may ultimately affect overall TCR-proximal signaling in the presence of limiting agonist ligands. To test this, we recorded changes in intracellular calcium in 5c.c7 TCR transgenic T-cells in response to increasing densities of I-E^k loaded with the agonist peptide MCC, the weak agonist T102S, the co-agonist K99A, the endogenous peptides ER60 and β2m, the antagonist K99R, as well as the null peptide (Fig 7D and E).

As shown in Appendix Fig S18B, the endogenous ligands I-E^k/ER60, I-E^k/β2m, and I-E^k/null failed to trigger T-cell calcium signaling, even when displayed on the PLB at densities higher than 1,000 molecules μm^{-2}, as Fura-2 ratio values were comparable to those recorded in the absence of pMHCIIs. The MCC-based altered peptide ligands (APLs) K99A and K99R induced low-level oscillatory calcium signaling patterns when presented at supraphysiological densities above 1,000 molecules μm^{-2} (Appendix Fig S18B).

To assess whether TCR-proximal signaling in response to limiting numbers of agonist ligands was affected by bystander pMHCIIs co-presented in high abundance, we exposed T-cells to PLBs functionalized with I-E^k/MCC in low numbers (∼1 molecule μm^{-2}) together with ICAM-1, B7-1, and high numbers of I-E^k loaded with T102S, K99A, K99R, ER60, β2m, or the non-binding null peptide. As expected, I-E^k/T102S acted as weak agonist: when present in high abundance, it increased the number of fully activated T-cells as well as the overall calcium signaling capacity (Fura-2 ratio) and accelerated furthermore the onset of signaling. Quite in contrast, endogenous I-E^k/ER60 and I-E^k/β2m, as well as I-E^k/K99A, I-E^k/K99R, and I-E^k/null, did not affect calcium response parameters even when present in more than 1,000-fold excess (Fig 7E and Appendix Fig S18C). Furthermore, T-cells displayed comparable, if not identical dose–response curves toward the agonist I-E^k/MCC, regardless of the absence or presence of I-E^k/K99A, I-E^k/ER60, or I-E^k/null (Fig 7F, and Appendix Fig S19A and B).

In summary, our findings challenge the very concept of pMHCII co-agonism and underscore the stimulatory potency of single, freely diffusing agonist pMHCIIs, as these activated T-cells in a peptide-specific manner and without contributions from endogenous bystander pMHCIIs.

Discussion

Advances in our understanding of T-cell antigen recognition and the extent to which it might be sensitized by pMHCII nanoscale

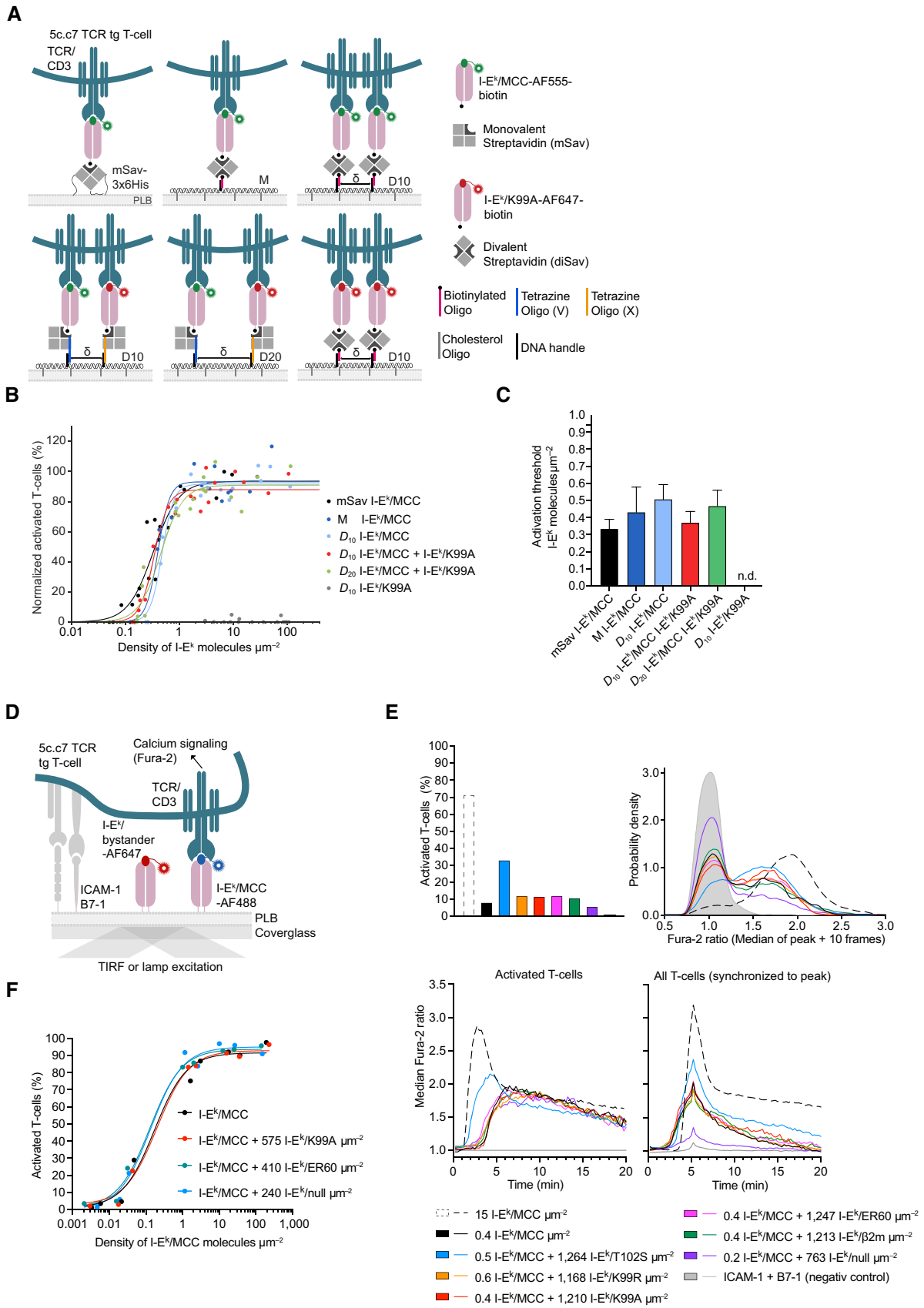

Figure 7.

Figure 7. Rare antigenic pMHCIIs are recognized by T-cells independently of highly abundant bystander pMHCIIs.

A Strategies for the site-specific functionalization of DNA origami structures (70 × 100 nm) with biotinylated I-E^k/MCC and I-E^k/K99A molecules to investigate the effect of ligand spacing (D_{10} = 10 nm, D_{20} = 20 nm) on T-cell activation.

B Dose–response curves for T-cell activation mediated by I-E^k/MCC displayed in the absence or presence of the co-agonist I-E^k/K99A and in the context of the mSav platform or different DNA origami constructs. Each data point corresponds to the percentage of activated T-cells determined in an individual experiment at a specific I-E^k/MCC density. Data were normalized to activation levels recorded for positive control (=100%) involving the use of PLBs featuring I-E^k/MCC at a density of 150 molecules μm^{-2} together with ICAM-1 and B7-1 at 100 molecules μm^{-2}. Data are representative of >2 biological replicates with the use of antigen-experienced T-cells isolated from 3–4 different 5c.c7 TCR-transgenic mice (Appendix Table S1B).

C Dose–response curves were fitted with equation (12) to extract the activation threshold (T_A, i.e., pMHCII density at half-maximum response, EC50). Statistics: mean and standard deviation (from a bootstrapping analysis). For each dose–response curve, data were derived from at least two independent experiments involving T-cells isolated from at least three different mice. Results of the fit and the significance test of the T_A are summarized in Appendix Table S1B and C.

D Scheme illustrating the means by which intracellular calcium levels were recorded to assess the impact of highly abundant bystander pMHCIIs on the recognition of agonist pMHCIIs present in low abundance.

E Calcium response of T-cells in contact with PLBs featuring the agonist I-E^k/MCC at a density of 0.2–0.6 I-E^k/MCC μm^{-2}, bystander pMHCIIs at high densities (763 to 1,264 I-E^k μm^{-2}), as well as ICAM-1 and B7-1 (both present with 100 molecules μm^{-2}). Shown are percentage of activated T-cells (upper left), probability density plot of Fura-2 ratios of individual T-cells (upper right), mean Fura-2 ratios of activated T-cells over time (lower left), and mean Fura-2 ratios of the entire T-cell population synchronized to onset of signaling (indicated by the highest Fura-2 value within a given track; lower right). Data are representative of >3 biological replicates with the use of antigen-experienced T-cells (n = 233–814 cells per condition) and isolated from >3 different 5c.c7 TCR-transgenic mice (Appendix Fig S18B and C).

F Calcium response of antigen-experienced 5c.c7 TCR-transgenic T-cells (n = 62–441 cells per condition) exposed to increasing levels of the agonist I-E^k/MCC (n = 8–9 conditions) presented together at indicated densities with I-E^k/K99A, I-E^k/ER60, or I-E^k/null. Three-parameter dose–response curve fit is summarized in the source data.

Source data are available online for this figure.

organization on professional APCs have been stalled for the last decade, in large part because the readout of most biochemical and imaging approaches employed did not support quantitative conclusions at the molecular level in living cells. We have therefore combined minimally invasive molecular live-cell microscopy with the use of custom-prepared imaging probes to arrive at a meaningful spatiotemporal resolution in the millisecond and nanometer regimes without adversely affecting cellular integrity. Following this strategy, we demonstrated that APCs express pMHCIIs at high numbers which become quickly distributed over the entire cell surface as single stimulatory entities as soon as they arrive at the plasma membrane. Highly abundant endogenous pMHCIIs did not enhance TCR binding and T-cell detection of rare agonist pMHCIIs at early or later stages of synapse formation. Endogenous pMHCIIs need to engage at least a fraction of TCRs in order to induce low-level signaling, which we observed only for MCC-derived APLs when these were presented to T-cells at exceptionally high densities. Together, this leaves us with the conclusion that single-agonist pMHCII entities elicit the full response of the scanning T-cell in a truly autonomous fashion. Following this concept, most efficient detection of rare agonist pMHCIIs would hence be best promoted by their rapid redistribution as soon as they arrive on the APC surface.

Central to the robustness of our analysis was the use of a monovalent and site-specifically fluorophore-conjugated (and optionally biotinylated) 14.4.4 mAb-derived scF$_V$, which targeted the pMHCII molecule I-E^k in a highly specific and stable manner. This allowed for tagging surface-resident I-E^k molecules with a single fluorescence emitter and supported quantitative analyses. We can exclude the possibility that we missed surface-resident I-E^k in significant numbers as antigen-pulsed APCs preabsorbed with 14.4.4-scF$_V$ effectively blocked T-cell activation at 37°C due to their direct and effective competition with TCRs for pMHCII binding.

Underscoring the validity of employing monovalent and site-specifically labeled scF$_V$s for quantitation, we detected 40 times more I-E^k molecules per APC (17 times more on B-cells and 40 times more on BMDCs) and also four- to fivefold higher molecular densities than previously reported with the use of phycoerythrin (PE)-conjugated full mAbs for cell staining (Unternaehrer *et al*, 2007). Given their large size, in particular when linked to PE, and their divalent nature, mAbs may be in part sterically hindered or bind instead of a single two pMHCIIs, which is plausible especially when facing exceedingly high epitope densities. Other possibilities may include non-quantitative PE conjugation or mAb linkage to photobleached PE, which together contrast the use of verifiably site-specifically dye-conjugated monomeric scF$_V$s, as done in our study.

It was speculated that the high density of pMHCIIs present in MIIC-derived vesicles on their anterograde transport to the cell surface may be preserved at least transiently after vesicle fusion with the plasma membrane to support sensitized T-cell detection (Bosch *et al*, 2013). Diffusion measurements of pulse-chased I-E^k as done in our study render such a scenario unlikely since 99% of newly arriving pMHCII molecules were mobile and dispersed over the entire APC surface within < 1 min. Single particle tracking revealed furthermore that 60–80% of pMHCIIs diffuse rapidly without any evidence of confinement. We examined whether the remaining fraction of more slowly diffusing pMHCIIs (20–40%) was associated with membrane entities such as sphingolipid rafts as had been previously reported (Anderson *et al*, 2000; Hiltbold *et al*, 2003; Knorr *et al*, 2009; Bosch *et al*, 2013). However, unlike Bosch *et al*, we failed to recover any surface I-E^k in DRMs to an extent that was larger than 1%, when applying a highly quantitative LGC centrifugation- and flowcytometry-based method. This implies that such association is either non-existent on the cell surface or too weak to be conserved when using the non-ionic detergent NP40 employed to discriminate between DRM-resident proteins (e.g., CD44 and CD55) and solubilized membrane proteins (e.g., CD71). Since we failed to co-isolate surface I-E^k with DRMs, as would be expected from raft-resident proteins, we consider transient I-E^k association with tetraspanins (Zuidscherwoude *et al*, 2014) or re-internalization (Ma *et al*, 2012) a likely cause for the observed reduction in lateral mobility.

Of note, living BMDCs and B-cells decorated with monovalent, site-specifically labeled 14.4.4-scF$_V$ did not feature in our hands any form of I-E^k clustering as was previously reported (Bosch *et al*, 2013), both above and below the diffraction limit. Decoration of living BMDCs and B-cells with randomly labeled I-E^k and I-A^k-reactive mAbs showed homogenous staining, whereas co-staining with secondary IgG mAbs produced a punctate appearance (Appendix Fig S5A and B). In view of our diffusion and TOCCSL analysis, we consider it likely that the use of divalent mAbs, a temperature shift from 37 to 0°C, and PFA fixation had in fact caused the reported dotted appearance of I-E^k.

Unlike what had been reported earlier (Turley *et al*, 2000; Bosch *et al*, 2013; Zuidscherwoude *et al*, 2015), neither hsPALM on living cells nor hsPALM and STED microscopy on fixed cells provided in our hands convincing evidence for clustered pMHCIIs on activated BMDCs and B-cells. Previous studies might have suffered from protein crosslinking as caused by antibodies applied at insufficient concentrations as well as by fixation artifacts impeding an unperturbed assessment of the pMHCII surface distribution. We circumvented these issues altogether by using monomeric and monovalent scF$_V$ to avoid receptor crosslinking, even when scF$_V$s had been applied at non-saturating conditions, and to allow for non-invasive labeling and imaging strategies. Moreover, we implemented an unbiased cluster analysis protocol that included every single localization and improved the detection of true nanoscale enrichments from false-positive clusters emerging as a result of continuously blinking photo-switchable fluorescent proteins (Baumgart *et al*, 2016; Platzer *et al*, 2020; Jensen *et al*, 2022). Contrary to our observations, a study involving STED microscopy reported exclusively pMHCII clusters on immature and activated APCs (Zuidscherwoude *et al*, 2015). It should be noted, however, that neither (i) the extent to which such reported pMHCII clusters differed in intensity from single molecule emitters nor (ii) the frequencies of their occurrence had been further compared to that of single pMHCIIs. By visually inspecting STED images of I-E^k present on activated BMDCs and B-cells, we did not observe a clustered appearance of pMHCIIs. In contrast, especially in areas with low surface density on the APC cell membrane, we detected most I-E^k molecules (i.e., 14.4.4 scF$_V$-abSTAR635P) as single events which gave rise to the same mean intensity and FWHM values as single fluorescence emitters.

A dimeric arrangement of pMHCIIs was suggested to be a potent mediator of sensitized detection of antigen by T-cells (Krogsgaard *et al*, 2005), yet without direct confirmation of the existence or the formation of higher order pMHCII structures within the plasma membrane of living APCs. In fact, despite using all available means we were unable to identify such entities on the surface of activated B-cells and BMDCs. This pertained to their detection via TOCCSL, for which they had to be stable for no longer than 2–20 s, and via inter-pMHCII FRET-based measurements, which as a whole did not provide any evidence for their existence. The latter experiments were performed to account in particular for pMHCIIs diffusing slowly on the cell surface. FRET-based measurements relied on FRET dye combination featuring a Förster radius of 5.1 nm (AF555 and AF647) and site-specifically labeled probes present at ratios of 1:1 to 1:4 for quantitative readout. An earlier study employing FITC and TRITC-conjugated 14.4.4 monoclonal antibodies (Förster radius: 5.5 nm) to reveal homo-association of pMHCII on B lymphoma cells arrived at an average FRET efficiency of 6.5% without further description of the donor to acceptor ratios applied and the numbers of fluorophores attached to the 14.4.4 mAb (Gombos *et al*, 2004). In contrast, our quantitative analysis, which included the use of site-specifically conjugated scF$_V$ and FRET simulations involving monomeric and randomly distributed FRET pairs, failed to provide any evidence for pMHCII homodimerization. Instead, we showed with the use of PLB-anchored pMHCIIs that random encounters of freely diffusing monomeric entities can give rise to FRET values of such magnitude.

With this information, we set out to recapitulate antigen recognition by T-cells in contact with PLBs featuring pMHCIIs as well as ICAM-1 and B7-1 at physiological densities. In preceding T-cell imaging studies involving fluorescence and calcium measurements, it had been reported that co-agonist pMHCIIs contributed in part to the response to agonist pMHCIIs (Wulfing *et al*, 2002; Krogsgaard *et al*, 2005; Anikeeva *et al*, 2012). Yet other studies featuring similar techniques questioned the role of co-agonists (Ma *et al*, 2008) or concluded that CD8 co-receptor affinities dictated the co-agonistic effect (Gascoigne, 2008; Hoerter *et al*, 2013). In this study, we found TCR engagement of all endogenous pMHCIIs with previously attributed co-agonist qualities at the level of random molecular collisions. Only for the altered peptide ligand I-E^k/K99A (and I-E^k/K99R, a proposed antagonist), we detected specific TCR binding, which amounted to fewer than 500 interactions per synapse at any given time when these pMHCIIs had been present at a density of 1,390 molecules μm^{-2}. Assuming that the T-cell synapse covers an area of 100 μm^2 with a TCR density of 100 TCRs μm^{-2}, this number indicates that on average fewer than 0.4% of available I-E^k/K99A and only 1% of all synaptic TCRs had been occupied. Not surprisingly, highly abundant I-E^k/K99A (outnumbering TCRs in our example 14:1) did not alter TCR binding of rare agonist pMHCIIs in early and mature synapses. In fact, the ensuing TCR-proximal signaling response was unaffected, even when I-E^k/K99A was co-presented on DNA origami-based platforms in a spatially highly defined fashion with the agonist ligand I-E^k/MCC. Interestingly, our observations contrast previous findings we had based on the use of DNA origami-tethered anti-TCRβ-scF$_V$s as a means of T-cell stimulation (Hellmeier *et al*, 2021a). Here, we identified distances separating individual stimulatory scF$_V$s that were smaller than 20 nm as permissive for T-cell activation, a notion that did not hold up for the recognition of nominal pMHCII antigens. A possible explanation for such divergent behavior may include ligand-dependent differences in stimulatory potency as well as the highly transient nature of TCR-pMHC engagement, which enables single antigens to trigger more than one TCR/CD3 complex in rather close proximity.

It should also be noted that instead of promoting or functionally enhancing rare agonist-TCR interactions, highly abundant bystander pMHCIIs rather competed with agonist pMHCIIs for available TCRs with increasing TCR affinities. We also observed that unlike endogenous I-E^k/ER60 and I-E^k/β2m, the MCC-based APLs I-E^k/K99A and I-E^k/K99R promoted low-level signaling when present at supraphysiological pMHCII densities (> 1,000 molecules μm^{-2}), yet without sensitizing T-cells for agonist pMHCIIs.

In summary, our results leave us with no plausible conclusion other than that single agonist pMHCII entities elicit the full

response of the scanning T-cell in a fully autonomous fashion. In view of future improved designs of T-cell-based immunotherapies, this realization places a particular emphasis on a deep subcellular and molecular understanding of effective, faithful, and fail-safe TCR-proximal signal amplification, which appears to rely solely on the distinct nature of synaptic TCR-pMHCII interactions and CD4 co-receptor engagement within the context of plasma membrane biophysics and physiology. Our findings imply furthermore that rapid redistribution of newly arriving pMHCIIs rather than clustering underlies highly efficient detection by scanning $CD4^+$ T-cells. It will be highly informative to reveal communalities and differences concerning the organization of pMHCI on the surface of target cells with possible consequences for $CD8^+$ T-cell recognition.

Materials and Methods

Reagents and Tools table

Reagent/Resource	Reference or Source	Identifier or Catalog Number
Experimental Models		
5c.c7 αβ TCR-tg B10.A (*Mus musculus*)	Björn Lillemeier (Salk Institute for Biological Studies, US & Albert-Ludwigs-Universität Freiburg, Germany), Michael Dustin (University of Oxford, UK)	N/A
CH27 B-cell lymphoma line	Mark Davis (Stanford University, USA)	N/A
X38-Ag8 plasmacytoma cell line (GM-CSF producing)	Michael Sixt, IST Austria	N/A
14.4.4S hybridoma cell line	ATCC	HB-32
Sf9 cells	Thermo Fisher Scientific	11496015
High Five cells	Thermo Fisher Scientific	B85502
Recombinant DNA		
pET21a(+) 14.4.4 scF_V	This manuscript	N/A
pET21a(+) 14.4.4 scF_V-biotin	This manuscript	N/A
pET21a(+) PS-CFP2 AVI-tag 3C 12xHis	Platzer *et al* (2020)	N/A
pET21a(+) streptavidin alive 6xHis subunit	Alice Ting (Stanford University, USA)	N/A
pET21a(+) streptavidin alive A106C 3C 6xGlu	Platzer *et al* (2020)	N/A
pET21a(+) streptavidin alive A106C 6xGlu	Platzer *et al* (2020)	N/A
pET21a(+) streptavidin alive 6xGlu	Fairhead *et al* (2014)	N/A
pET21a(+) streptavidin dead	Alice Ting (Stanford University, USA)	N/A
pET21a(+) H57 scF_V (J0 and J1)	Huppa *et al* (2010)	N/A
pET21a(+) I-E^k α 6xHis	Huppa *et al* (2010)	N/A
pET21a(+) I-E^k β 6xHis	Huppa *et al* (2010)	N/A
pET21a(+) I-E^k α 12xHis	Huppa *et al* (2010)	N/A
pET21a(+) I-E^k α - biotin	Huppa *et al* (2010)	N/A
pET21a(+) I-E^k β	Huppa *et al* (2010)	N/A
Antibodies		
I-E^k mAb (14.4.4S)	Hybridoma cell line (ATCC)	HB-32
14.4.4 mAb – AF647	This manuscript	N/A
14.4.4 scF_V (all labels, all variants)	This manuscript	N/A
I-A^k mAb (clone 11-5.2)	BioLegend	110002
11-5.2 mAb – AF647	This manuscript	N/A
CD16/CD32 mAb (clone: 93)	BioLegend	101302
CD11b-BV510 mAb (clone: M1/70)	BioLegend	101245
IgG2b mAb – BV510 (clone: RTK4530)	BioLegend	400645
CD55 mAb – APC (clone: RIKO-3)	BioLegend	131805
CD4 mAb – APC-Cy7 (clone: GK1.5)	BD Biosciences	561830

Reagents and Tools table (continued)

Reagent/Resource	Reference or Source	Identifier or Catalog Number
CD8 mAb – PE-Cy7 (clone: 53-6.7)	BD Biosciences	561097
CD4 mAb – biotin (clone: RM4-5)	BioLegend	100506
CD8 mAb – biotin (clone: 53-6.7)	BioLegend	100704
CD19 mAb – V450 (clone: 1D3)	BD Biosciences	560376
CD71 mAb – PE (Batch: 39716)	BD Biosciences	553267
CD11c mAb – FITC (clone: N418)	eBioscience	11-0114-81
TNF-α mAb – PE (clone: MP6-XT22)	BioLegend	506305
IFN-γ mAb – BV421 (clone: XMG1.2)	BD Biosciences	563376
IgG mAb – FITC (clone: eBio299Arm)	eBioscience	11-4888-81
CD44 mAb – eF450 (clone: IM7)	eBioscience	48-0441-82
H57 scF_V (J0, J1, all labels)	Huppa *et al* (2010)	N/A
CD18 mAb (clone: M18/2)	BioLegend	101402
CD205 mAb (clone: NLDC-145)	BioLegend	138202
Goat anti-Mouse IgG (H+L)-AF647	Thermo Fisher Scientific	A-21235
Oligonucleotides and other sequence-based reagents		
5′VH chain: 5′-GAGGTGCAGCTGCAGGAGTCTGG-3′	Ohradanova-Repic *et al* (2018)	N/A
5′VL chain: 5′-GACATTGTGCTGACMCARTCTCC-3′	Ohradanova-Repic *et al* (2018)	N/A
3′CH chain: 5′-AATTTTCTTGTCCACCTTGGTGCT-3′	Ohradanova-Repic *et al* (2018)	N/A
3′CL chain: 5′-ACACTCATTCCTGTTGAAGCTCTTG-3′	Ohradanova-Repic *et al* (2018)	N/A
BD Baculo Gold Linearized Baculovirus DNA	BD Biosciences	554739
X-strand: tetrazine-PEG5-CTTCTGTCTATCTTGGC	Biomers	N/A
V-strand: tetrazine-PEG5-ACATGACACTACTCCAC	Biomers	N/A
Chemicals, Enzymes and other reagents		
Murine I-E^k/(ANP) 2x6His	Huppa *et al* (2010)	N/A
Murine I-E^k/(ANP) α-biotin	Huppa *et al* (2010)	N/A
Murine ICAM-1-12xHis	Huppa *et al* (2010)	N/A
Murine B7-1-12xHis	Huppa *et al* (2010)	N/A
14.4.4 scF_V, 14.4.4 scF_V-biotin	This manuscript	N/A
AF555-H57 scF_V (J1)	Huppa *et al* (2010)	N/A
Monovalent streptavidin 6× Glu tag (mSav)	Fairhead *et al* (2014); This manuscript	N/A
Monovalent streptavidin (A106C) 6× Glu tag (mSav)	This manuscript	N/A
PS-CFP2	http://evrogen.com	N/A
PS-CFP2 with a free cysteine in the linker sequence	Platzer *et al* (2020)	N/A
6-Methyl-Tetrazine-PEG_4-Maleimide	Jena Bioscience	CLK-A139-100
TCO-PEG_3-Maleimide	Jena Bioscience	CLK-1002-10
Alexa Fluor 647 C2 Maleimide, 1 mg	Thermo Fisher Scientific	A20347
Alexa Fluor 555 carboxylic acid, succinimidyl ester, 1 mg	Thermo Fisher Scientific	A20009
Alexa Fluor 647 carboxylic acid, succinimidyl ester, 1 mg	Thermo Fisher Scientific	A20006

Reagents and Tools table (continued)

Reagent/Resource	Reference or Source	Identifier or Catalog Number
Alexa Fluor 488 C5 Maleimide 1 mg	Thermo Fisher Scientific	A10254
Alexa Fluor 555 C2 Maleimide, 1 mg	Thermo Fisher Scientific	A20346
Maleimide-Abberior STAR635P, 1 mg	Abberior	ST635P-0003-1MG
Maleimide-Abberior CAGE635, 1 mg	Abberior	CA635-0003-1MG
Tris(2-carboxyethyl)phosphine (TCEP)	Thermo Fischer Scientific	T2556
BirA biotin ligase	Avidity	N/A
HRV 3C Protease	ACRO Biosystems	3CC-N3133
Mouse IL-2 recombinant protein, eBioscience	Thermo Fisher Scientific	34-8021-82
Mouse IL-4 recombinant protein, eBioscience	Thermo Fisher Scientific	BMS338
GM-CSF	Biozym	B576304
Ni-NTA Agarose	QIAGEN	30230
MCC (88–103): ANERADLIAYLKQATK	Elim Biopharmaceuticals https://elimbio.com	N/A
MCC(GGSC): ANERADLIAYLKQATKGGSC	Intavis https://intavispeptides.com	N/A
MCC(dSdSdC): ANERADLIAYLKQATKdSdSdC	Biosyn https://www.biosyn.com	N/A
MCC(NVOC): ANERADLIAYL[NVOC]QATKGGSC	Elim Biopharmaceuticals https://elimbio.com	N/A
MCC(ANP): ANERADLIAYL[ANP]QATKGGSC	Elim Biopharmaceuticals https://elimbio.com	N/A
T102S: ANERADLIAYLKQASKGGSC	Margit Focke-Tejkl (Medical University of Vienna)	N/A
K99A: ANERADLIAYLAQATKGGSC	Intavis https://intavispeptides.com	N/A
K99R: ANERADLIAYLRQATKGGSC	Intavis https://intavispeptides.com	N/A
ER60: GFPTIYFSPANKKLGGSC	Intavis https://intavispeptides.com	N/A
β2m: HPPHIEIQMLKNGKKIPGGSC	Intavis https://intavispeptides.com	N/A
null: ANERAELIAYLTQAAKGGSC	Intavis https://intavispeptides.com	N/A
LPS *Escherichia coli* O55:B5	Merck	L2880
EZ-Link Maleimide-PEG_2-Biotin	Thermo Fisher Scientific	21901BID
EZ-Link NHS-LC-LC-Biotin	Thermo Fisher Scientific	21343
Surfact-Amps NP-40	Thermo Fisher Scientific	28324
1,2-dioleoyl-sn-glycero-3-[N(5-amino-1-carboxypentyl)iminodiacetic acid] succinyl [nickelsalt]	Avanti Polar Lipids	790404P
1-Palmitoyl-2-oleoyl-sn-glycero-3-phosphocholine	Avanti Polar Lipids	850457C
1,2-dipalmitoyl-sn-glycero-3-phosphocholine	Avanti Polar Lipids	850355P
Albumin from chicken egg white	Merck	A5253
Fura-2, AM	Thermo Fisher Scientific	F1221
16% Formaldehyde solution (PFA)	Thermo Fisher Scientific	28906
BD Perm/Wash	BD Biosciences	554723
BD Cytofix/Cytoperm	BD Biosciences	554655
BD GolgiStop	BD Biosciences	554724
BD GolgiPlug	BD Biosciences	555029

Reagents and Tools table (continued)

Reagent/Resource	Reference or Source	Identifier or Catalog Number
Deoxycholic acid	Merck	D6750
Triton X-100	Merck	X100
EDTA	Roth	8043.2
Guanidine hydrochloride	Labochem	LC-10170.1
Sodium bicarbonate	Roth	6885.1
TCEP agarose CL4-B	Merck	52486
FBS	Biowest	S181H-500
HBSS (Gibco)	Thermo Fisher Scientific	14175095
1640 RPMI (Gibco)	Thermo Fisher Scientific	31870074
IMDM (Gibco)	Thermo Fisher Scientific	21980032
β-mercaptoethanol (Gibco)	Thermo Fisher Scientific	31350010
L-Glutamine (Gibco)	Thermo Fisher Scientific	A2916801
Penicillin-Streptomycin (Gibco)	Thermo Fisher Scientific	15140148
MEM Non-essential amino acids	Thermo Fisher Scientific	11140050
Sodium Pyruvate (Gibco)	Thermo Fisher Scientific	11360070
Histopaque-1119	Merck	11191
Gentamicin	Merck	G1397
Software		
Matlab version R2017-2021a	https://de.mathworks.com	N/A
GraphPad Prism 10	https://www.graphpad.com	N/A
ImageJ (Fiji)	www.fiji.sc	N/A
Metamorph Research Imaging version 7.10.	https://www.moleculardevices.com	N/A
µManager	https://micro-manager.org	N/A
FlowJo software version 10.4.2	www.flowjo.com	N/A
R 4.2.3 GUI 1.79 High Sierra build (8198)	https://www.r-project.org	N/A
Leica Suite	https://www.leica-microsystems.com	N/A
Other		
Mono Q 5/50 GL	Cytiva	17-5166-01
Superdex 75 10/300 GL	Cytiva	17-5174-01
Superdex 200 10/300 GL	Cytiva	17-5175-01
Amicon Ultra-15 centrifugal filters 10 kDa	Merck	UFC901024
Amicon Ultra-4 centrifugal filters 10 kDa	Merck	UFC801024
Amicon Ultra-2 centrifugal filters 100 kDa	Merck	UFC210024
Pursuit XRs C18 250 ×21.2 mm, 5 µm HPLC column	Agilent	A3000250 x212
Stirred ultrafiltration cell 400 ml	Merck	UFSC40001
Ultrafiltration Discs 10 kDa	Merck	PLGC07610
OneComp eBeads	Thermo Fisher Scientific	01-1111-42
Quantum Alexa Fluor 647 MESF	Bangs Laboratories	647
TetraSpec Microspheres, 0.1 µm	Thermo Fisher Scientific	T7279
HCX PL APO 100×, NA = 1.47	Leica	N/A
Nikon SR APO TIRF 100×, NA = 1.49	Nikon	N/A
HCX PL Fluotar 20×, NA = 0.5	Leica	N/A
Nikon S Fluor, 20×, NA = 0.75	Nikon	N/A
UPlanFL N 10×, NA = 0.3	Olympus	N/A

Reagents and Tools table (continued)

Reagent/Resource	Reference or Source	Identifier or Catalog Number
EMCCD camera iXon Ultra 897	Andor https://andor.oxinst.com	N/A
CMOS prime95B	Teledyne Photometrics https://www.photometrics.com	N/A
B-cell Isolation Kit mouse	Miltenyi Biotec	130-090-862
TRIzol Reagent	Thermo Fisher Scientific	15596026
QuikChange II mutagenesis kit	Agilent	200523
Escherichia coli BL-21 (DE3)	Agilent	200131
Pierce Protein A/G Agarose	Thermo Fisher Scientific	20422
Pierce Monomeric Avidin Agarose	Thermo Fisher Scientific	20219
Pierce Glutathione Agarose	Thermo Fisher Scientific	16100
Picodent eco-sil extrahart	Picodent	1300 9100
Nunc LabTek chambers, 16 wells	Thermo Fisher Scientific	178599PK
Nunc LabTek chambers, 8 wells	Thermo Fisher Scientific	177445PK
L6Cc laser combiner box	Oxxius	N/A
Plasma cleaner	Diener ZEPTO	N/A
0.2 µm Filtropur S filter	SARSTEDT	83.1826.001
0.45 µm Filtropur S filter	SARSTEDT	83.1826
Abberior Mount Solid	Abberior	MM-2011-2X15ML

Methods and Protocols

Animal model and ethical compliance statement

5c.c7 αβ TCR-transgenic mice bred onto the B10.A background were a kind gift from Björn Lillemeier (Salk Institute for Biological Studies, US & Albert-Ludwigs-Universität Freiburg, Germany) and Michael Dustin (University of Oxford, UK). Mouse breeding and euthanasia were evaluated by the ethics committees of the Medical University of Vienna and approved by the Federal Ministry of Science, Research and Economy, BMWFW (BMWFW-66.009/0378-WF/V/3b/2016). All procedures to isolate lymphocytes, splenocytes, and bone marrow from 8- to 12-week-old gender-mixed mice were performed in accordance with Austrian law (Federal Ministry for Science and Research, Vienna, Austria), the guidelines of the Federation of Laboratory Animal Science Associations (FELASA), which match those of Animal Research Reporting *In Vivo* Experiments (ARRIVE), and the guidelines of the ethics committees of the Medical University of Vienna. Mice were kept and bred in the animal facility of the Medical University of Vienna.

Tissue culture

Splenocytes or lymphocytes of 5c.c7 αβ TCR-transgenic mice were isolated and pulsed with 0.5 µM C18 reverse-phase HPLC-purified MCC (88–103) peptide (sequence: ANERADLIAYLKQATK, underlined amino acids represent the T-cell epitope; Elim Biopharmaceuticals) and 50 U ml^{-1} IL-2 (eBioscience) for 7 days to arrive at a transgenic T-cell culture (Huppa *et al*, 2003). T-cells were maintained at 37°C in an atmosphere of 5% CO_2 in 1640 RPMI media (Gibco) supplemented with 100 U ml^{-1} penicillin, 100 µg ml^{-1} streptomycin (Gibco), 2 mM L-glutamine (Gibco), 10% FBS (Biowest), 0.1 mM MEM non-essential amino acids (Gibco), 1 mM sodium pyruvate (Gibco), and 50 µM β-mercaptoethanol (Gibco). After expansion, T-cells were subjected to Histopaque-1119 (Merck) density gradient centrifugation to remove dead cells. Antigen-experienced T-cells were used for experiments from day 8 to 10.

B-cells were isolated from lymph nodes of 5c.c7 αβ TCR-transgenic mice and enriched using a murine B-cell isolation kit in order to deplete activated B-cells and non-B-cells (B-cell Isolation Kit mouse, Miltenyi Biotec). B-cells were cultured at 37°C and 5% CO_2 in 1640 RPMI (Gibco) supplemented with 10% FBS (Biowest), 100 U ml^{-1} penicillin, 100 µg ml^{-1} streptomycin (Gibco), 2 mM L-glutamine (Gibco) and 50 µM β-mercaptoethanol (Gibco). B-cells were either used for experiments directly after isolation and enrichment as naive (non-activated) B-cells or activated with 50 µg ml^{-1} LPS derived from *E. coli* serotype O55:B5 (Merck) for 24–48 h to induce B-cell blast formation.

BMDCs were isolated from 5c.c7 αβ TCR-transgenic mice and differentiated for 7 days as described (Inaba *et al*, 2009). BMDCs were maintained at 37°C and 5% CO_2 in IMDM (Gibco) supplemented with 10% FBS (Biowest), 100 U ml^{-1} penicillin, 100 µg ml^{-1} streptomycin (Gibco), 2 mM L-glutamine (Gibco), 50 µM β-mercaptoethanol (Gibco), 20 ng ml^{-1} GM-CSF (Biozym), or X38-Ag8 supernatant (1%) and from day 5 on additionally with 10 ng ml^{-1} IL-4 (eBioscience). At day 7, BMDCs were either activated with 100 ng ml^{-1} LPS from *E. coli* serotype O55:B5 (Merck) for 24–48 h to arrive at a mature BMDC culture or alternatively frozen to −80°C in 90% FBS (Biowest) and 10% DMSO (Merck) using a cell freezing container (CoolCell LX, Biozym) and stored in liquid N_2 for later experiments.

The murine CH27 B-cell lymphoma cell line was cultured at 37°C and 5% CO_2 in 1640 RPMI (Gibco) supplemented with 10% FBS (Biowest), 100 U ml^{-1} penicillin (Gibco), 100 µg ml^{-1} streptomycin (Gibco), 2 mM L-glutamine (Gibco), and 50 µM β-mercaptoethanol (Gibco).

The 14.4.4 mAb-producing hybridoma cell line (isotype: mouse IgG2a, kappa) was maintained at 37°C and 5% CO_2 in 1640 RPMI (Gibco) supplemented with 5% FBS (Biowest), 100 U ml^{-1} penicillin (Gibco), 100 µg ml^{-1} streptomycin (Gibco), and 2 mM L-glutamine (Gibco).

The plasmacytoma cell line X38-Ag8 producing GM-CSF was cultivated at 37°C and 5% CO_2 in IMDM (Gibco) supplemented with 5% FBS (Biowest), 100 U ml^{-1} penicillin, 100 µg ml^{-1} streptomycin (Gibco), 2 mM L-glutamine (Gibco), 50 µM β-mercaptoethanol (Gibco), and 50 µg ml^{-1} gentamicin (Merck). The supernatant containing GM-CSF was filtered through a 0.45 µm Filtropur S filter (SARSTEDT) and stored at −80°C.

All cell lines were tested for mycoplasma contamination on a biweekly basis using Hoechst staining of supernatant-treated Vero cells as an indicator.

Protein expression, refolding, and preparation of imaging tools

In order to genetically assemble the 14.4.4 scF_V, we obtained the sequence information of the 14.4.4 mAb VH and VL chain by isolating total mRNA from a 14.4.4 mAb-producing hybridoma cell line with the use of TRIzol (Thermo Fisher Scientific) followed by reversely transcribing the isolated mRNA into cDNA (First-strand cDNA Kit, Roche).

The 5′ primers for the VH chain (5′-GAGGTGCAGCTGCAGGAGT CTGG-3′) and kappa VL chain (5′-GACATTGTGCTGACMCARTCTCC-3′) as well as the 3′ primers for the CH (5′-AATTTTCTTGTCCACCTT GGTGCT-3′) and kappa CL chain (5′-ACACTCATTCCTGTTGAAGCT CTTG-3′) were kindly provided by Anna Ohradanova-Repic (Medical University of Vienna) (Ohradanova-Repic *et al*, 2018).

We genetically combined the C-terminus of the VH domain and the N-terminus of the VL domain with a $[GGGGS]_3$ linker to obtain a functional scF_V transcript, which was cloned into the pet21a(+) expression vector using the restriction enzymes NdeI and HindIII (Appendix Fig S20A and B). To create a target for site-specific modifications using maleimide-based click chemistry, we substituted in the VH domain the serine at position 120 to an unpaired cysteine (14.4.4 scF_V) via site-directed mutagenesis (QuikChange II, Agilent). In addition, we extended the 14.4.4 scF_V C-terminally with the BirA biotin ligase (Avidity) recognition site (GLNDIFEAQKIEWHE) to allow for a site-specific attachment of biotin and fluorophores (e.g., 14.4.4 scF_V-AF647-biotin).

The TCR β-reactive H57 scF_V (J0, GenBank: MH045460.1) and the H57 scF_V, having a free cysteine for site-specific labeling (J1, GenBank: MH045461.1), were produced as described (Huppa *et al*, 2010; Brameshuber *et al*, 2018).

All scF_V constructs were expressed as inclusion bodies in *E. coli* (BL-21) for 4 h at 37°C. Bacterial cells processed via ultrasound and insoluble inclusion bodies were extracted with 1% deoxycholic acid (Merck) and 1% Triton X-100 (Merck) in 50 mM Tris pH 8.0, 200 mM NaCl, and 2 mM EDTA (Roth), and finally, dissolved in 6 M guanidine hydrochloride (Merck). 14.4.4 and H57 scF_Vs were refolded from inclusion bodies *in vitro*, concentrated using an ultrafiltration cell (10 kDa cutoff, Merck) and purified by gel filtration using Superdex 200 (Superdex 200, 10/300 GL, Cytiva) as described (Tsumoto *et al*, 1998). scF_V containing a free cysteine was concentrated in the presence of 50 µM Tris (2-carboxyethyl) phosphine (TCEP, Thermo Fisher Scientific).

After S200 gel filtration, fractions containing monomeric scF_V were concentrated with Amicon Ultra-4 centrifugal filters (10 kDa cut off, Merck). 14.4.4 scF_V without an unpaired cysteine was randomly conjugated on surface-exposed lysine residues with Alexa Fluor 555 carboxylic acid, succinimidyl ester (Thermo Fisher Scientific), or Alexa Fluor 647 carboxylic acid, and succinimidyl ester (Thermo Fisher Scientific). 14.4.4 scF_V harboring an unpaired cysteine residue were site-specifically conjugated with Alexa Fluor 647 C2 Maleimide, Alexa Fluor 568 C5 Maleimide, Alexa Fluor 555 C2 Maleimide, Alexa Fluor 488 C5 Maleimide (Thermo Fisher Scientific), or Maleimide-Abberior STAR 635P (Abberior) according to the manufacturer's instructions and in the presence of 50 µM TCEP (Thermo Fisher Scientific). The monomeric H57 scF_V (J1) was conjugated with Alexa Fluor 555 C2 Maleimide or Alexa Fluor 488 C5 Maleimide according to the same protocol.

To remove excess dye, labeled 14.4.4 scF_Vs were purified by gel filtration using Superdex 75 (Superdex 75, 10/300 GL, Cytiva). Fractions containing monomeric and labeled 14.4.4 scF_Vs were concentrated with Amicon Ultra-4 centrifugal filters (10 kDa cut off, Merck) to arrive at a protein concentration between 0.2 and 1 mg ml^{-1}. Protein-to-dye ratios were determined by spectrophotometry at 280 nm and the corresponding absorption maximum of the dyes (647, 635, 568, 555, and 488 nm). Protein-to-dye ratios of randomly conjugated 14.4.4 scF_Vs were between 1 and 2. Protein-to-dye ratios of site-specifically decorated 14.4.4 scF_V and 14.4.4 scF_V-biotin were as follows: 0.98 (14.4.4 scF_V-AF488 and 14.4.4 scF_V-AF555) and 1.0 (14.4.4 scF_V-AF647, 14.4.4 scF_V-AF647-biotin, 14.4.4 scF_V-AF488-biotin, 14.4.4 scF_V-AF555-biotin, H57 scF_V-AF555, and H57 scF_V-AF488). The 14.4.4 scF_V-abSTAR635P exhibited a protein-to-dye ratio of 0.75. Proteins were stored in 1× PBS supplemented with 50% glycerol at −20 to −80°C.

The I-E^k-specific 14.4.4 mAb was purified from hybridoma supernatant using a protein A/G agarose column (Thermo Fisher Scientific) and gel filtration (Superdex-200 10/300 GL, Cytiva). The 14.4.4 mAb and the I-A^k-reactive 11–5.2 mAb were randomly labeled via available lysine residues with Alexa Fluor 647 carboxylic acid succinimidyl ester (Thermo Fisher Scientific) according to the manufacturer's instructions and purified via gel filtration (Superdex-200 10/300 GL, Cytiva). Protein-to-dye ratio of the 14.4.4 mAb and 11–5.2 mAb were 2.1 and 2.4, respectively.

The CD205-reactive mAb NLDC-145 (BioLegend) and the CD18-reactive mAb M18/2 (BioLegend) were randomly conjugated with Alexa Fluor 647 carboxylic acid succinimidyl ester (Thermo Fisher Scientific) and EZ-Link NHS-LC–LC-Biotin (Thermo Fisher Scientific) in a 1-to-2 molar ratio (protein:dye and protein:biotin) in the presence of 0.1 M sodium bicarbonate (Roth) for 1 h followed by gel filtration (Superdex-200 10/300 GL, Cytiva). The CD18-reactive mAb M18/2 was additionally purified with monomeric avidin agarose (Thermo Fisher Scientific) to remove non-biotinylated mAb. The protein-to-dye ratio of the NLDC-145 mAb and M18/2 mAb was 2.1 and 1.3, respectively. The degree of mAb NLDC-145 or mAb M18/2 biotinylation was verified by a monovalent streptavidin-based gel shift assays and SDS–PAGE analysis (Appendix Fig S7D).

mSav was prepared with some modifications as described (Howarth *et al*, 2006; Fairhead *et al*, 2014). The pET21a(+) expression vectors encoding either for the "dead" (i.e., biotin non-binding) or the "alive" (i.e., biotin binding) streptavidin subunit were a kind gift from Alice Ting (Stanford University, USA). We substituted the hexa-histidine tag on the "alive" subunit with a cleavable hexa-glutamate tag to allow for purification via anion exchange

chromatography (Mono Q 5/50 GL, Cytiva) followed by a recognition site of the 3C protease for optimal removal of the tag (Platzer *et al*, 2020). To produce mSav for conjugation with maleimide-linked fluorescent dyes or maleimide-tetrazine (or −TCO) for orthogonal click chemistry-based protein conjugation, we mutated the alanine residue at position 106 (A106C) for a cysteine residue in the "alive" subunit. The mSav platform mSav-STAR635 was prepared as described (Platzer *et al*, 2020).

Both, dead and alive streptavidin subunits were expressed in *E. coli* (BL-21) for 4 h at 37°C and refolded from inclusion bodies as described (Howarth *et al*, 2006; Fairhead *et al*, 2014; Platzer *et al*, 2020). After refolding *in vitro* (Howarth & Ting, 2008), the streptavidin tetramer mixture (containing D4, A1D3, A2D2, A3D1, and A4) was concentrated in an ultrafiltration cell (10 kDa cut off, Merck); mSav (A106C) was refolded and concentrated in the presence of 100 μM TCEP. After buffer exchange to 20 mM Tris–HCl, pH 8.0, with Amicon Ultra-15 centrifugal filters (10 kDa cut off, Merck), the mixture of tetramers was purified by anion exchange chromatography (Mono Q 5/50 GL, Cytiva) using a column gradient from 0.1 to 0.4 M NaCl over 90 ml. mSav and mSav (A106C) were eluted with 0.22 M NaCl, concentrated again (Amicon Ultra-4 centrifugal filters, 10 kDa cut off), and further purified via gel filtration (Superdex 200 10/300, Cytiva). mSav was either stored at −80°C in 1× PBS or randomly labeled with fluorescent dyes (e.g., Alexa Fluor 555 carboxylic acid, succinimidyl ester) according to the manufacturer's instructions. mSav featuring an unpaired cysteine was site-specifically labeled with Maleimide-Abberior STAR 635P (Abberior), Maleimide-Abberior CAGE 635 (Abberior), or Alexa Fluor 647 C2 Maleimide (Thermo Fisher Scientific) according to the manufacturer's instructions. In the last step, dye-conjugated mSav was purified by gel filtration using Superdex 75 (Superdex 75, 10/300 GL, Cytiva), and monomeric fractions were concentrated with Amicon Ultra-4 centrifugal filters (10 kDa cut off, Merck) and stored in 1× PBS supplemented with 50% glycerol at −20 to −80°C.

DNA-conjugated mSav (X-strand—CTTCTGTCTATCTTGGC, or V-strand—ACATGACACTACTCCAC) were produced as described (Hellmeier *et al*, 2021b).

Removal of the hexa-glutamate tag was carried out via 3C protease-based cleavage (ACRO Biosystems) for 24 h at 4°C followed by subtraction of the GST-tagged 3C protease via glutathione agarose (Thermo Fisher Scientific) and gel filtration (Superdex 200, 10/300 GL, Cytiva). Protein-to-dye ratios of the randomly dye-conjugated mSav was 1.5 (mSav-AF555) for the site-specifically decorated mSav 1.0 (mSav-AF647). Proteins were stored at −20°C in 1× PBS supplemented with 50% glycerol.

Divalent streptavidin (diSav) in *trans* configuration (optionally with a 3C cleavage site) was prepared as described (Fairhead *et al*, 2014). In brief, *trans* diSav was eluted from the Mono Q 5/50 GL with ~0.25 M NaCl, purified via gel filtration (Superdex 200 10/300 GL, Cytiva), concentrated with Amicon Ultra-4 centrifugal filters (10 kDa cut-off), and stored in 1× PBS supplemented with 50% glycerol at −20°C.

Monomeric photo-switchable cyan fluorescence protein 2 (PS-CFP2, Evrogen) featuring an unpaired cysteine residue and C-terminally extended with an AVI-tag (GLNDIFEAQKIEWHE) for site-specific biotinylation with the BirA biotin ligase (Avidity) preceded by a 3C protease recognition site (LEVLFQGP) and a 12x histidine (12x His) tag was produced as described (Platzer *et al*, 2020). To produce a conjugate of mSav and PS-CFP2, we site-specifically decorated PS-CFP2 with 6-Methyl-Tetrazine-PEG_4-Maleimide (Jena Bioscience) and mSav (A106C) with TCO-PEG_3-Maleimide (Jena Bioscience) according to the manufacturer's instructions. PS-CFP2-tetrazine and mSav-TCO were purified from unreacted crosslinker via gel filtration (Superdex 75 10/300 GL; Cytiva) and concentrated with Amicon Ultra-4 centrifugal filters (10 kDa cut off) to ~1 mg ml^{-1}. To click PS-CFP2-tetrazine to mSav-TCO, we incubated both proteins for 1 day at 4°C in 1× PBS and purified the resulting mSav-cc-PS-CFP2 together with an excess of PS-CFP2-tetrazine via Ni-NTA agarose-based affinity chromatography (QIAGEN) and gel filtration (Superdex 200 10/300 GL, Cytiva). Adduct fractions containing mSav-cc-PS-CFP2 were verified by SDS–PAGE, concentrated with Amicon Ultra-4 centrifugal filters (10 kDa cut-off, Merck), and stored at −20°C in 1× PBS supplemented with 50% glycerol.

For blinking analysis of PS-CFP2, we conjugated the mSav-STAR635 platform with PS-CFP2-biotin, as described in Platzer *et al* (2020).

The murine MHC class II molecule I-E^k α subunits (C-terminally extended with a BirA-biotin ligase recognition site, 6× histidine-tag or 12× histidine-tag) and the β subunits (no tag or C-terminally extended with a 6× histidine-tag) were expressed in *E. coli* as inclusion bodies and refolded *in vitro* with a cleavable placeholder peptide (ANERADLIAYL[ANP]QATK) as described (Xie *et al*, 2012; Hellmeier *et al*, 2023). Specifically, we refolded I-E^k/ANP 2x6His (or α-12His) for attachment to 18:1 DGS-NTA(Ni) and I-E^k/ANP α-biotin for attachment to monovalent or divalent streptavidin. After refolding, we purified I-E^k/ANP 2x6His via Ni-NTA-based affinity chromatography followed by gel filtration (Superdex 200 10/300 GL, Cytiva). After refolding I-E^k/ANP α-biotin, we purified the protein via affinity chromatography using a custom-made 14.4.4 mAb column (Gohring *et al*, 2021) followed by gel filtration (Superdex 200 10/300 GL, Cytiva). I-E^k/ANP α-biotin was site-specifically biotinylated using the BirA biotin ligase (Avidity) and purified via Ni-NTA agarose (to remove BirA) and gel filtration (Superdex 200 10/300 GL, Cytiva). Monomeric protein fractions were concentrated to ~1 mg ml^{-1} (Amicon Ultra-4 centrifugal filters, 10 kDa cutoff), snap-frozen in liquid nitrogen, and stored at −80°C for later use and exchange of the placeholder peptide.

The placeholder peptide can be substituted with any peptide that binds into the peptide-binding cleft of I-E^k under acidic conditions (pH adjusted to 5.1 with 0.2 M citric acid buffer) over a period of 3 days (Xie *et al*, 2012).

We employed peptides C-terminally extended with a GGSC linker to render these peptides fit for maleimide-based conjugation to fluorophores. The following peptides were used to exchange the placeholder peptide:

MCC (ANERADLIAYLKQATKGGSC, T-cell epitope is underlined), T102S (ANERADLIAYLKQASKGGSC), K99A (ANERADLIAYLAQATKGGSC), K99R (ANERADLIAYLRQATKGGSC), ER60 (GFPTIYFSPANKKLGGSC), β2m (HPPHIEIQMLKNGKKIPGGSC), and null (ANERAELIAYLTQAAKGGSC).

The same loading strategy was used to produce I-E^k/MCC [NVOC], which contains a UV-cleavable 6-nitroveratryloxycarbonyl (NVOC) attached to the lysine residue in the central position of the MCC peptide (ANERADLIAYLK[NVOC]QATKGGSC) facing the TCR (DeMond *et al*, 2006).

All peptides were ordered as lyophilized products, purified via reversed-phase chromatography (Pursuit XRs C18 column, Agilent),

and verified via MALDI-TOF (Bruker) mass spectrometry. For site-specific labeling, peptides were dissolved at a concentration of 1 to 5 mg ml^{-1} in 1× PBS and incubated with TCEP agarose CL4-B (Merck) for 1 h to reduce paired cysteines. The peptide sample was filtered through a 0.22 μm filter to remove TCEP agarose and incubated with a 1.2-fold excess of maleimide-conjugated dye (Alexa Fluor 647 C2 Maleimide, Alexa Fluor 488 C5 Maleimide, or Alexa Fluor 555 C2 Maleimide) for 2 h in 1× PBS supplemented with 10 mM HEPES, pH 6.8.

In addition, we produced an MCC peptide derivative (ANERADLIAYLKQATKdSdSdC, d refers to D enantiomer; underlined amino acids are recognized by the T-cell) conjugated with EZ-Link Maleimide-PEG_2-Biotin (Thermo Fisher Scientific) according to the manufacturer's instructions.

Fluorophore-conjugated (or biotinylated) peptides were purified via reversed-phase chromatography on a C18 column (Pursuit XRs C18 column, Agilent) to separate peptide–dye conjugates from unconjugated peptides or dyes. Efficient fluorophore (or biotin) coupling was again verified via MALDI-TOF (Bruker) and nanoHPLC-nanoESI-Linear-Trap-Quadrupole-Orbitrap mass spectrometry (UltiMate, RSLCnano, LTQ Orbitrap Velos, Dionex/Thermo Fisher Scientific). Stoichiometric I-E^k/MCC[ANP] peptide replacement was gauged via spectrophotometry (280 to 488 or 555 or 640 nm ratio), which was in all cases 90 to 100%.

ICAM-1-12xHis and B7-1-12xHis were expressed in a baculovirus system in *Drosophila* S2 cells and purified as described (Huppa *et al*, 2010).

Antibodies

The I-E^k-reactive 14.4.4 mAb and 14.4.4 scF_V, and the TCR β-reactive H57 scF_V were designed and produced as described above. Antibodies binding to CD4 (APC-Cy7, clone GK1.5), CD8 (PE-Cy7, clone 53–6.7), CD19 (V450, clone: 1D3), CD71 (PE), and IFN-γ (BV421, clone: XMG1.2) were purchased from BD Biosciences. Antibodies reactive to CD11c (FITC, clone: N418), Armenian hamster IgG (isotype control-FITC, clone: eBio299Arm), and CD44 (eFluor450, clone: IM7) were purchased from eBioscience. Antibodies reactive to I-A^k (clone: 11-5.2), CD16/CD32 (clone: 93), CD11b (BV510, clone: M1/70), rat IgG2b (isotype control-BV510, clone: RTK4530), CD55 (APC, clone RIKO-3), CD4 (biotin, clone: RM4-5), CD8 (biotin, clone: 53-6.7), CD205 (clone: NLDC-145), CD18 (clone M18/2), and TNF-α (PE, clone: MP6-XT22) were purchased from BioLegend. The secondary antibody reactive to mouse IgG (anti-Mouse IgG (H + L)-AF647) was purchased from Thermo Fisher Scientific.

Flow cytometry experiments

For cell surface labeling in general, 0.25×10^6 to 1×10^6 cells were stained with fluorescently labeled mAbs or scF_Vs for 20 to 30 min on ice and washed two to three times in FACS buffer (1× PBS, 1% BSA, and 0.02% NaN_3). Prior to addition of mAbs, cells were treated with the Fc block CD16/CD32 (20 μg ml^{-1}) for 15 min. Lymphocytes or splenocytes were stained with CD19 mAb-V450 (1:200), H57 scF_V-AF488 (10 μg ml^{-1}), and modified 14.4.4 scF_Vs (10–20 μg ml^{-1}). BMDCs were stained with CD11c mAb-FITC (1:200), CD11b mAb-BV510 (1:200), Armenian hamster IgG isotype control mAb-FITC (1:200), rat IgG2b isotype control mAb-BV510 (1:200), and fluorophore-conjugated 14.4.4 scF_Vs (10 μg ml^{-1}). CH27 B-cells were stained with fluorophore-conjugated 14.4.4 scF_Vs (titration up to 20 μg ml^{-1}). To determine total I-E^k expression levels (14.4.4 scF_V-AF647 staining under saturating conditions), fluorescence associated with AF647 antibody-labeled cells was compared to that of AF647 quantification beads (Quantum Alexa Fluor 647 MESF, Bangs Laboratories) serving as reference and measured as a separate sample during the same experiment with the same flow cytometer settings.

For I-E^k recovery experiments, B-cells and BMDCs were pulsed with 25 and 50 μM, respectively, MCC-PEG_2-biotin for up to 36 h, washed, and stained with saturating amounts of mSav-AF647 (10 μg ml^{-1}) or 14.4.4 scF_V-AF647 (10 μg ml^{-1}).

For intracellular cell-staining, we first labeled cell surface proteins (e.g., TCR) in FACS buffer for 30 min before washing with 1× PBS and fixation with BD Cytofix/Cytoperm (BD Biosciences) for 15 min. Samples were then washed again with BD Perm/Wash (BD Biosciences) and subsequently stained for intracellular proteins (e.g., mAbs binding to TNF-α or IFN-γ, both 1:200) in the presence of BD Perm/Wash for 30 min. After another washing step with BD Perm/Wash and FACS buffer, samples were directly subjected to flow cytometric analysis.

Samples were analyzed on the LSR II flow cytometer (BD Biosciences) or the Cytek Aurora (Cytek Biosciences). Data derived from flow cytometry measurements were analyzed with the FlowJo v10 software (BD Biosciences).

Lysis gradient centrifugation

Association of surface-labeled molecules with DRMs has been determined via lysis gradient centrifugation followed by flow cytometry as described (Schatzlmaier *et al*, 2015). In detail, 0.2 to 0.5×10^6 primary B-cells and BMDCs were treated with the Fc block CD16/CD32 (20 μg ml^{-1}) in 1640 RPMI (Gibco) supplemented with 10% FBS (Biowest) on ice for 15 min prior to staining with labeled mAbs in a total volume of 50–100 μl. Enriched non-activated and activated B-cells were stained with saturating amounts of CD71 mAb-PE (1:200), CD44 mAb-eF450 (1:200), CD55 mAb-APC (1:200), 14.4.4 mAb-AF647, 11-5.2 mAb-AF647, and 14.4.4 scF_V-AF647 (10 μg ml^{-1}). BMDCs were stained with CD11c mAb-FITC (1:100) and sorted for $CD11c^+$ cells using a SH800S cell sorter (Sony). $CD11c^+$ ($FITC^+$) cells were further stained with CD71 mAb-PE (1:200), CD44 mAb-F450 (1:200), 14.4.4 mAb-AF647, 11–5.2 mAb-AF647, and 14.4.4 scF_V-AF647 (10 μg ml^{-1}). After staining, cells were washed two times in FACS buffer (1× PBS, 1% BSA, and 0.02% NaN_3), and one-quarter of the labeled cell samples were kept on ice for intact cell recordings, while three-quarters of cells (at least 1×10^5 cells) were subjected to 0.5% NP-40 lysis gradient centrifugation (LGC) to isolate DRM-associated nuclei.

Fluorescence intensities of intact cells and DRM-coated LGC-derived nuclei were analyzed with an LSR II flow cytometer (BD Biosciences). Appropriate single-color staining of cells and OneComp eBeads (Thermo Fisher Scientific) were performed to compensate for spectral overlap. Unstained cells and unstained isolated nuclei were used to evaluate background fluorescence. The FlowJo v10 software (BD Biosciences) was employed to determine mean fluorescence intensities (MFIs) from cellular and nuclear single-event populations per sample. DRM association for mAb-stained cell surface molecules was calculated in percent as $[(MFI_{nuclei} - MFI_{nuclear\ background})/(MFI_{intact\ cells} - MFI_{cellular\ background})] \times 100$.

BMDC and T-cell co-culture assays

Activated BMDCs were pulsed with 0.008 to 1.0 μM MCC (88–103) peptide in the presence of 100 ng ml^{-1} LPS for 1 h followed by an epitope blocking step with 0 or 20 μg ml^{-1} 14.4.4 scF_V on ice for 30 min. BMDCs were then washed once in T-cell medium (see above) and transferred to a 96-well plate together with 5c.c7 TCR transgenic T-cells at a 1:1 ratio (60,000 cells in total) in the presence or absence of 20 μg ml^{-1} 14.4.4 scF_V (total volume 100 μl). The co-culture was maintained in T-cell medium supplemented with BD GolgiStop (1 μl ml^{-1}) and BD GolgiPlug (0.7 μl ml^{-1}) at 37°C in an atmosphere of 5% CO_2 for 4 h prior to intracellular staining and flow cytometric analysis.

SDS–PAGE and silver staining

Protein samples were mixed 3:1 with a 4× loading buffer (250 mM Tris–HCl, 8% SDS, 40% glycerol, and 0.04% bromophenol blue, pH 6.8) optionally supplemented with 20 mM dithiothreitol (Merck) to arrive at non-reducing and reducing conditions, respectively, and then subjected to 10–12% SDS–PAGE in running buffer (25 mM Tris–HCl, 192 mM glycine, and 0.1% SDS, pH 8.2). Silver staining and colloidal Coomassie G-250 staining were carried out for visualization of the protein bands as described (Chevallet *et al*, 2006; Dyballa & Metzger, 2009).

Preparation of functionalized glass-supported lipid bilayers (PLBs)

1,2-dioleoyl-sn-glycero-3-[N(5-amino-1-carboxypentyl)iminodiacetic acid] succinyl [nickelsalt] (Ni-DOGS-NTA, Avanti Polar Lipids) and 1-palmitoyl-2-oleoyl-sn-glycero-3-phosphocholine (POPC, Avanti Polar Lipids) were premixed at a 1:9 molar ratio or a 2:98 molar ratio in chloroform (Merck) to arrive at PLBs harboring Ni-DOGS-NTA at 10 or 2%, vacuum-dried overnight in a desiccator, re-suspended in 10 ml of degassed 1× PBS, and sonicated under nitrogen in a water bath sonicator (Q700, Qsonica). To produce immobile PLBs, we used 1% Ni-DOGS-NTA and 99% 1,2-dipalmitoyl-sn-glycero-3-phosphocholine (DPPC, Avanti Polar Lipids) instead of POPC. Vesicles were subjected to high-speed centrifugation for 4 h at 55,000 *g* (25°C) and subsequently at 8 h at 75,000 *g* (4°C) with an ultracentrifuge (Sorvall RC M150GX, Thermo Fisher Scientific) using a fixed-angle rotor (S150AT-0128, Thermo Fisher Scientific) to pellet large and non-unilamellar lipid vesicles. Glass slides (24 mm x 50 mm #1 borosilicate, VWR) were either immersed in a 1:1 mixture of 30% hydrogen peroxide (Merck) and concentrated sulfuric acid (Merck) for at least 30 min, rinsed with deionized water and air-dried or the surface was treated with a plasma cleaner (Diener ZEPTO) using plasma created from air for 10 min, and finally, glued with picodent eco-sil extrahart (Picodent) to the bottom of 8- or 16-well Nunc LabTek chambers (Thermo Fisher Scientific), from which the original glass bottom had been removed. Slides were exposed to a tenfold-diluted lipid vesicle suspension (in 1× PBS) for 15 min at room temperature (for mobile PLBs) or 60°C (for immobile PLBs) and rinsed with 15–30 ml 1× PBS at room temperature. Subsequently, His-tagged proteins were incubated for 60–90 min at room temperature and in the dark. After incubation, functionalized PLBs were rinsed twice with 15–30 ml 1× PBS to remove unbound proteins. Shortly before adding the cells to the imaging chamber, 1× PBS was exchanged for imaging buffer containing 1× HBSS (Gibco) supplemented with either 0.4 mg ml^{-1} ovalbumin (Merck) or 1% FBS (Biowest) and 2 mM $CaCl_2$ and 2 mM $MgCl_2$ (Merck).

To prepare ICAM-1-coated glass slides, 10 μg ml^{-1} murine ICAM-1-His_{12} was diluted in 1× PBS and applied to clean chambers for 2 h at 37°C. ICAM-1-coated glass slides were washed once with 10 ml 1× PBS, which was exchanged for imaging buffer consisting of 1× HBSS (Gibco) supplemented with 1% FBS (Biowest) and 2 mM $CaCl_2$ and 2 mM $MgCl_2$ (Merck) prior to adding the cells.

Preparation of DNA origami

DNA origami structures were assembled in a single folding reaction followed by purification and step-wise functionalization as previously described (Hellmeier *et al*, 2021a). At sites chosen for ligand attachment, staple strands were elongated at their 3′-end with 21 bases. At sites chosen for cholesterol anchor attachment, staple strands were elongated at their 3′-end with 25 bases. DNA origami was stored for up to 2 weeks at −20°C. DNA origami decorated with a single pMHCII species was functionalized as described (Hellmeier *et al*, 2021a). Hetero-dimeric configurations on DNA origami were created by pre-incubating biotinylated pMHCIIs with a 3× molar excess of DNA-conjugated mSav (mSav X-strand with I-E^k/K99A-AF647-biotin, and mSav V-strand with I-E^k/MCC-AF555-biotin) for 30 min at 24°C. Unbound proteins were removed by spin column purification (Amicon Ultra-2 centrifugal filters, 100 kDa cut-off (Merck)). As a last step, DNA-conjugated mSav-bound biotinylated pMHCIIs (I-E^k/K99A-AF647, I-E^k/MCC-AF555) were hybridized to the elongated staple strands of the DNA origami at a 5× molar excess for 60 min at 24°C, followed by spin column purification (100 kDa cut-off). Functionalized DNA origami platforms were seeded onto mobile PLBs decorated with B7-1 and ICAM-1 at 100 μm^{-2} and were used for experiments on the same day. Functionalization efficiency of DNA origami was determined via two-color colocalization microscopy as previously described (Hellmeier *et al*, 2021b).

Microscopy setup

For molecular live-cell imaging, we operated setup #1 and setup #2 at the Medical University of Vienna and setup #3 at the Technical University of Vienna. Setup #1 was a Leica DMI 4000B inverted microscope, which was used to image samples in epifluorescence or total internal reflection fluorescence mode (TIRF) with a 100× objective (HCX PL APO 100×, NA = 1.47, Leica) and a 20× objective (HCX PL Fluotar 20×, NA = 0.5, Leica). As setup #2, we operated an Eclipse Ti-E (Nikon) inverted microscope system that was equipped with a 100× objective (Nikon SR APO TIRF 100×, NA = 1.49) and a 20× objective (Nikon S Fluor, NA = 0.75).

If not otherwise mentioned, we used diode lasers with the wavelengths 405 nm (LBX-405-180), 488 nm (LBX-488-200), 515 nm (LBX-515-150), 532 nm (LCX-532-500), 561 nm (LCX-561-250), and 640 nm (LCX-640-500) coupled into a polarization-maintaining fiber with the L6Cc laser combiner box (Oxxius) on setups #1 and #2. For some experiments, we also employed diode lasers with the wavelengths 405 nm (OBIS-405-100), 488 nm (OBIS-488-150-LS), 515 nm (iBEAM-SMART-515-S, Toptica), 532 nm (OBIS-532-100-LS), 561 nm (OBIS-561-100-LS), and 637 nm (OBIS-637–140) in a "free-beam" configuration. Laser excitation light was cleaned up with bandpass filters that matched the corresponding wavelengths (Chroma) and focused with a two-lens telescope onto the back focal plane of the objectives. In addition, setup #1 was coupled to a mercury lamp (Leica EL6000), and setup #2 was coupled to a xenon

lamp (Lambda LS lamp, Sutter Instrument Company). Fluorescence lamp illumination was realized by using various sets of filters in the excitation path. The fluorescence lamp of setup #1 was equipped with two fast filter wheels with the following filters installed: ET340/26, ET387/11, ET370/36, ET474/27, ET554/23, and ET635/18 (Leica). The fluorescence lamp of setup #2 was equipped with one filter wheel (Sutter Instrument Company) with the following filters installed: ET340/26, ET387/11, ET370/36, ET474/27, ET554/23, and ET635/18 (Chroma). Setup #1 was further equipped with the beam splitters calcium cube FU2 (Leica), ZT405/488/561/647rpc and ZT405/488/532/647rpc (Chroma), and a custom Notch filter (405, 488, 532, and 642 nm, Chroma) to block the corresponding laser lights in the excitation pathway. Setup #2 was equipped with the beam splitters ZT405/488/561/647rpc, ZT405/488/532/640rpc, and ZT405/514/635rpc (Chroma), ET Dualb. "Sedat" CFP/YFP sbxm + HC510/20, and HC Quadband Fura, GFP, Cy3, and Cy5 (Semrock), and a custom Notch filter (405, 488, 532, and 642 nm, Chroma). In the emission path, setup #1 was operating a fast emission filter wheel (Leica) equipped with the custom bandpass filters ET455/50, ET525/36, ET605/52, and ET705/72 (Leica). Setup #2 was equipped with a filter wheel (Sutter Instrument Company) featuring the custom bandpass filters ET450/50, ET510/20, ET525/50, ET605/52, and ET700/75 (Chroma).

Emission light was recorded with the EMCCD camera (Andor iXon Ultra 897) or the CMOS prime95B (Teledyne Photometrics). To program and apply timing protocols and regulate hardware components, both setups were either operated with an 8-channel DAQ-card (National Instruments) or the USB-3114 analog and digital output system (Measurement Computing) controlled by the microscopy automation and image analysis software Metamorph (Molecular Devices). Setup #1 was additionally operated with the Leica software (Leica Suite) and μManager (Open Imaging). All setups were enclosed with a heating chamber (Leica (setup #1), Pecon (setup #2)) and equipped with a heating unit to adjust the temperature within the box.

Setup #3 was equipped with a monochromatic light source (Polychrome V, TILL Photonics) coupled to a Zeiss Axiovert 200 M, which was equipped with a 10× objective (UplanFL N 10×, NA = 0.3, Olympus), a 1.6 × tube lens, and the EMCCD camera Andor iXon Ultra 897. In the emission path, we installed a long-pass filter (T400lp, Chroma) and an emission filter (510/80 ET, Chroma). Precise temperature control was enabled by an in-house-built incubator equipped with a heating unit.

Conventional fluorescence microscopy

For conventional fluorescence microscopy analysis, BMDCs and B-cells were stained with saturating amounts of fluorophore-conjugated scF_V (e.g., 10 μg ml^{-1} 14.4.4 scF_V-AF647) or mAbs (14.4.4 mAb-AF647, 11–5.2 mAb-AF647, and IgG (H + L)-AF647) for 30 min on ice, and washed twice with 10 ml 1× HBSS (Gibco) supplemented with 1% FBS (Biowest), 2 mM $CaCl_2$, and 2 mM $MgCl_2$ (Merck) prior to seeding the cells onto ICAM-1-coated glass slides. Cells were treated with the Fc block CD16/CD32 (BioLegend) at 20 μg ml^{-1} for 15 min prior to the addition of mAbs. For experiments involving chemical fixation, cell samples were treated with 4% PFA (Thermo Fisher Scientific) in 1× PBS for 15 min at room temperature and subsequently washed in 1× HBSS (Gibco) supplemented with 1% FBS (Biowest), 2 mM $CaCl_2$ and 2 mM $MgCl_2$ (Merck) to stop the fixation reaction.

Mid-sections of BMDCs or B-cells were recorded as z-stacks (50 images with 0.3 μm spacing, total depth of z-stack: 15 μm) and deconvolved with the ImageJ plugin iterative deconvolve 3D, which is based on the DAMAS (Deconvolution Approach for the Mapping of Acoustic Sources) algorithm (Dougherty, 2005). The point spread function in x, y, and z used to deconvolve the images was measured with single fluorescent beads (TetraSpeck Fluorescent Microspheres).

Quantification of protein densities within cell membranes and PLBs

Rectangular regions of a cell or planar-supported lipid bilayer were specified for further calculations. Next, the camera background was subtracted from the intensity of the selected images and divided by the single-molecule intensity of the corresponding fluorophore. The intensity of single fluorescence emitters was obtained from cells or planar-supported lipid bilayers decorated with single molecules (e.g., 14.4.4 scF_V-AF647 or I-E^k/MCC-AF647) and imaged at a power density of 0.1–0.4 kW cm^{-2} and 10–20 ms illumination times. To avoid saturation of the camera when imaging highly fluorescent PLBs, we reduced either the power density by a factor of 10 using neutral density filters in the beam path (OD 1.0, Thorlabs) or reduced the linear EM gain of the EMCCD camera by a predetermined factor resulting in a tenfold reduction in pixel counts. Protein densities were specified as number of molecules μm^{-2}.

High-speed photoactivation localization microscopy (hsPALM)

0.1–0.5 × 10^6 BMDCs or B-cells were labeled with 20 μg ml^{-1} 14.4.4 scF_V-AF647-biotin for 30 min on ice, washed twice with 1× HBSS (Gibco) supplemented with 1% FBS (Biowest), 2 mM $CaCl_2$, and 2 mM $MgCl_2$ (Merck), and afterward incubated with excess amounts of mSav-cc-PS-CFP2 for 30 min on ice. Next, cells were washed twice and either kept on ice or allowed to spread on ICAM-1-coated glass slides for 1 to 5 min and were then directly subjected to live PALM imaging. Optionally, cell samples were fixed with 4% PFA (Thermo Fisher Scientific) in 1× PBS for 15 min at room temperature, washed, stored at 4°C (to complete fixation), and imaged either immediately after or the next day. PALM images were recorded in TIRF mode at 25°C. We recorded hsPALM image stacks only from adherent cells, a condition that was determined by one red image (637 nm laser excitation (OBIS-637-140), 705/72 emission filter) of the AF647-conjugated 14.4.4 scF_V-biotin seconds before streaming the hsPALM image stack. With the intention to excite and bleach PS-CFP2 in one single frame (with 2 ms illumination time and 0.3 ms readout time), we used the 488 nm laser line (OBIS-488-150-LS) with a power density of 3.5 kW cm^{-2}. After a short prebleach stream with 488 nm laser excitation (50 frames), we used continuous 405 nm laser excitation (OBIS-405-100) operated at a very low power density (1–10 W cm^{-2}) to photo-convert PS-CFP2 from cyan to green emission and filtered the emission channel with the bandpass filters ET525/36 (Leica) or ET525/50 (Chroma). With the use of the Andor iXon Ultra 897 EMCCD camera, we collected at a frame rate of 435 Hz 3,050 image frames (50 × 200 pixel) sufficient for one reconstructed super-resolution image in 7 s.

We obtained the blinking statistics of PS-CFP2 under the same experimental conditions (PFA fixed or unfixed) and with the same illumination settings and 488 nm power densities following a procedure we had previously published (Platzer *et al*, 2020). More

specifically, we decorated immobile PLBs with spatially well-separated mSav-abSTAR635P in complex with PS-CFP2 molecules which had been site-specifically biotinylated via an AVI-tag. Imaging of hundreds of different PLB positions was conducted at room temperature and in TIRF mode as described (Platzer *et al*, 2020). To visualize the position of single mSav-STAR635-PS-CFP2 molecules, we used the 637 nm laser line (OBIS-637-140) with a power density of 0.5–1.0 kW cm^{-2} and the emission bandpass filter ET700/75 (Chroma). We recorded 20 images to localize (and photo bleach) the mSav-STAR635 platform prior to streaming 3,050 frames to create the hsPALM stack for the PS-CFP2 blinking analysis.

Single-molecule blinking analysis of PS-CFP2 conjugated to the mSav-STAR635 platform was carried out as described (Platzer *et al*, 2020) with the following modifications: The position of mSav-STAR635 molecules was averaged by using the localization merging algorithm implemented in ThunderSTORM (Ovesny *et al*, 2014) with the following parameters: maximum t_{off} = 20 frames and maximum displacement = 100 nm. A localization cluster threshold was set to 30 to filter out extreme outliers. Data were pooled from two independent experiments.

PALM image analysis via Ripley's K was performed as described in Platzer *et al* (2020). We first selected for each cell a rectangular region of interest (ROI) with a maximum size specified by the boundaries of the cell (e.g., 3,000 × 3,000 nm). Single-molecule PS-CFP2 signals within the ROI were fitted with a Gaussian intensity distribution by maximum-likelihood estimation using the ImageJ plug-in ThunderSTORM and filtered for sigma (< 320 nm) and positional accuracy (< 150 nm). We obtained a positional accuracy of median of 51 nm for single PS-CFP2 signals with the illumination settings described above (Appendix Fig S6F). We then performed a qualitative Ripley's K analysis of a region of interest and compared the calculated maxima of the Ripley's K function of the cell-derived localization map with a simulated localization map, which represented a random distribution of molecules present at the same molecular density and exhibited features such as blinking behavior of PS-CFP2 and in selected cases diffusion parameters of respective molecules (Appendix Fig S8A and B). Of note, Ripley's K analysis of a ground truth localization map (after MBC) was compared to a simulated localization map, which represented only a random distribution of molecules present at the same molecular density (without blinking or diffusion parameters). Localization maps with an L(r)-*r* maxima mainly above the standard deviation of the associated simulated random distribution (within r = 250 nm) were registered to contain (partly or exclusively) clusters (Platzer *et al*, 2020).

PALM image analysis via label density variation was carried out as described by Baumgart *et al* (2016). After obtaining the X and Y coordinates for every localization as described above, we assigned a Gauss function with a sigma (σ) of 35 nm (that was cut at 2σ) to every localization within the sample regions. Briefly, overlapping Gauss functions were summed subpixel-wise after applying a threshold (from 0.5 to 4.5; here 1.0) to generate a three-dimensional cluster map (Fig 2E). Next, we calculated the density within the selected cluster regions (ρ; localizations μm^{-2}) and the relative area of selected cluster regions (η; cluster area divided by total area). The pair-wise numbers obtained for each sample were plotted in a ρ/η diagram and compared to a reference curve for randomly distributed localizations (equation 1). The reference curve was determined by simulating randomly distributed molecules under different conditions (variations in blinking statistics and thresholds) and applying a polynomial function that fits every scenario, as described by Baumgart *et al* (2016).

$$\rho = \rho 0\left(1 + 1.4 \times \eta^4\right) \quad (1)$$

Model-based correction (MBC) and DBSCAN analysis of PALM data

We corrected for multiple blinking artifacts in our PALM data with the MBC workflow introduced by Jensen *et al* (2022). To this end, we selected 3,000 × 3,000 nm regions (Appendix Fig S8A and B) within the recorded cells and saved the respective localization maps as .csv files containing the information for x (nm), y (nm), frame, and positional accuracy (nm). MBC was performed on the selected ROIs with default parameters (as suggested) and a framerate of 435 fps (2.3 ms time lag) using the provided R script. After MBC, we subjected the corrected localization maps, now containing ground truth fluorophore localizations, to Ripley's K analysis (to verify clusters over spatial randomness as described above), and DBSCAN analysis to characterize potential clusters (Ester *et al*, 1996), both implemented in Matlab.

DBSCAN analysis is based on the density distribution within a dataset and requires two parameters, *epsilon* (threshold for a neighborhood search radius) and *minpts* (minimum number of neighbors), to identify core points and assign them to clusters. All unconnected points are considered noise points. To facilitate the identification of clusters over noise in our datasets, we found *minpts* = 5 to be suitable for all investigated cell regions. The adequate choice of *epsilon* is at a threshold just large enough to minimize the number of noise points incorrectly assigned to clusters. We estimated *epsilon* for every cell region with a k-distance graph (Ester *et al*, 1996) and decreased this value (depending on the density of points) in steps of 10 until only noise points (i.e., percentage of molecules in clusters ~1%) were detected in the associated simulated random distribution as recommended by Endesfelder *et al* (2013). With this approach, we were able to determine the percentage of molecules within clusters, the number of molecules per cluster, and the number of detected clusters of I-E^k on activated BMDCs and B-cells and CD205 on activated BMDCs.

Single-molecule tracking

BMDCs and B-cells were stained with a single molecule dilution of the 14.4.4 scF_V-AF555 on ice for 30 min and washed twice with imaging buffer containing 1× HBSS (Gibco) supplemented with 1% FBS (Biowest), 2 mM $CaCl_2$ and 2 mM $MgCl_2$ (Merck). Cells were kept on ice or seeded onto ICAM-1-coated glass slides for imaging at 37°C and in TIRF mode. AF555 was excited with the use of a 532 nm laser (OBIS-532-100-LS), and the emission channel was cleaned up with the bandpass filter ET605/52. We recorded movies of single I-E^k (AF555-14.4.4 scF_V) localizations over 500 frames with a power density of 0.25–0.5 kW cm^{-2}, an illumination time of 10 ms, and a total time lag of 10.26–10.5 ms between two adjacent images (frame transfer mode).

For I-E^k recovery experiments, BMDCs and B-cells were pulsed for 12 and 6 h, respectively, with 50 μM MCC-PEG_2-biotin. We divided each cell sample into two aliquots. The first aliquot represented the total pool of I-E^k/MCC-PEG_2-biotin and was kept on ice. The second one was blocked with unlabeled monovalent

streptavidin for 30 min on ice, washed in imaging buffer, and again divided into two aliquots: One was incubated on ice for 10 min to serve as blocking control. The second one was incubated for 10 min at 37°C to allow for newly synthesized I-E^k molecules to arrive at the cell membrane via vesicular transport (recovered I-E^k fraction). Finally, all three sample groups representing (i) the total pool of I-E^k molecules, (ii) the blocking control, and (iii) the fraction of newly arrived I-E^k molecules were stained with abCAGE635-conjugated mSav (mSav-abCAGE635) for 5 min at room temperature and afterward washed once with 10 ml imaging buffer at room temperature. Stained BMDCs and B-cells were seeded onto ICAM-1-coated glass slides for immediate imaging at 37°C in TIRF mode. The photoactivatable dye abCAGE635 was activated with low-powered 405 nm laser illumination (0.01–0.1 W cm^{-2}) and excited with 637 nm laser light (OBIS-637–140) with a power density of 0.1–0.2 kW cm^{-2}. The emission channel was cleaned up with the bandpass filter ET705/72. We recorded movies of single I-E^k/MCC-PEG_2-biotin (mSav-abCAGE635) trajectories for up to 1,000 frames with an illumination time of 10 ms and a total time lag of 10.26 ms (100 × 100-pixel ROI). B-cells and BMDCs stained with mSav-AF555 were excited with the use of a 532 nm laser (0.25–0.5 kW cm^{-2}), and the emission channel was cleaned up with the ET605/52 bandpass filter.

Single fluorescent emitters (e.g., I-E^k labeled with 14.4.4 scF_V-AF555) were tracked using a custom-written algorithm in Matlab. We calculated the XY localization and intensity of each fluorophore detected within the image stack using the ImageJ plugin ThunderSTORM and filtered for sigma (< 320 nm) and positional accuracy (< 150 nm). Single localizations within the imaging stack were combined into trajectories based on a published algorithm (Schutz *et al*, 1997). We calculated the mean square displacement (MSD) describing the average of the square displacements between two points of the trajectory with the single molecule position $r(t)$ and the accuracy σ according to equation (2).

$$\mathrm{MSD}(t_{lag}) = <\left(r \times \left(t + t_{lag}\right) - r(t)\right)^2> \quad (2)$$

The first two MSD values as a function of t_{lag} were used to calculate the diffusion coefficient (D) for each trajectory according to $MSD = 4 \times D \times t_{lag} + 4\sigma^2$ (Wieser *et al*, 2007). Multiple mobile fractions were discriminated by analyzing the step-size distributions of square displacements for several time lags (Schutz *et al*, 1997). By assuming free Brownian motion of one mobile fraction, the cumulative probability for finding a square displacement smaller than r^2 is given by equation (3).

$$P = 1 - exp\left(-\frac{r^2}{4Dt_{lag}}\right) \quad (3)$$

Two different fractions α and $(1-\alpha)$ with diffusion coefficients D_1 and D_2 can be distinguished by fitting the bi-exponential function (equation 4).

$$P = 1 - \alpha \times exp\left(-\frac{r^2}{4D_1 t_{lag}}\right) - (1-\alpha) \times exp\left(-\frac{r^2}{4D_2 t_{lag}}\right) \quad (4)$$

Thinning out clusters while conserving the stoichiometry of labeling (TOCCSL)

BMDCs and B-cells (0.25×10^6 to 0.5×10^6) were labeled for 30 min on ice with 20 µg ml^{-1} 14.4.4 scF_V-AF647-biotin, then washed with 1× HBSS (Gibco) supplemented with 1% FBS (Biowest), 2 mM $CaCl_2$, and 2 mM $MgCl_2$ (Merck), and subsequently allowed to adhere on ICAM-1-coated glass slides before TOCCSL imaging. To reduce the likelihood of oligomer detection and create a monomer control, we premixed the 14.4.4 scF_V-AF647-biotin with unlabeled 14.4.4 scF_V-biotin in a 1:10 to 1:15 ratio before labeling the cells. To serve as fluorescence dimer control, we premixed the 14.4.4 scF_V-AF647-biotin with mSav-AF647 at a 1:5 ratio for 30 min on ice prior to staining the cells with the conjugate. To induce dimerization directly on cells, we first stained BMDCs with 20 µg ml^{-1} 14.4.4 scF_V-AF647-biotin, washed, and treated the samples with 125 nM divalent streptavidin (*trans* configuration). TOCCSL experiments were performed on setup #2 in TIRF mode and at room temperature as described (Moertelmaier *et al*, 2005; Brameshuber *et al*, 2010, 2018; Ruprecht *et al*, 2010). I-E^k-bound 14.4.4 scF_V-AF647 was excited with the 640 nm laser (LCX-640-500) or the 637 nm laser (OBIS-637-140) at a power density of 0.1–0.2 kW cm^{-2} and recorded with an illumination time of 20 ms. The emission channel was filtered with the ET700/75 bandpass filter (Chroma). The unmasked cell region of interest was adjusted with a slit aperture (width 5–10 µm) and photobleached for a total time of 750–1,000 ms with a power density of 2–3 kW cm^{-2} in epifluorescence and TIRF mode. To confirm that photobleaching was complete, we included in some experiments a control image directly following the bleach pulse (100–750 ms delay). In order to observe well-separated fluorescence emitters diffusing back into the photobleached region, the recovery time was adjusted to 2–10 s for cells that had been stained under saturating conditions and 2–20 s for monomer controls. The first image after passing the recovery time was used to measure brightness values of the recovered as of then unbleached molecules.

Data recorded from TOCCSL experiments were analyzed as described in Brameshuber *et al* (2010). We applied a custom-made Matlab-based maximum-likelihood estimator to extract XY coordinates, integrated brightness B values, the full width at half-maximum (FWHM) and the local background of individual fluorescence signals in the TOCCSL images (Moertelmaier *et al*, 2005). The brightness values B of single AF647-scFv molecules pooled from the TOCCSL images of the monomer control (1:15 premix of labeled to unlabeled 14.4.4 scF_V) were used to calculate the probability density function (pdf) of monomers, $\rho_1(B)$. Because of the independent photon emission process of single fluorescent emitters, the corresponding pdfs of N colocalized emitters can be calculated by a series of convolution integrals according to equation (5).

$$\rho_N(B) = \int_1^{\rho} (B')\rho_{N-1}(B - B')dB' \quad (5)$$

A weighted linear combination (α_N) of these pdfs was used to calculate the brightness distribution of a mixed population of monomers and higher order multimers.

$$\rho(B) = \sum_{N=1}^{N_{\max}} \alpha_N \rho_N(B) \quad (6)$$

A minimum of 180 brightness values was applied to calculate $\rho_1(B)$ and $\rho_N(B)$ from all TOCCSL images of multiple cells of one experimental condition. A least-square fit with equation (6) was employed to determine the weights of the individual pdfs, α_N, with $\sum_{N=1}^{N_{max}} \alpha_N = 1$.

Ensemble FRET imaging

T-cells (0.25×10^6) were stained with saturating amounts (12 μg ml^{-1}) of H57 scF$_V$-AF555 (FRET donor) for 30 min on ice and washed into imaging buffer (10 ml of 1× HBSS (Gibco) supplemented with 0.4 mg ml^{-1} ovalbumin (Merck), 2 mM $CaCl_2$ and 2 mM $MgCl_2$ (Merck), and kept on ice until imaging proceeded. Stained T-cells were allowed to settle for 2 min on functionalized PLBs, which were equipped with unlabeled ICAM-1, B7-1 (100 molecules μm^{-2}), and I-E^k/peptide-AF647 (FRET acceptor) at different densities. Synaptic FRET was recorded as a consequence of TCR-pMHCII binding for up to 10 min (i.e., 2–12 min after cells had made first bilayer contact).

To examine the oligomeric state of pMHCIIs, 0.25×10^6 to 0.5×10^6 BMDCs and B-cells were labeled on ice for 30 min with the FRET donor 14.4.4 scF$_V$-AF647 and the FRET acceptor 14.4.4 scF$_V$-AF555 (10 μg ml^{-1} each) using premixed (1:1, 1:2, 1:3, or 1:4) AF647 and AF555 probe cocktails. Cells were then washed with imaging buffer (1× HBSS (Gibco)) supplemented with 1% FBS (Biowest), 2 mM $CaCl_2$, and 2 mM $MgCl_2$ (Merck) and subsequently allowed to adhere on ICAM-1-coated glass slides prior to imaging in TIRF mode at 22.5°C. To dimerize I-E^k within the cell membrane, 0.5×10^6 BMDCs were stained for 30 min on ice with 14.4.4 scF$_V$-AF647-biotin and 14.4.4 scF$_V$-AF555-biotin premixed at a 1:1 ratio and subsequently washed with imaging buffer (1× HBSS (Gibco) supplemented with 1% FBS (Biowest), 2 mM $CaCl_2$, and 2 mM $MgCl_2$ (Merck)). Biotinylated scF$_V$ were then crosslinked with varying concentrations of divalent streptavidin (ranging from 1 to 1,000 nM) for 30 min on ice to induce I-E^k-dimer formation, before allowing the cells to adhere to ICAM-1-coated glass slides.

For FRET measurements of bilayer-resident pMHCIIs, we functionalized PLBs with unlabeled I-E^k/MCC which were then labeled using increasing amounts of 14.4.4 scF$_V$-AF555 and 14.4.4 scF$_V$-AF647 which had been premixed at a 1:1, 1:2, or 1:3 ratio. PLBs were washed with imaging buffer (1× HBSS (Gibco) supplemented with 1% FBS (Biowest), 2 mM $CaCl_2$, and 2 mM $MgCl_2$ (Merck)) prior to imaging.

For all FRET experiments, the emission beam path was separated into two spectral channels employing an Optosplit 2 device (Cairn Research) which was equipped with a beam splitter (ZT640rdc, Chroma) and adequate emission bandpass filters (ET575/50 or ET640SP, ET655LP, Chroma). The following alternating excitation protocol was used to record FRET donor and FRET acceptor channels: a low-intensity AF647 acquisition (to monitor the AF647 signal, OBIS-637-140, power < 0.01 kW cm^{-2}) was succeeded by a low-intensity AF555/FRET acquisition (to record the AF555 and FRET signal before FRET acceptor photobleaching, OBIS-532-100-LS, power ~0.01 kW cm^{-2}), followed by a high-intensity 640-nm bleach pulse (to ablate AF647, power > 2 kW cm^{-2}), a second low-intensity AF647 acquisition (to verify AF647 ablation, power ~0.01 kW cm^{-2}), and finally, a second AF555/FRET acquisition (to record the AF555 signal after FRET acceptor bleaching and verify FRET ablation, power ~ 0.01 kW cm^{-2}). Time lapsing between the two AF555/FRET acquisitions was less than 500 ms. Quantitative imaging was ensured by minimizing photobleaching at a given illumination time of 30 ms. To this end, the power levels of the 532 nm FRET donor excitation laser were adjusted to keep photobleaching between consecutive images below 1%. I-E^k/peptide-AF488 was excited with the 488 nm laser (OBIS-488-150-LS) at a power density of 0.1–0.2 kW cm^{-2} and the emission was cleaned up employing the ET525/50 (Chroma) filter.

For FRET-sensitized emission analysis, donor and acceptor channels were superimposed using an affine transformation matrix (including shift, stretch, rotation, and tilt) and intensity registration, both generated from a fluorescent bead reference (TetraSpeck Fluorescent Microspheres Size Kit, Thermo Fisher Scientific). Net fluorescence intensities were obtained by pixel-wise subtraction of the camera background from the raw-intensity images. To compensate for laser illumination profiles, we performed a pixel-wise flatfield correction by means of median averaging 10 separately recorded PLB samples representing a similar fluorophore density as the sample employed for FRET measurements.

FRET donor recovery after FRET acceptor photobleaching analysis was performed as described (Huppa *et al*, 2010). After background subtraction, the AF555 intensity (FRET donor) before FRET acceptor photobleaching (*DDpre*) was subtracted from the AF555 intensity after FRET acceptor photobleaching (*DDpost*). The difference was then divided by *DDpost* to obtain the FRET yield according to equation (7).

$$\text{FRET yield } (E_{FRET}) = \frac{DDpost - DDpre}{DDpost\text{–background}} \tag{7}$$

Apparent FRET efficiencies were calculated based on equation (8) with α = cross-excitation, β = bleed through, DA = donor excitation, acceptor channel (FRET channel), AA = acceptor excitation, and acceptor channel (AF647 signal).

$$\text{FRET}_{\text{apparent}} = \frac{K \times DA}{DDpre}; \text{with } K = \frac{DDpost - DDpre}{DA - \alpha \times AA - \beta \times DDpre} \tag{8}$$

The TCR occupancy, that is, the ratio of ligand-engaged and total TCRs was calculated as shown in equation (9):

$$\text{TCR occupancy} = \frac{K \times DA}{DDpost} \times R; \text{with } R = \frac{I_{sm}\ Donor}{I_{sm}\ FRET}; \tag{9}$$

with I_{sm} *Donor* = single-molecule FRET donor intensity and I_{sm} *FRET* = single-molecule FRET intensity, as determined experimentally by the average intensity of single-molecule FRET events and the average intensity of single-molecule FRET donor signals (see single-molecule FRET imaging and Appendix Fig S15D). Additionally, we estimated R based on the transmitted spectrum of light of the filter sets ET575/50 (62.1%) and ET655LP (74.3%) as follows:

$$R_{filter} = \%FRET\ donor / \%FRET\ acceptor \times 0.78 = 1.07.$$

Since the TCR occupancy is directly proportional to the FRET yield (Axmann *et al*, 2015), we established a relationship between these two parameters by plotting the synaptic FRET yields obtained from FRET DRAAP measurements against TCR occupancies obtained from the same T-cell synapses (Appendix Fig S15F). By fitting a linear regression, we experimentally determined the

conversion factor $C = 1.21$ (for $R_{exp} = 1.0$) to calculate TCR occupancies directly from FRET yields according to equation (10).

$$\text{TCR occupancy} = E_{FRET} \times C \quad (10)$$

The experimentally determined conversion factor $C = 1.21$ was comparable with the estimated values of $C = 1.29$ (for $R_{filter} = 1.07$) and $C = 1.28$ (obtained from the maximal FRET efficiency of the FRET system max $E_{FRET} = 1/0.78 = 1.28$).

Single-molecule FRET imaging

Single-molecule FRET recordings were conducted with the same experimental setup, hardware settings, and filters as used for recording ensemble FRET. To attenuate bleed through from the FRET donor fluorophore into the FRET acceptor channel, we opted to stain approximately 10% of the TCRs on T-cells with the H57 scF_V-AF555 by premixing one part of H57 scF_V-AF555 with nine parts of unlabeled H57 scF_V prior to cell staining (total 10 μg ml^{-1}). We also adjusted I-E^k/MCC-AF647 densities on PLBs to 5–30 I-E^k μm^{-2}, to reduce cross-excitation of the FRET acceptor fluorophore.

To visualize earliest single TCR-pMHCII-binding events, we employed, in addition, the caged MCC peptide derivative ANERADLIAYLK[NVOC]QATKGGSC-AF647 loaded onto I-E^k (I-E^k/MCC[NVOC]-AF647) which represents a null ligand unless it becomes uncaged by means of a short 405 nm laser pulse (0.17 kW cm^{-2}, 100 ms). 1–2 seconds after the 405 nm pulse, individual TCR-pMHCII-binding events appeared as single-molecule FRET events, disappeared in single steps, and aligned with single FRET acceptor fluorophores (I-E^k/MCC-AF647). We recorded smFRET events with an illumination time of 20 ms and applied a 532 nm power density of 0.1 kW cm^{-2} (OBIS-532-100-LS or LCX-532-500) to excite the donor fluorophore AF555 and a 640 nm power density of 0.05 kW cm^{-2} (OBIS-637–140 or LCX-640-500) to excite the acceptor fluorophore AF647. I-E^k/K99A-AF488 was excited with the 488 nm laser (LBX-488-200) at a power density of 0.1–0.2 kW cm^{-2} and the emission was filtered employing an ET525/50 (Chroma) filter.

Intensity and positional accuracy of single-molecule donor and single-molecule FRET events as a consequence of TCR-pMHCII binding were calculated with the ImageJ plugin ThunderSTORM (Ovesny *et al*, 2014) and filtered for sigma (< 320 nm) and positional accuracy (< 150 nm).

To measure the synaptic off-rate of 5c.c7 TCR:I-E^k/MCC interactions at 26°C in the presence or absence of I-E^k/K99A, we adjusted the I-E^k/MCC-AF647 density on PLBs to 11 I-E^k/MCC-AF647 μm^{-2} and ICAM-1 and B7-1 to 100 μm^{-2}. I-E^k/K99A-AF488 was either completely absent or present at a density of 1,060 I-E^k/K99A μm^{-2}. For off-rate determination, we recorded the appearance of smFRET traces at different time lags (56, 84, 252, 476, 924, and 1,820 ms) to correct for photobleaching. We then listed the smFRET traces according to their trajectory length and created a normalized inverse cumulative decay function for each time lag as described in Axmann *et al* (2015). The resulting decay function was fitted with a single exponential decay function (start 1.0, plateau 0) to calculate (app $t_{off} = 1/\text{app } k_{off}$) the apparent lifetime (Appendix Fig S17E). Lastly, we plotted the calculated apparent lifetimes against the respective time lags and fitted the lifetime (t_{off}) and the bleach constant c_{bleach} based on equation (11).

$$\text{app } t_{off} = \left(t_{off} / \frac{t_{off}}{c_{bleach}} \right) + t_{lag} \quad (11)$$

Calcium imaging

Intracellular calcium levels were measured with the ratio-metric dye Fura-2 (Thermo Fischer Scientific) as published (Roe *et al*, 1990). 1–2 × 10^6 antigen-experienced 5c.c7 TCR-transgenic T-cells were incubated with 2 μM Fura-2 in T-cell growth medium for 15–20 min at room temperature and subsequently washed with warm (room temperature) imaging buffer (14 ml of 1× HBSS (Gibco) supplemented with 1% FBS (Biowest), and 2 mM $CaCl_2$ and 2 mM $MgCl_2$ (Merck)). Immediately afterward, T-cells were seeded onto functionalized PLBs featuring increasing densities of I-E^k in complex with agonist or non-agonist (bystander) peptides and unlabeled B7-1 and ICAM-1 (100 μm^{-2}). The usage of 16-well Nunc LabTek chambers (Thermo Fisher Scientific) enabled us to record up to 12 different conditions (i.e., various or different concentrations of I-E^k) in a single experimental run. Calcium experiments were carried out on setup #1 or setup #3 at 37°C. On setup #1, Fura-2 was excited using a monochromatic light source (Leica) coupled into an inverted Leica DMI4000B microscope that was equipped with a 20× objective (HCX PL Fluotar 20×, NA = 0.5, Leica), the dichroic beamsplitter FU2 (Leica), and the bandpass filter ET525/36 (Leica). Calcium signaling was measured ratiometrically by continuous switching between 340 and 387 nm excitation, which was achieved with the use of a fast excitation filter wheel (Leica) featuring the excitation bandpass filters 340/26 and 387/11 (Leica). The total recording time was 10–20 min with an image recorded every 15–20 s. An automated XY stage (Leica) allowed fast changes between different positions (i.e., LabTek chamber wells). Precise temperature control was carried out with a heating unit and a box enclosing the microscope (Leica).

For calcium imaging of T-cells approaching DNA origami structures, we used setup #3. Fura-2 was excited with a monochromatic light source (Polychrome V, TILL Photonics) coupled to a Zeiss Axiovert 200 M which was equipped with a 10× objective (UplanFL N 10×, NA = 0.3, Olympus), a 1.6× tube lens, a long-pass filter (T400lp, Chroma), the emission filter ET510/80 (Chroma), and the EMCCD camera Andor iXon Ultra 897. Imaging was performed with excitation at 340 and 380 nm with illumination times of 50 and 10 ms, respectively. The total recording time was 10 min with one image per second. Experiments were carried out at 37°C using an in-house-built incubator equipped with a heating unit for precise temperature control.

Calcium image analysis was carried out either with a custom code written in Matlab (based on Salles *et al*, 2013) or as described in Hellmeier *et al* (2021b). In detail, we first generated the ratio image of the 340 nm / 380 nm image for every frame. Individual T-cells were then tracked using an in-house Matlab algorithm based on Gao & Kilfoil (2009) and the positional information of each cell was used to extract the intensity value from the ratio image stack. Fura-2 intensity traces were either normalized to the starting value at timepoint 0 or the median of all Fura-2 intensity traces of a

negative control (ICAM-1,100 μm^{-2}, B7-1,100 μm^{-2}). Traces were categorized into "activating," oscillatory, and "non-activating" based on an activation threshold defined by a receiver operating curve between a negative control and a positive control (I-E^k/MCC > 10 μm^{-2}, ICAM-1,100 μm^{-2}, and B7-1,100 μm^{-2}). T-cells were categorized as "activating" when the Fura-2 intensity value remained 80% of the entire trace above the threshold, "non-activating" when it remained 80% of the trace below the threshold, otherwise the cell was classified as oscillatory. The generation of dose–response curves and the bootstrap analysis of EC50 data is best described in Hellmeier *et al* (2021b). The calcium imaging data were fitted to a three- (hillslope $n = 1.0$) or four-parameter dose–response curve with equation (12) to extract the activation threshold (T_A) at half-maximum response. Statistical significance between obtained values $T_{A,1}$ and $T_{A,2}$ for two different data sets was determined via a bootstrap ratio test (Appendix Table S1C) as described in MacKinnon (2009) and Wheeler *et al* (2006).

$$Y = Bottom + \frac{(X^n \times (Top - Bottom))}{(X^n + T_A^n)} \quad (12)$$

STED microscopy

BMDCs and B-cells (0.25×10^6 to 0.5×10^6) were stained with 20 μg ml^{-1} 14.4.4 scF$_V$-abSTAR635P for 30 min on ice and washed with imaging buffer (1× HBSS (Gibco) supplemented with 1% FBS (Biowest), 2 mM $CaCl_2$ and 2 mM $MgCl_2$ (Merck)). Cells were allowed to adhere on ICAM-1-coated glass slides for 10 min at 25°C before fixation. Cells were stained with limited amounts of 14.4.4 scF$_V$ abSTAR635P to visualize single fluorescent emitters. Samples were fixed for 15 min at room temperature applying 4% PFA (Thermo Fisher Scientific), washed with 1× PBS and imaging buffer, mounted in Abberior Mount Solid (Abberior), and stored at 4°C until imaging. STED imaging was performed on a Zeiss Axio Imager A2 upright microscope equipped with a 100× objective (alpha-Plan-Apochromat 100×, NA = 1.46, Oil DIC M27, Zeiss) and the Stedycon super-resolution microscopy unit (Abberior Instruments). Scanning was performed with the built-in QUAD beam scanner with a pixel dwell time of 250 ms at a pixel size of 25 nm. A pulsed 640 nm diode laser with an output of 1.2 mW at 40 MHz (max. 5 mW) and > 20 pJ per pulse (< 150 ps) was used to excite abSTAR635P molecules, and a pulsed 775 nm STED depletion laser with an output of 1.25 W and > 30 nJ per pulse (jitter < 100 ps) was used for stimulated emission depletion. Time gating delay was set to 1 ns and gate width to 6 ns. The Stedycon was controlled via a Chrome browser-based software provided by the manufacturer (Abberior Instruments).

Simulations and software used for analysis

Microscopy images were processed and analyzed with the open-source image processing package Fiji (Schindelin *et al*, 2012). More extensive image analysis was carried out with custom-written algorithms in Matlab (MathWorks). Frame, XY localization, intensity, and positional accuracy of single molecules were calculated with the ImageJ plugin ThunderSTORM (Ovesny *et al*, 2014). Matlab, GraphPad Prism 10 (GraphPad), and R (r project) were used for statistical data analysis and evaluation.

STED autocorrelation analysis

To judge the randomness of pMHCII in STED microscopy data, we calculated ACFs for four different 2.5 × 2.5 μm regions of interest per cell and compared these experimental samples with ACFs of simulated STED images of randomly distributed molecules obtained with experimentally determined parameters (Sengupta *et al*, 2011). To characterize the point-spread function of the imaging system, we sparsely labeled activated BMDCs and B-cells with the 14.4.4 scF$_V$-abSTAR65P and fitted the recorded single molecules signals using the ImageJ plugin ThunderSTORM. The background was determined from the mean fluorescence signal of non-fluorescent areas within each region of interest. I-E^k densities were calculated by dividing the background subtracted mean intensity in fully labeled cells by the average single-molecule intensity, which yielded 15–108 I-E^k molecules μm^{-2} on activated BMDCs and 24–44 I-E^k molecules μm^{-2} on activated B-cells. Simulated images of random signal distributions were then generated using the parameters intensity (I), and sigma (σ) derived from single-molecule signals and background and molecular density from the cell regions of interest using an in-house written Matlab code (for details see Rossboth *et al*, 2018).

Simulation of random distributions for blinking analysis via Ripley's K

A region of interest (e.g., 3,000 × 3,000 nm) featuring randomly distributed molecules at a specified density was simulated as described (Rossboth *et al*, 2018; Platzer *et al*, 2020). To arrive at simulations to be used for comparison with cell-associated PALM data, the approximate expression levels of I-E^k (14.4.4 scF$_V$-AF647-biotin + mSav-cc-PSCFP2), CD205 (NLDC-145 mAb-AF647-biotin + mSav-cc-PSCFP2), and CD18 (M18/2 mAb-AF647-biotin + mSav-cc-PS-CFP2) within a region of interest were determined by dividing the number of PS-CFP2 localizations with the mean number of detections N per fluorescence molecule as obtained from the blinking analysis (Appendix Fig S7A). The experimentally derived probability distribution of the number of detections N was randomly assigned to every simulated localization to include the blinking of PS-CFP2. To arrive at simulations to be used for comparison with PALM data after MBC, we determined the number of PS-CFP2 localizations from the corrected region and set the mean number of detections N per fluorescence molecule to $N = 1$.

Finally, all positions were shifted into a random direction by a distance drawn from a normal distribution with an average value of zero and localization precision (51 ± 12 nm) as standard deviation to simulate a PFA-fixed scenario. In order to simulate live-cell scenarios, we additionally shifted the localizations based on the diffusion parameters F (fast diffusing fraction), D_1 (diffusion constant of fast-moving fraction), and D_2 (diffusion constant of slowly moving fraction) of I-E^k on BMDCs ($F = 0.83$, $D_1 = 0.284$ μm^2 s^{-1}, $D_2 = 0.046$ μm^2 s^{-1}, Appendix Fig S7B), I-E^k on B-cells ($F = 0.77$, $D_1 = 0.150$ μm^2 s^{-1}, $D_2 = 0.024$ μm^2 s^{-1}, Appendix Fig S7B), CD205 ($F = 0.9$, $D_1 = 0.065$ μm^2 s^{-1}, $D_2 = 0.0006$ μm^2 s^{-1} (Manzo *et al*, 2012)), and CD18 ($F = 0.3$, $D_1 = 0.03$ μm^2 s^{-1}, $D_2 = 0.0$ μm^2 s^{-1} (Mukherjee *et al*, 1998)), and a time lag of 2.3 ms.

Monte-Carlo simulation of cluster detection using PALM

Ripley's K functions were determined from Monte-Carlo simulations of nanoclusters with a cluster radius of 20, 40, 60, or 100 nm, a fraction of molecules residing inside clusters between 20 and 100%, 3,

5, 10, 15, and 20 clusters μm^{-2}, an average molecular density of 100 molecules μm^{-2}, and the experimentally determined blinking statistics of PS-CFP2 determined under 4% PFA-fixed and non-fixed imaging conditions (Appendix Fig S7A). Functions were compared to those calculated from random localization distributions and categorized as "Resolvable," "Borderline," or "Not resolvable" as described in Platzer *et al* (2020).

Monte-Carlo simulation of TOCCSL

TOCCSL results were simulated based on experimentally derived parameters using a Monte-Carlo–based approach as outlined in detail in Bodner *et al* (2023). In brief, a cell size of 10.5 × 10.5 μm^2 containing 500 molecules μm^{-2} diffusing with an average diffusion constant of 0.244 $\mu m^2\ s^{-1}$ ($D = 0.83*0.284 + 0.17*0.046\ \mu m^2\ s^{-1}$, see Appendix Fig S7B) was simulated. An area of 7 × 7 μm^2 was photobleached for 750 ms with bleaching parameters derived from photobleaching curves of AF647 illuminated with a laser power density of 3 kW cm^{-2} and a diffraction-affected laser intensity profile as determined experimentally. For TOCCSL simulations, the fraction of molecular dimers was varied between 3 and 100% while keeping the overall density of molecules constant. For each dimer fraction, the fraction of detected dimers after a recovery time of 2 s was determined from the simulations. Simulations were repeated 1,000 times for each dimer fraction. The 5% detection level of the TOCCSL method is described in Brameshuber & Schutz (2012).

Monte-Carlo simulation of FRET efficiency

FRET efficiencies of randomly distributed donor and acceptor molecules at increasing densities were simulated as described (Brameshuber *et al*, 2018). We used algorithms custom written in Matlab to simulate random X and Y positions of pMHCII molecules for increasing surface densities between 20 and 1,000 molecules μm^{-2} (increment 20). Due to higher simulated surface densities compared to our previous study (Brameshuber *et al*, 2018), we considered not only the nearest neighbor of every donor molecule for calculation of the FRET efficiency but also the second nearest neighbor. To this end, the distances $d_{1,2}$ between every donor molecule and the two nearest acceptor molecules were calculated and used to determine the FRET efficiencies $E_{1,2}$, according to equation (13), with $R_0 = 5.1$ nm, the Förster radius for the AF555/AF647 dye pair.

$$E_{1,2} = \frac{1}{1 + \left(\frac{d_{1,2}}{R_0}\right)^6} \tag{13}$$

The overall FRET efficiency for a donor with two acceptor molecules (Koushik *et al*, 2009) was calculated according to equation (14).

$$E_{1,2} = \frac{\sum_{i=1}^{2} \frac{E_i}{1-E_i}}{1 + \sum_{i=1}^{2} \frac{E_i}{1-E_i}} \tag{14}$$

For every surface density, the simulation was repeated 20 times to arrive at a mean and range of FRET efficiencies. FRET efficiencies were plotted against the total density (sum of donor and acceptor molecules).

Data availability

Links to the software packages for analysis can be obtained from the cited papers or the corresponding authors. No additional software packages or primary datasets have been generated and deposited.

Expanded View for this article is available online.

Acknowledgements

We thank Magdalena Schneider (TU Wien) for updating the Matlab code for Ripley's K blinking analysis. We are grateful to Björn Lillemeier (Salk Institute for Biological Studies, US & Albert-Ludwigs-Universität Freiburg, Germany) and Michael Dustin (Oxford University) for generously supplying us with 5c.c7 αβTCR-transgenic mice. This work was financially supported by the Austrian Science Fund (FWF) through the PhD program Cell Communication in Health and Disease W1205 (RP, HS, JBH), the projects I4662-B (MB), I4740-B (CB), P32307-B (JG), V538-B26 (ES, JBH), and P25775-B2 (JBH), and the Vienna Science and Technology Fund (WWTF) projects LS13-030 (GJS, JG, JBH) and LS14-031 (JBH). Funding was further provided by a predoctoral fellowship from the Boehringer Ingelheim Fonds (RP).

Author contributions

René Platzer: Conceptualization; data curation; formal analysis; validation; investigation; methodology; writing – original draft; writing – review and editing. **Joschka Hellmeier:** Resources; software; methodology. **Janett Göhring:** Software; validation. **Iago Doel Perez:** Resources; methodology. **Philipp Schatzlmaier:** Validation; methodology. **Clara Bodner:** Formal analysis. **Margarete Focke-Tejkl:** Resources. **Gerhard J Schütz:** Conceptualization; supervision; funding acquisition. **Eva Sevcsik:** Resources; supervision; methodology. **Hannes Stockinger:** Conceptualization; resources; supervision. **Mario Brameshuber:** Conceptualization; resources; software; formal analysis; supervision; methodology; writing – original draft; writing – review and editing. **Johannes B Huppa:** Conceptualization; resources; formal analysis; supervision; funding acquisition; validation; investigation; methodology; writing – original draft; project administration; writing – review and editing.

Disclosure and competing interests statement

The authors declare that they have no conflict of interest.

References

Anderson HA, Hiltbold EM, Roche PA (2000) Concentration of MHC class II molecules in lipid rafts facilitates antigen presentation. *Nat Immunol* 1: 156–162

Anikeeva N, Gakamsky D, Scholler J, Sykulev Y (2012) Evidence that the density of self peptide-MHC ligands regulates T-cell receptor signaling. *PLoS ONE* 7: e41466

Annibale P, Vanni S, Scarselli M, Rothlisberger U, Radenovic A (2011) Identification of clustering artifacts in photoactivated localization microscopy. *Nat Methods* 8: 527–528

Axmann M, Schutz GJ, Huppa JB (2015) Measuring TCR-pMHC binding in situ using a FRET-based microscopy assay. *J Vis Exp* e53157

Baumgart F, Arnold AM, Leskovar K, Staszek K, Folser M, Weghuber J, Stockinger H, Schutz GJ (2016) Varying label density allows artifact-free analysis of membrane-protein nanoclusters. *Nat Methods* 13: 661–664

Betzig E, Patterson GH, Sougrat R, Lindwasser OW, Olenych S, Bonifacino JS, Davidson MW, Lippincott-Schwartz J, Hess HF (2006) Imaging intracellular fluorescent proteins at nanometer resolution. *Science* 313: 1642–1645

Bodner C, Kiesenhofer D, Schutz GJ, Brameshuber M (2023) Monte Carlo simulations for the evaluation of oligomerization data in TOCCSL experiments. *Biophys J* 122: 2367–2380

Bohrer CH, Yang X, Thakur S, Weng X, Tenner B, McQuillen R, Ross B, Wooten M, Chen X, Zhang J *et al* (2021) A pairwise distance distribution correction (DDC) algorithm to eliminate blinking-caused artifacts in SMLM. *Nat Methods* 18: 669–677

Bosch B, Heipertz EL, Drake JR, Roche PA (2013) Major histocompatibility complex (MHC) class II-peptide complexes arrive at the plasma membrane in cholesterol-rich microclusters. *J Biol Chem* 288: 13236–13242

Brameshuber M, Schutz GJ (2012) Detection and quantification of biomolecular association in living cells using single-molecule microscopy. *Methods Enzymol* 505: 159–186

Brameshuber M, Weghuber J, Ruprecht V, Gombos I, Horvath I, Vigh L, Eckerstorfer P, Kiss E, Stockinger H, Schutz GJ (2010) Imaging of mobile long-lived nanoplatforms in the live cell plasma membrane. *J Biol Chem* 285: 41765–41771

Brameshuber M, Kellner F, Rossboth BK, Ta H, Alge K, Sevcsik E, Gohring J, Axmann M, Baumgart F, Gascoigne NRJ *et al* (2018) Monomeric TCRs drive T cell antigen recognition. *Nat Immunol* 19: 487–496

Bromley SK, Burack WR, Johnson KG, Somersalo K, Sims TN, Sumen C, Davis MM, Shaw AS, Allen PM, Dustin ML (2001) The immunological synapse. *Annu Rev Immunol* 19: 375–396

Brown JH, Jardetzky TS, Gorga JC, Stern LJ, Urban RG, Strominger JL, Wiley DC (1993) Three-dimensional structure of the human class II histocompatibility antigen HLA-DR1. *Nature* 364: 33–39

Chevallet M, Luche S, Rabilloud T (2006) Silver staining of proteins in polyacrylamide gels. *Nat Protoc* 1: 1852–1858

Cochran JR, Cameron TO, Stern LJ (2000) The relationship of MHC-peptide binding and T cell activation probed using chemically defined MHC class II oligomers. *Immunity* 12: 241–250

Corr M, Slanetz AE, Boyd LF, Jelonek MT, Khilko S, Al-Ramadi BK, Kim YS, Maher SE, Bothwell AL, Margulies DH (1994) T cell receptor-MHC class I peptide interactions: affinity, kinetics, and specificity. *Science* 265: 946–949

Davis MM, Boniface JJ, Reich Z, Lyons D, Hampl J, Arden B, Chien Y (1998) Ligand recognition by alpha beta T cell receptors. *Annu Rev Immunol* 16: 523–544

DeMond AL, Starr T, Dustin ML, Groves JT (2006) Control of antigen presentation with a photoreleasable agonist peptide. *J Am Chem Soc* 128: 15354–15355

Dougherty R (2005) Extensions of DAMAS and benefits and limitations of deconvolution in beamforming. 11th AIAA/CEAS Aeroacoustics Conference

Dyballa N, Metzger S (2009) Fast and sensitive colloidal coomassie G-250 staining for proteins in polyacrylamide gels. *J Vis Exp* 1431

Ebert PJ, Jiang S, Xie J, Li QJ, Davis MM (2009) An endogenous positively selecting peptide enhances mature T cell responses and becomes an autoantigen in the absence of microRNA miR-181a. *Nat Immunol* 10: 1162–1169

Endesfelder U, Finan K, Holden SJ, Cook PR, Kapanidis AN, Heilemann M (2013) Multiscale spatial organization of RNA polymerase in *Escherichia coli*. *Biophys J* 105: 172–181

Ester M, Kriegel H-P, Sander J, Xiaowei X (1996) *A density-based algorithm for discovering clusters in large spatial databases with noise*, pp 226–231. Portland, OR: AAAI Press

Fairhead M, Krndija D, Lowe ED, Howarth M (2014) Plug-and-play pairing via defined divalent streptavidins. *J Mol Biol* 426: 199–214

Feng Y, Brazin KN, Kobayashi E, Mallis RJ, Reinherz EL, Lang MJ (2017) Mechanosensing drives acuity of alphabeta T-cell recognition. *Proc Natl Acad Sci USA* 114: E8204–E8213

Fremont DH, Dai S, Chiang H, Crawford F, Marrack P, Kappler J (2002) Structural basis of cytochrome c presentation by IE(k). *J Exp Med* 195: 1043–1052

Gao Y, Kilfoil ML (2009) Accurate detection and complete tracking of large populations of features in three dimensions. *Opt Express* 17: 4685–4704

Gascoigne NR (2008) Do T cells need endogenous peptides for activation? *Nat Rev Immunol* 8: 895–900

Gohring J, Kellner F, Schrangl L, Platzer R, Klotzsch E, Stockinger H, Huppa JB, Schutz GJ (2021) Temporal analysis of T-cell receptor-imposed forces via quantitative single molecule FRET measurements. *Nat Commun* 12: 2502

Gohring J, Schrangl L, Schutz GJ, Huppa JB (2022) Mechanosurveillance: tiptoeing T cells. *Front Immunol* 13: 886328

Gombos I, Detre C, Vamosi G, Matko J (2004) Rafting MHC-II domains in the APC (presynaptic) plasma membrane and the thresholds for T-cell activation and immunological synapse formation. *Immunol Lett* 92: 117–124

Helft J, Bottcher J, Chakravarty P, Zelenay S, Huotari J, Schraml BU, Goubau D, Reis e Sousa C (2015) GM-CSF mouse bone marrow cultures comprise a heterogeneous population of CD11c(+)MHCII(+) macrophages and dendritic cells. *Immunity* 42: 1197–1211

Hellmeier J, Platzer R, Eklund AS, Schlichthaerle T, Karner A, Motsch V, Schneider MC, Kurz E, Bamieh V, Brameshuber M *et al* (2021a) DNA origami demonstrate the unique stimulatory power of single pMHCs as T cell antigens. *Proc Natl Acad Sci USA* 118: e2016857118

Hellmeier J, Platzer R, Muhlgrabner V, Schneider MC, Kurz E, Schutz GJ, Huppa JB, Sevcsik E (2021b) Strategies for the site-specific decoration of DNA origami nanostructures with functionally intact proteins. *ACS Nano* 15: 15057–15068

Hellmeier J, Platzer R, Huppa JB, Sevcsik E (2023) A DNA origami-based biointerface to interrogate the spatial requirements for sensitized T-cell antigen recognition. *Methods Mol Biol* 2654: 277–302

Hess ST, Girirajan TPK, Mason MD (2006) Ultra-high resolution imaging by fluorescence photoactivation localization microscopy. *Biophys J* 91: 4258–4272

Hiltbold EM, Poloso NJ, Roche PA (2003) MHC class II-peptide complexes and APC lipid rafts accumulate at the immunological synapse. *J Immunol* 170: 1329–1338

Hoerter JA, Brzostek J, Artyomov MN, Abel SM, Casas J, Rybakin V, Ampudia J, Lotz C, Connolly JM, Chakraborty AK *et al* (2013) Coreceptor affinity for MHC defines peptide specificity requirements for TCR interaction with coagonist peptide-MHC. *J Exp Med* 210: 1807–1821

Howarth M, Ting AY (2008) Imaging proteins in live mammalian cells with biotin ligase and monovalent streptavidin. *Nat Protoc* 3: 534–545

Howarth M, Chinnapen DJ, Gerrow K, Dorrestein PC, Grandy MR, Kelleher NL, El-Husseini A, Ting AY (2006) A monovalent streptavidin with a single femtomolar biotin binding site. *Nat Methods* 3: 267–273

Hsu CJ, Hsieh WT, Waldman A, Clarke F, Huseby ES, Burkhardt JK, Baumgart T (2012) Ligand mobility modulates immunological synapse formation and T cell activation. *PLoS ONE* 7: e32398

Huang J, Zarnitsyna VI, Liu B, Edwards LJ, Jiang N, Evavold BD, Zhu C (2010) The kinetics of two-dimensional TCR and pMHC interactions determine T-cell responsiveness. *Nature* 464: 932–936

Huang J, Brameshuber M, Zeng X, Xie J, Li QJ, Chien YH, Valitutti S, Davis MM (2013) A single peptide-major histocompatibility complex ligand triggers digital cytokine secretion in CD4(+) T cells. *Immunity* 39: 846–857

Huppa JB, Davis MM (2003) T-cell-antigen recognition and the immunological synapse. *Nat Rev Immunol* 3: 973–983

Huppa JB, Gleimer M, Sumen C, Davis MM (2003) Continuous T cell receptor signaling required for synapse maintenance and full effector potential. *Nat Immunol* 4: 749–755

Huppa J, Axmann M, Mörtelmaier M, Lillemeier B, Newell E, Brameshuber M, Klein L, Schütz G, Davis M (2010) TCR-peptide-MHC interactions in situ show accelerated kinetics and increased affinity. *Nature* 463: 963–967

Huse M, Klein LO, Girvin AT, Faraj JM, Li QJ, Kuhns MS, Davis MM (2007) Spatial and temporal dynamics of T cell receptor signaling with a photoactivatable agonist. *Immunity* 27: 76–88

Inaba K, Swiggard WJ, Steinman RM, Romani N, Schuler G, Brinster C (2009) Isolation of dendritic cells. *Curr Protoc Immunol* Chapter 3: 3.7.1–3.7.19

Irvine DJ, Purbhoo MA, Krogsgaard M, Davis MM (2002) Direct observation of ligand recognition by T cells. *Nature* 419: 845–849

Jensen LG, Hoh TY, Williamson DJ, Griffie J, Sage D, Rubin-Delanchy P, Owen DM (2022) Correction of multiple-blinking artifacts in photoactivated localization microscopy. *Nat Methods* 19: 594–602

Jiang N, Huang J, Edwards LJ, Liu B, Zhang Y, Beal CD, Evavold BD, Zhu C (2011) Two-stage cooperative T cell receptor-peptide major histocompatibility complex-CD8 trimolecular interactions amplify antigen discrimination. *Immunity* 34: 13–23

Knorr R, Karacsonyi C, Lindner R (2009) Endocytosis of MHC molecules by distinct membrane rafts. *J Cell Sci* 122: 1584–1594

Koushik SV, Blank PS, Vogel SS (2009) Anomalous surplus energy transfer observed with multiple FRET acceptors. *PLoS ONE* 4: e8031

Krogsgaard M, Li QJ, Sumen C, Huppa JB, Huse M, Davis MM (2005) Agonist/endogenous peptide-MHC heterodimers drive T cell activation and sensitivity. *Nature* 434: 238–243

Kusumi A, Fujiwara TK, Chadda R, Xie M, Tsunoyama TA, Kalay Z, Kasai RS, Suzuki KG (2012) Dynamic organizing principles of the plasma membrane that regulate signal transduction: commemorating the fortieth anniversary of Singer and Nicolson's fluid-mosaic model. *Annu Rev Cell Dev Biol* 28: 215–250

Li QJ, Dinner AR, Qi S, Irvine DJ, Huppa JB, Davis MM, Chakraborty AK (2004) CD4 enhances T cell sensitivity to antigen by coordinating Lck accumulation at the immunological synapse. *Nat Immunol* 5: 791–799

Liu B, Chen W, Evavold BD, Zhu C (2014) Accumulation of dynamic catch bonds between TCR and agonist peptide-MHC triggers T cell signaling. *Cell* 157: 357–368

Lu X, Gibbs JS, Hickman HD, David A, Dolan BP, Jin Y, Kranz DM, Bennink JR, Yewdell JW, Varma R (2012) Endogenous viral antigen processing generates peptide-specific MHC class I cell-surface clusters. *Proc Natl Acad Sci USA* 109: 15407–15412

Ma Z, Sharp KA, Janmey PA, Finkel TH (2008) Surface-anchored monomeric agonist pMHCs alone trigger TCR with high sensitivity. *PLoS Biol* 6: e43

Ma JK, Platt MY, Eastham-Anderson J, Shin JS, Mellman I (2012) MHC class II distribution in dendritic cells and B cells is determined by ubiquitin chain length. *Proc Natl Acad Sci USA* 109: 8820–8827

MacKinnon JG (2009) Bootstrap hypothesis testing. In *Handbook of Computational Econometrics*, Belsley DA, Kontoghiorghes EJ (eds), pp 183–213. Hoboken, NJ: John Wiley & Sons, Ltd

Manzo C, Torreno-Pina JA, Joosten B, Reinieren-Beeren I, Gualda EJ, Loza-Alvarez P, Figdor CG, Garcia-Parajo MF, Cambi A (2012) The neck region of the C-type lectin DC-SIGN regulates its surface spatiotemporal organization and virus-binding capacity on antigen-presenting cells. *J Biol Chem* 287: 38946–38955

Matsui K, Boniface JJ, Reay PA, Schild H, de St Groth BF, Davis MM (1991) Low affinity interaction of peptide-MHC complexes with T cell receptors. *Science* 254: 1788–1791

Matsui K, Boniface JJ, Steffner P, Reay PA, Davis MM (1994) Kinetics of T-cell receptor binding to peptide/I-Ek complexes: correlation of the dissociation rate with T-cell responsiveness. *Proc Natl Acad Sci USA* 91: 12862–12866

Moertelmaier M, Brameshuber M, Linimeier M, Schutz GJ, Stockinger H (2005) Thinning out clusters while conserving stoichiometry of labeling. *Appl Phys Lett* 87: 263903

Mukherjee G, Rasmusson B, Linner JG, Quinn MT, Parkos CA, Magnusson KE, Jesaitis AJ (1998) Organization and mobility of CD11b/CD18 and targeting of superoxide on the surface of degranulated human neutrophils. *Arch Biochem Biophys* 357: 164–172

Nagy P, Matyus L, Jenei A, Panyi G, Varga S, Matko J, Szollosi J, Gaspar R, Jovin TM, Damjanovich S (2001) Cell fusion experiments reveal distinctly different association characteristics of cell-surface receptors. *J Cell Sci* 114: 4063–4071

Ohradanova-Repic A, Nogueira E, Hartl I, Gomes AC, Preto A, Steinhuber E, Muhlgrabner V, Repic M, Kuttke M, Zwirzitz A *et al* (2018) Fab antibody fragment-functionalized liposomes for specific targeting of antigen-positive cells. *Nanomedicine* 14: 123–130

Ovesny M, Krizek P, Borkovec J, Svindrych Z, Hagen GM (2014) ThunderSTORM: a comprehensive ImageJ plug-in for PALM and STORM data analysis and super-resolution imaging. *Bioinformatics* 30: 2389–2390

Pettmann J, Awada L, Rozycki B, Huhn A, Faour S, Kutuzov M, Limozin L, Weikl TR, van der Merwe PA, Robert P *et al* (2023) Mechanical forces impair antigen discrimination by reducing differences in T-cell receptor/peptide-MHC off-rates. *EMBO J* 42: e111841

Pierre P, Turley SJ, Gatti E, Hull M, Meltzer J, Mirza A, Inaba K, Steinman RM, Mellman I (1997) Developmental regulation of MHC class II transport in mouse dendritic cells. *Nature* 388: 787–792

Platzer R, Huppa JB (2020) T-cell antigen recognition – lessons from the past and projections into the future. In *eLS*, pp 1–26. Chichester: John Wiley & Sons, Ltd

Platzer R, Rossboth BK, Schneider MC, Sevcsik E, Baumgart F, Stockinger H, Schutz GJ, Huppa JB, Brameshuber M (2020) Unscrambling fluorophore blinking for comprehensive cluster detection via photoactivated localization microscopy. *Nat Commun* 11: 4993

Purbhoo MA, Irvine DJ, Huppa JB, Davis MM (2004) T cell killing does not require the formation of a stable mature immunological synapse. *Nat Immunol* 5: 524–530

Robertson C, George SC (2012) Theory and practical recommendations for autocorrelation-based image correlation spectroscopy. *J Biomed Opt* 17: 080801-1

Roe MW, Lemasters JJ, Herman B (1990) Assessment of Fura-2 for measurements of cytosolic free calcium. *Cell Calcium* 11: 63–73

Rossboth B, Arnold AM, Ta H, Platzer R, Kellner F, Huppa JB, Brameshuber M, Baumgart F, Schutz GJ (2018) TCRs are randomly distributed on the plasma membrane of resting antigen-experienced T cells. *Nat Immunol* 19: 821–827

Ruprecht V, Brameshuber M, Schutz GJ (2010) Two-color single molecule tracking combined with photobleaching for the detection of rare molecular interactions in fluid biomembranes. *Soft Matter* 6: 568–581

Sahl SJ, Hell SW, Jakobs S (2017) Fluorescence nanoscopy in cell biology. *Nat Rev Mol Cell Biol* 18: 685–701

Salles A, Billaudeau C, Sergé A, Bernard A-M, Phélipot M-C, Bertaux N, Fallet M, Grenot P, Marguet D, He H-T *et al* (2013) Barcoding T cell calcium response diversity with methods for automated and accurate analysis of cell signals (MAAACS). *PLoS Comput Biol* 9: e1003245

Schatzlmaier P, Supper V, Goschl L, Zwirzitz A, Eckerstorfer P, Ellmeier W, Huppa JB, Stockinger H (2015) Rapid multiplex analysis of lipid raft components with single-cell resolution. *Sci Signal* 8: rs11

Schindelin J, Arganda-Carreras I, Frise E, Kaynig V, Longair M, Pietzsch T, Preibisch S, Rueden C, Saalfeld S, Schmid B *et al* (2012) Fiji: an open-source platform for biological-image analysis. *Nat Methods* 9: 676–682

Schutz GJ, Schindler H, Schmidt T (1997) Single-molecule microscopy on model membranes reveals anomalous diffusion. *Biophys J* 73: 1073–1080

Sengupta P, Jovanovic-Talisman T, Skoko D, Renz M, Veatch SL, Lippincott-Schwartz J (2011) Probing protein heterogeneity in the plasma membrane using PALM and pair correlation analysis. *Nat Methods* 8: 969–975

Sevcsik E, Brameshuber M, Folser M, Weghuber J, Honigmann A, Schutz GJ (2015) GPI-anchored proteins do not reside in ordered domains in the live cell plasma membrane. *Nat Commun* 6: 6969

Sibener LV, Fernandes RA, Kolawole EM, Carbone CB, Liu F, McAffee D, Birnbaum ME, Yang X, Su LF, Yu W *et al* (2018) Isolation of a structural mechanism for uncoupling T cell receptor signaling from peptide-MHC binding. *Cell* 174: 672–687

Tsumoto K, Shinoki K, Kondo H, Uchikawa M, Juji T, Kumagai I (1998) Highly efficient recovery of functional single-chain Fv fragments from inclusion bodies overexpressed in *Escherichia coli* by controlled introduction of oxidizing reagent—application to a human single-chain Fv fragment. *J Immunol Methods* 219: 119–129

Turley SJ, Inaba K, Garrett WS, Ebersold M, Unternaehrer J, Steinman RM, Mellman I (2000) Transport of peptide-MHC class II complexes in developing dendritic cells. *Science* 288: 522–527

Umemura YM, Vrljic M, Nishimura SY, Fujiwara TK, Suzuki KG, Kusumi A (2008) Both MHC class II and its GPI-anchored form undergo hop diffusion as observed by single-molecule tracking. *Biophys J* 95: 435–450

Unternaehrer JJ, Chow A, Pypaert M, Inaba K, Mellman I (2007) The tetraspanin CD9 mediates lateral association of MHC class II molecules on the dendritic cell surface. *Proc Natl Acad Sci USA* 104: 234–239

Verdijk P, van Veelen PA, de Ru AH, Hensbergen PJ, Mizuno K, Koerten HK, Koning F, Tensen CP, Mommaas AM (2004) Morphological changes during dendritic cell maturation correlate with cofilin activation and translocation to the cell membrane. *Eur J Immunol* 34: 156–164

Vrljic M, Nishimura SY, Brasselet S, Moerner WE, McConnell HM (2002) Translational diffusion of individual class II MHC membrane proteins in cells. *Biophys J* 83: 2681–2692

Weikl TR, Hu J, Xu GK, Lipowsky R (2016) Binding equilibrium and kinetics of membrane-anchored receptors and ligands in cell adhesion: insights from computational model systems and theory. *Cell Adh Migr* 10: 576–589

Wheeler MW, Park RM, Bailer AJ (2006) Comparing median lethal concentration values using confidence interval overlap or ratio tests. *Environ Toxicol Chem* 25: 1441–1444

Wieser S, Schutz GJ (2008) Tracking single molecules in the live cell plasma membrane-Do's and Don't's. *Methods* 46: 131–140

Wieser S, Moertelmaier M, Fuertbauer E, Stockinger H, Schutz GJ (2007) (Un) confined diffusion of CD59 in the plasma membrane determined by high-resolution single molecule microscopy. *Biophys J* 92: 3719–3728

Wulfing C, Rabinowitz JD, Beeson C, Sjaastad MD, McConnell HM, Davis MM (1997) Kinetics and extent of T cell activation as measured with the calcium signal. *J Exp Med* 185: 1815–1825

Wulfing C, Sumen C, Sjaastad MD, Wu LC, Dustin ML, Davis MM (2002) Costimulation and endogenous MHC ligands contribute to T cell recognition. *Nat Immunol* 3: 42–47

Xie J, Huppa JB, Newell EW, Huang J, Ebert PJ, Li QJ, Davis MM (2012) Photocrosslinkable pMHC monomers stain T cells specifically and cause ligand-bound TCRs to be 'preferentially' transported to the cSMAC. *Nat Immunol* 13: 674–680

Zuidscherwoude M, de Winde CM, Cambi A, van Spriel AB (2014) Microdomains in the membrane landscape shape antigen-presenting cell function. *J Leukoc Biol* 95: 251–263

Zuidscherwoude M, Gottfert F, Dunlock VM, Figdor CG, van den Bogaart G, van Spriel AB (2015) The tetraspanin web revisited by super-resolution microscopy. *Sci Rep* 5: 12201